Measuring Binding Kinetics of Therapeutic Antibodies to Membrane Receptors Using Nanohole Array SPR Biosensors

A DISSERTATION
SUBMITTED TO THE FACULTY OF
THE UNIVERSITY OF MINNESOTA BY

Luke Jordan

IN PARTIAL FULFILLMENT OF THE REQUIREMENTS
FOR THE DEGREE OF
DOCTOR OF PHILOSOPHY

Dr. Sang-Hyun Oh, Adviser

April 2016

Front Matter

Acknowledgements

First, I would like to thank my adviser, Sang-Hyun Oh, for his dedicated mentoring and generous provision to learn a multitude of fabrication, characterization, and analytical methods to perform scientific research. Second, I would like to thank my mentor, Nathan Wittenberg, who taught me so many practical things in the lab and for helping plan experiments and analyze data. I also would like to thank two former lab members, Hyungsoon Im and Si-Hoon Lee, who strengthened my work ethic and generously shared their expertise of micro- and nanofabrication. I also would like to thank all my wonderful current and former lab mates along the way who made this a wonderful endeavor: Shailabh Kumar, Avijit Barik, Yong-Sang Ryu, Tim Johnson, Stephen Olson, Daehan Yoo, Xiaoshu Chen, Lauren Otto, Nathan Lindquist, Antoine Lesuffleur, Jonah Shaver, Dmitriy Zhukov, Sudhir Cherukulappurath, Jincy Jose, Dan Klemme, and Dan Mohr.

In addition, I want to thank my collaborators at the Mayo Clinic who provided valuable samples, discussion, and a noble cause to spend time on: Moses Rodriguez, Arthur Warrington, Xiaohua Xu, Jens Watzlawik, Bharath Wootla, Aleksandar Denic, and Brent Wright.

I would also like to thank the numerous scientists and technicians in the Minnesota Nanofabrication Center, the Characterization Facility, and University Imaging Center who taught me to use their sophisticated instruments and machines and helped solve arising technical problems, in particular Tony Whipple, Greg Haugstad, and John Oja.

Lastly, I would like to thank my funding sources: the 3M Company for a fellowship and an opportunity to get to know their innovative company, and the Minnesota Partnership for Biotechnology and Medical Genomics and National Institutes of Health for grants to conduct this research.

Abstract

In the field of drug discovery, two important metrics of candidate drugs are their binding affinity and kinetics to target receptors. Dr. Moses Rodriguez and his colleagues at the Mayo Clinic have found monoclonal IgM antibodies exhibiting therapeutic effects for multiple sclerosis and amyotrophic lateral sclerosis in animal models, and therefore desired to obtain the kinetic profiles of these antibodies to their targets. Dr. Sang-Hyun Oh's lab at the University of Minnesota specializes in designing and fabricating plasmonic devices, and have developed a nanohole array sensor coated with silicone dioxide which permits formation of cell mimicking supported lipid bilayers. The focus of this dissertation has been to build these devices and develop assays to measure the binding between these antibodies and receptors in cell extracts and supported lipid bilayers. The first antibody to measure was rHIgM22, which binds to myelin membrane. We did not know the receptor, so we used myelin extracts which would include the unknown receptors, and attached these particles to the sensor surface by passive immobilization. To reduce particle size into the sensor detection window, we extruded the particles through pores of known dimensions. After immobilization we measured binding with antibodies. Unfortunately, binding with rHIgM22 was undetectable, but a similar antibody, mouse IgM O4, which also binds to myelin and has a therapeutic effect, did bind consistently and gave $K_{D,\ apparent}$ = 2.6 ± 3.6 nM, k_a = 2.5 ± 0.0l × 10^4 $M^{-1}s^{-1}$, and $k_{d,slow}$ = 6.6 ± 0.3 × 10^{-5} s^{-1}. The second antibody to measure was rHIgM12, which binds to neuronal membranes. We found rHIgM12 binds to the gangliosides GT1b and GD1a, but not GM1. These gangliosides were incorporated into supported lipid bilayers (5 mol %) and binding to the antibodies was measured. Binding of rHIgM12 to GT1b gave $K_{D,\ apparent}$ = 24.8 ± 7.9 nM, k_a = 2.19 ± 0.196 × 10^4 $M^{-1}s^{-1}$, and $k_{d,slow}$ = 4.72 ± 1.15 × 10^{-4} s^{-1}. Binding of rHIgM12 to GD1a gave $K_{D,\ apparent}$ = 42.3 ± 20.6 nM, k_a = 1.79 ± 0.516 × 10^4 $M^{-1}s^{-1}$, and $k_{d,slow}$ = 4.43 ± 1.38 × 10^{-4} s^{-1}.

Table of Contents

List of Figures

List of Tables

List of Abbreviations and Acronyms

AFM	atomic force microscopy
Ag	silver
Al_2O_3	aluminum oxide
ALD	atomic layer deposition
ALS	amyotrophic lateral sclerosis
Au	gold
CCD	charged coupled device
Chol	cholesterol
CNP	2',3'-cyclic-nucleotide 3'-phosphodiesterase
Cryo-SEM	cryogenic scanning electron microscopy
Cryo-TEM	cryogenic transmission electron microscopy
EAE	Experimental Autoimmune Encephalomyelitis
EDTA	ethylenediaminetetraacetic acid
egg PC	L-α-phosphatidylcholine from chicken eggs
ELISA	enzyme-linked immunosorbent assays
FIB	focused ion beam
FRAP	fluorescence recovery after photobleaching
GD1a	disialoganglioside
GM1	monosialoganglioside
GPMV	giant plasma membrane vesicle
GT1b	trisialoganglioside
GUV	giant unilamellar vesicle
HSA	human serum albumin
IgM	Immunoglobulin M
$K_{D,\ apparent}$	apparent equilibrium dissociation constant
k_a	association kinetic constant
$k_{d,\ fast}$	fast dissociation kinetic constant
$k_{d,\ slow}$	slow dissociation kinetic constant
MAG	myelin associated glycoprotein
MBP	myelin basic protein
MOG	myelin oligodendrocyte glycoprotein
MP	methylprednisolone
MS	multiple sclerosis
NSL	nanosphere lithography
PDMS	polydimethylsiloxane
PLP	proteolipid protein
PTFE	polytetrafluoroethylene
PVP	poly(N-vinylpyrrolidone)
Rho-DMPE	1,2-dimyristoyl-sn-glycero-3-phosphoethanolamine-N-(lissamine rhodamine B sulfonyl

rHIgM12	recombinant human immunoglobulin 12
rHIgM22	recombinant human immunoglobulin 22
SAM	self-assembled monolayer
SEM	scanning electron microscopy
sHIgM12	serum human immunoglobulin 12
sHIgM22	serum human immunoglobulin 22
Si	silicon
SiO_2	silicon dioxide
SLB	supported lipid bilayer
SPP	surface plasmon polariton
SPR	surface plasmon resonance
Sulf	sulfated galactocerebroside
SUV	small unilamellar vesicle
Tris	tris(hydroxymethyl)aminomethane
TMEV	Theiler's Murine Encephalomyelitis Virus

List of Publications

Xu X, Denic A, Jordan LR, Wittenberg NJ, Warrington A, Wootla B, Papke LM, Zoecklein LJ, Yoo D, Shaver J, Oh S-H, Pease LR, Rodriguez M. A Natural Human IgM that Binds to Gangliosides is Therapeutic in Murine Models of Amyotrophic Lateral Sclerosis. *Disease Models & Mechanisms*. **2015**, 8 (8), 831-842.

Ryu Y-S, Yoo D, Wittenberg NJ, Jordan LR, Lee S-D, Parikh AN, Oh S-D. Lipid Membrane Deformation Accompanied by Disk-to-Ring Shape Transition of Cholesterol-Rich Domains. *JACS*. **2015**, 137 (27), 8692-8695.

Cha H, Lee J, Jordan LR, Lee S-H, Oh S-H, Kim H-J, Park J, Hong S, Jeon H. Surface Passivation of a Photonic Crystal Band-Edge Laser by Atomic Layer Deposition of SiO2 and Its Application for Biosensing. *Nanoscale*. **2015**, 7, 3565-71.

Ryu Y-S, Lee I-H, Suh J-H, Park SC, Oh S, Jordan LR, Wittenberg NJ, Oh S-H, Jeon NL, Lee B, Parikh AN, Lee S-D. Reconstituting Ring-Rafts in Bud-Mimicking Topography of Model Membranes. *Nature Communications*. **2014**, 5, 1-8.

Nathan J Wittenberg, Bharath Wootla, Jordan LR, Denic A, Warrington AE, Oh S-H, Rodriguez M. Applications of SPR for the Characterization of Molecules Important in the Pathogenesis and Treatment of Neurodegenerative Diseases. *Expert Review of Neurotherapeutics*. **2014**, 14, 449-463.

Wittenberg NJ, Johnson TW, Jordan LR, Xu X, Warrington AE, Rodriguez M, Oh S-H. Formation of Biomembrane Microarrays with a Squeegee-Based Assembly Method. *Journal of Visualized Experiments*. **2014**, 87, e51501.

Xu X, Wittenberg NJ, Jordan LR, Kumar S, Watzlawik JO, Warrington AE, Oh S-H, Rodriguez M (2013). A Patterned Recombinant Human IgM Guides Neurite Outgrowth of CNS Neurons. *Scientific Reports*. **2013**, 3, 2267.

Jose J, Jordan LR, Johnson TW, Lee SH, Wittenberg NJ, Oh S-H. Topographically Flat Substrates with Embedded Nanoplasmonic Devices for Biosensing. *Advanced Functional Materials*. **2013**, 23, 2812–2820.

Lee SH, Lindquist NC, Wittenberg NJ, Jordan LR, Oh S-H. Real-Time Full-Spectral Imaging and Affinity Measurements from 50 Microfluidic Channels Using Nanohole Surface Plasmon Resonance. *Lab on a Chip*. **2012**, 12, 3882–90.

1 Introduction

1.1 Brief Overview

Neurologist Dr. Moses Rodriguez and his colleagues at the Mayo Clinic have been studying and developing several antibodies that may be therapeutic for a number of debilitating neurological disorders, including multiple sclerosis (MS) and amyotrophic lateral sclerosis (ALS). From their initial discoveries of these antibodies first in mice and then in humans, they have generated recombinant forms of two human antibodies for production as therapeutic drugs, recently finishing the first phase of clinical trials with one of them. To further understand physical properties of these drugs, they have sought to validate the antigens (molecules that the antibodies bind to, or "receptors") of the antibodies and measure binding rates of these interactions. To obtain this information they have teamed up with Dr. Sang-Hyun Oh's plasmonics laboratory at the University of Minnesota to build an instrument capable of making these measurements. This dissertation focuses on development of assays using these plasmonic biosensors to measure the binding kinetics between these antibodies and receptors in native myelin membranes as well as supported lipid bilayers.

1.2 Scope of Dissertation

This dissertation covers the design and testing of two approaches to measure binding kinetics between IgM antibodies and their antigens, one with natural membrane particles and the other with supported lipid bilayers. It includes the fabrication of microfluidic nanoengineered surface plasmon resonance (SPR) chips to measure the binding kinetics in a label free, real-time manner on a standard laboratory microscope. The nanoengineered sensing element consists of large area nanohole array in a thin metallic film. The experimental setup includes an inverted microscope attached to an imaging spectrometer and CCD to allow for multiplexed experiments.

1.3 Outline of Chapters

Chapter 2 explains the background material upon which this research project is built. This background material includes the research and development of these therapeutic antibodies by the Mayo researchers, the concept and measurement of the affinity and kinetics of molecular interactions, the basics of surface plasmon resonance and its application in measuring kinetics, and the development of large area nanohole arrays and lipid bilayer sensing by the Oh lab.

Chapters 3 and 4 cover the unique research performed for this dissertation. Chapter 3 covers the development of an SPR assay to measure binding between the multiple sclerosis (MS) treating antibodies, mouse IgM O4 and human rHIgM22, and the membranes they bind to, myelin from oligodendrocytes. Chapter 4 covers the assay development of an SPR assay to measure binding between amyotrophic lateral sclerosis (ALS) treating antibody, rHIgM12, and the gangliosides in a supported lipid bilayer (SLB).

The Appendix includes exploration of a technique which might help with problems encountered in the membrane particle assay described in chapter 3.

2 Background

2.1 Medical Purpose

Therapeutic Antibodies for Multiple Sclerosis and Amyotrophic Lateral Sclerosis

The goals of this research were to develop surface plasmon resonance assays to measure binding properties of human antibodies rHIgM22 and rHIgM12, which may be able to reverse some of the damage done by two devastating neurological diseases, multiple sclerosis (MS) and amyotrophic lateral sclerosis (ALS). There is currently no cure for either of these diseases, only medications to slow disease progression.[1] These antibodies have shown regenerative behaviors in cell and animal studies, and rHIgM22 has entered clinical trials, recently passing the first round (https://clinicaltrials.gov/ct2/show/NCT01803867). This section reviews the MS and ALS diseases, the evidence for the therapeutic effect of these antibodies, and the discovery and development of these antibodies.

Multiple Sclerosis

MS is the most common inflammatory demyelinating disease of the central nervous system (CNS).[1] Two cell types affected by MS are neurons and oligodendrocytes, illustrated in Figure 1. In the normal, healthy state, oligodendrocytes form wrappings of specialized membrane, myelin sheaths, around the axons of nearby neurons. These myelin sheaths enable high speed electrochemical signals to be sent from one neuron to the next. In MS, the body's immune system attacks and breaks down the myelin sheathes, causing reduction in conduction speed between neurons, and can eventually result in neuronal death. The disease is named after the multiple scars ("sclerae") present in the CNS tissue in these areas. Because these sclerae can appear anywhere in the central nervous system,

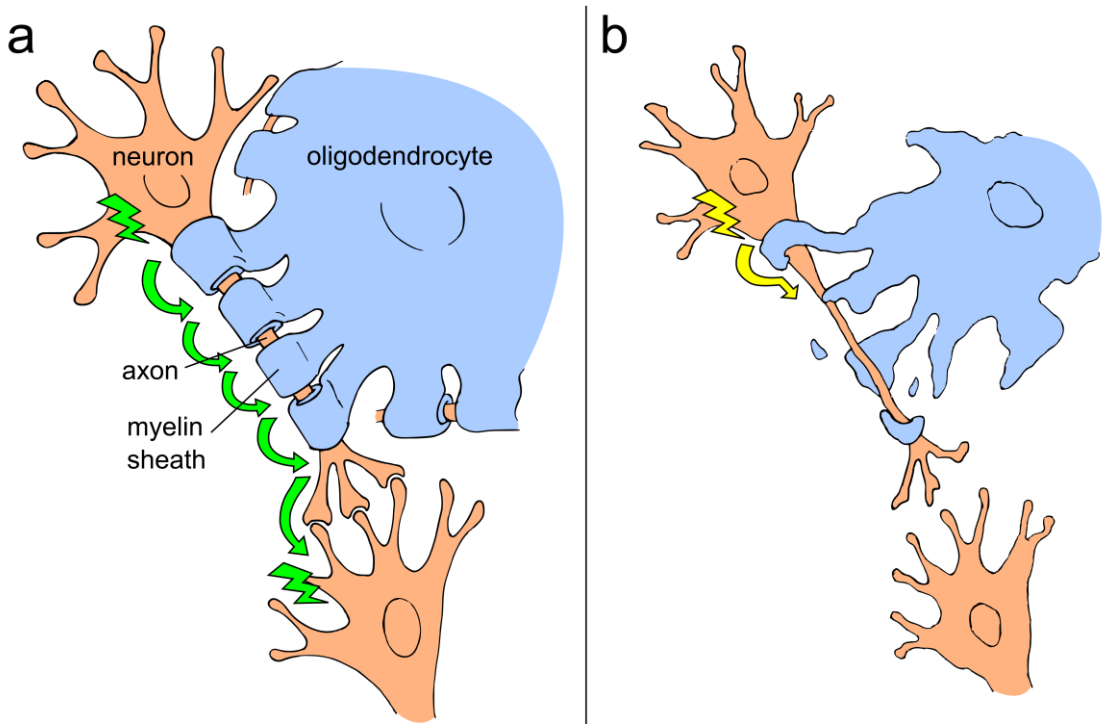

Figure 1: Multiple sclerosis (MS) damages neurons and oligodendrocytes. (**a**) In the healthy state, a neuron sends electrochemical signals (depicted as green arrows) to another neuron through its axon. Rapid signal propagation along the axon is enabled by wrappings of myelin sheaths from a nearby oligodendrocyte. (**b**) In the MS diseased state, myelin gets damaged, resulting in signal propagation breakdown and potential neuronal death.

the symptoms are wide ranging and can be of an autonomic, motor, sensory, visual, or psychological nature.

The disease progresses either in a steady manner, by acute attacks and partial recovery, or a combination of these two manners, resulting in eventual permanent deficits and potentially ultimately death. Estimates put the global median prevalence of MS at 30 per 100,000 people.[2] The disease occurs in all countries and can affect both genders, however there is an increased prevalence for those who live farther away from the equator, white people with European ancestry, and females over males (~2:1). Currently there are no cures, only treatments to reduce the severity or frequency of attacks. One therapeutic approach is for a drug to protect oligodendrocytes and stimulate their remyelination of

axons. One of the Mayo antibodies, rHIgM22, has been found to induce remyelination in cell cultures and in animals, and is being pursued as a therapy for MS.

Amyotrophic Lateral Sclerosis

A second, devastating, incurable neurological disease is amyotrophic lateral sclerosis (ALS). Motor neurons are neurons with cell bodies in the spinal cord or brain, which connect to muscles and send the signals for them to contract, as shown in Figure 2. ALS is a disease in which these motor neurons slowly shrivel and die. When these neurons die, the muscles they innervate also slowly wither and no longer contract, resulting in the loss of the ability to move, speak, swallow, or even breathe without a ventilator.

ALS is a quick acting disease and often leads to death within only 3-5 years. The following famous case provides a stark example. The disease is also known as "Lou Gehrig's disease", after the United States professional baseball player, Lou Gehrig, who

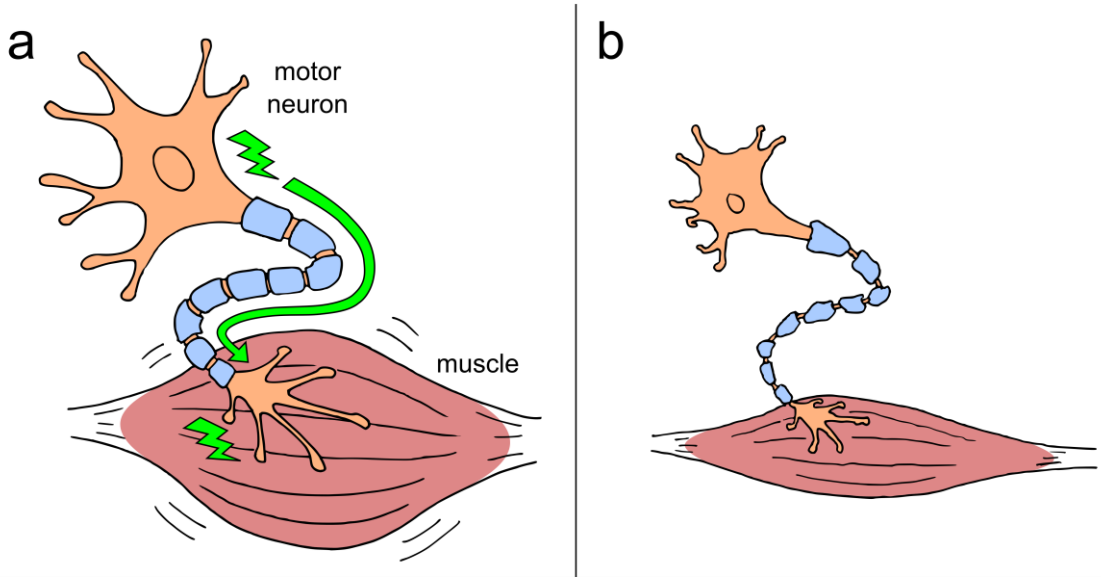

Figure 2: Amyotrophic lateral sclerosis (ALS) damages motor neurons and the muscles they innervate. (**a**) In the healthy state, motor neurons send electrochemical signals (depicted as a green arrow) to muscles to cause them to contract. (**b**) In the ALS diseased state, these motor neurons degenerate, accompanied by muscle atrophy and loss of motor function.

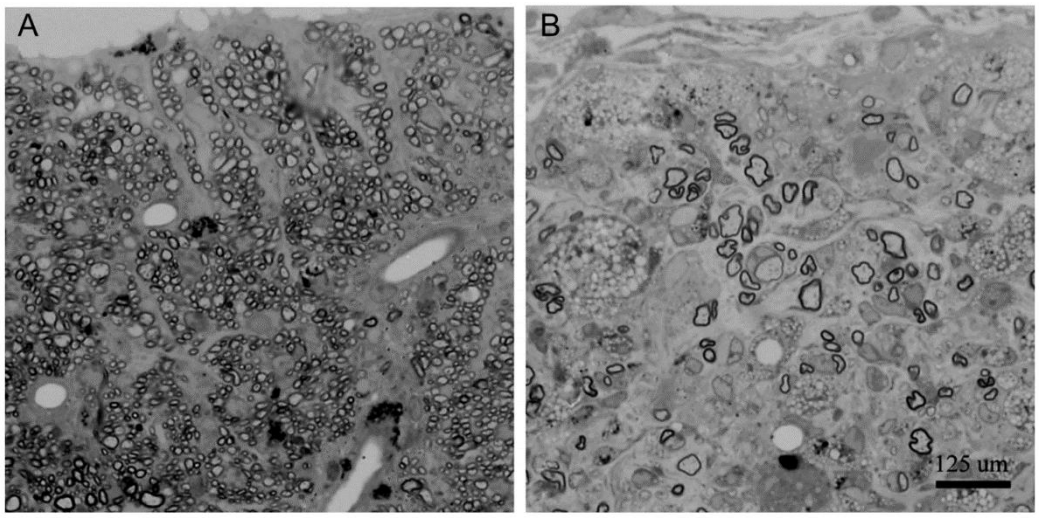

Figure 3: rHIgM22 increases myelin in a mouse model of MS. Mice were infected with TMEV which causes demyelination of neurons and is used as a mouse model for MS. One group of mice were given a single 50 µg dose of rHIgM22, and a second group was given a control human IgM. Five weeks later, spinal cord was sliced, stained, and photographed. Myelin sheathes encircling neuronal axons are stained and visible as dark rings. (**A**) Spinal cord from mouse injected with rHIgM22. (**B**) Spinal cord from mouse injected with a control human IgM. Significant remyelination occurred in the mouse treated with rHIgM22. Figure reproduced with permission from: Rodriguez, Warrington, and Pease. Invited Article: Human Natural Autoantibodies in the Treatment of Neurologic Disease. Neurology 2009, 72 (14), 1269–1276.[4]

had the record for the most consecutive games played (2,130, which lasted for over 50 years), but was diagnosed with ALS at the age of 36 and forced to retire, followed by death only two years later. In Europe, the disease occurs in ~2 in 100,000 people.[3] There is currently no cure for ALS, and only one drug approved by the FDA, riluzole (Rilutek), which slows the progression down. One avenue of research is to find drugs that help stimulate neuronal growth and function to regain lost motor function. A second Mayo antibody, rHIgM12, has been found to induce neuronal growth and function in cell cultures and in animals, and is being explored as a treatment for ALS.

Antibodies as Regenerative Therapies

Dr. Moses Rodriguez, a neurologist at the Mayo Clinic, and his colleagues have discovered and developed these unique antibodies, rHIgM22 and rHIgM12, which may be able to reverse some of the damage of these diseases.

rHIgM22 may help with people suffering from MS. This antibody has been found to help in animal models of MS. In these studies, mice were infected with Theiler's Murine Encephalomyelitis Virus (TMEV), which leads to neuron degeneration and eventual paralysis, similar to that seen in MS patients[4]. One group of mice was given a single 50 μg dose of rHIgM22 while the other group received a control human antibody. Figure 3 shows mouse spinal cord slices taken from mice treated with rHIgM22 (panel A) and those treated with the control antibody (panel B). The dark rings are stains of the myelin surrounding neurons. The number of normal myelin sheaths is significantly higher in the rHIgM22 treated mice.

Another measure of the disease progress and drug effectiveness is the amount of body movement of TMEV mice. Body movement of live mice can be quantified by the number of times the mice break infrared beams as they move about their cages, as seen in Figure 4. Mice with the standard MS treatment methylprednisolone (MP) plus a single dose of rHIgM22 (black bars) showed significantly more movement than those with only MP (gray bars). As further evidence of this antibody's effectiveness, rHIgM22 helped another mouse model of demyelinating disease: Experimental Autoimmune Encephalomyelitis (EAE).

These promising animal studies have led to human clinical trials. rHIgM22 has recently successfully passed phase I, which evaluates safety, toxicity, pharmacokinetics, and side effects of candidate drugs (https://clinicaltrials.gov/ct2/show/NCT01803867). rHIgM22 is currently entering phase II, which tests a larger group, and further evaluates safety and efficacy.

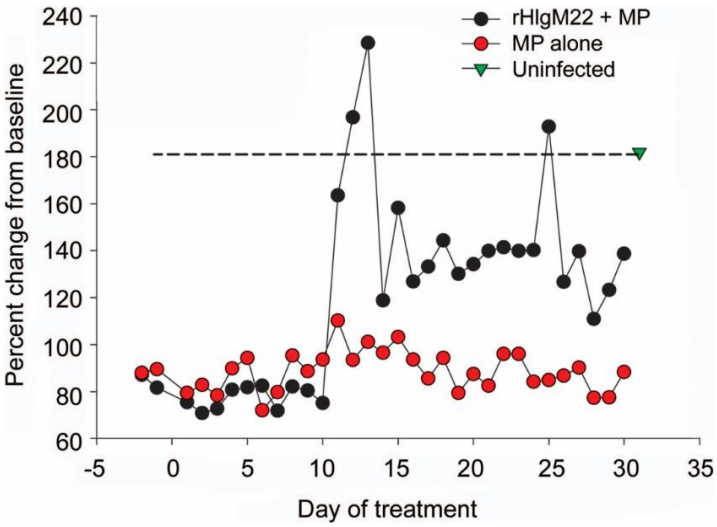

Figure 4: rHIgM22 increases body movement in mouse model of MS. Effectiveness of rHIgM22 in addition to the standard MS treatment, methylprednisolone (MP), was measured by change in mouse mobility. Movement was detected in activity boxes equipped with infrared beams which record beam breaks when mice move. Mice were infected with TMEV (a mouse model for MS), resulting in a decrease in body movement. A baseline level of activity was measured before and during drug treatment. All mice were given MP (1 mg twice per week), and one subgroup was also given a single 500 μg dose of rHIgM22. Mice given MP alone (**red circles**) had almost no change in body movement. Mice also given rHIgM22 (**black circles**) had a significant increase in body movement. Figure reproduced with permission from: Rodriguez, Warrington, and Pease. Invited Article: Human Natural Autoantibodies in the Treatment of Neurologic Disease. Neurology 2009, 72 (14), 1269–1276.[4]

rHIgM12, the second major antibody discovered and developed by the Mayo researchers, has potential to help people with ALS. This antibody is still being researched and has not reached clinical trials yet. In neuronal cell cultures, rHIgM12 has been shown to extend neurites as powerfully as the biomolecule laminin[5]. This behavior can be seen in Figure 5. PDMS stamps with grid patterns "inked" with the antibodies rHIgM12 and rHIgM22, were used to transfer and immobilize the antibodies onto glass coverslips. Neurons were then seeded onto these coverslips. Fluorescent secondary antibodies label the location of stamped antibodies (green) and growing neurons (red). The neurons followed patterns of rHIgM12, but not rHIgM22, indicating rHIgM12 is a signaling molecule which can direct neurite outgrowth.

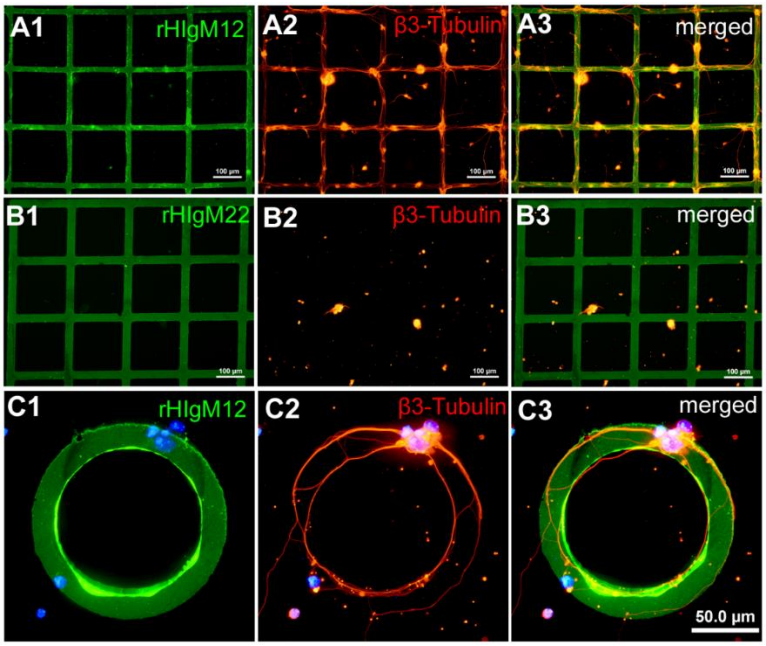

Figure 5: Neurons follow patterns of immobilized rHIgM12. Fluorescence micrographs of mouse spinal neurons seeded onto glass coverslips coated with patterns of either rHIgM12 or rHIgM22. IgMs are shown in **green** (FITC-labeled anti-human IgM secondary antibodies). Neurons are shown in **red** (anti-β3-tubulin antibodies, which label the cytoskeletal microtubules in neurons). Patterned rHIgM12 is shown in (**A1-A3**) and (**C1-C3**). Patterned rHIgM22 is shown in (**B1-B3**). Cells attach and neurites follow rHIgM12, but not rHIgM22. Figure reproduced from: Xu, et al. Sci. Rep. 2013, 3, 2267.[5]

In TMEV mice, administration of rHIgM12 increased the activity of affected mice, as can be seen by an increase in the number of beam breaks shown in Figure 6.

Known Binding Behavior of the Antibodies

These antibodies bind to a few different cell types in the nervous system, but the cells to which they bind and induce large beneficial effects are shown in the fluorescence images of Figure 7. rHIgM22 binds to oligodendrocytes (panels A1-A4), whereas rHIgM12 binds to neurons (panels B1-B4). Fluorescent secondary antibodies were added to reveal the locations of the antibodies and cells. The secondary antibodies which bind to the IgMs are green fluorescing (FITC-labeled) anti-human IgM antibodies. The secondary antibodies which bind to the cells are red fluorescing anti-myelin oligodendrocyte glycoprotein

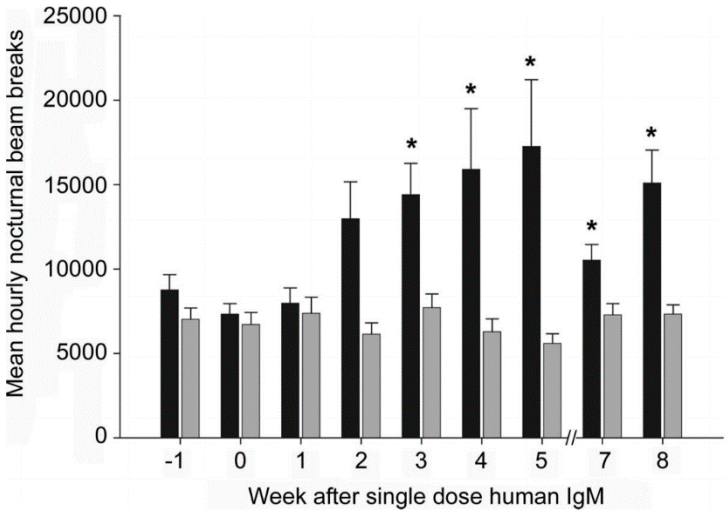

Figure 6: rHIgM12 increases movement in mouse model of ALS. Mice were infected with TMEV (a model of ALS), resulting in decreased movement, as measured by number of infrared beam breaks in activity boxes. One group of mice received a single 100 μg dose of the neurite extending rHIgM12 (**black bars**), while another group received a control human IgM which does not bind to neurons (**gray bars**). Mice with rHIgM12 exhibited a significant increase of movement, whereas mice given the control antibody showed no sign of improvement. Figure reproduced with permission from: Rodriguez, Warrington, and Pease. Invited Article: Human Natural Autoantibodies in the Treatment of Neurologic Disease. Neurology 2009, 72 (14), 1269–1276.[4]

(MOG, a protein on the surface of oligodendrocytes) or anti-β3-tubulin antibodies (a protein in neurons).

The transport in the body of these antibodies has been very surprising, running counter to conventional understanding. These antibodies have to cross the blood-brain barrier to reach their target nervous system cells. The blood-brain barrier is a membrane that surrounds the brain and spinal cord and only lets in small molecules by active transport (such as glucose) or diffusion (such as gases and hormones). However, these antibodies are large molecules. As IgMs (immunoglobulin class M), they are pentamers of IgG antibodies, giving them a hefty mass of more than 900 kDa. Large molecules such as these are not known to cross the blood-brain barrier. But MRI studies on mice with radioactively labeled IgMs injected into the body cavity have shown clearly that it crossed into the CNS.

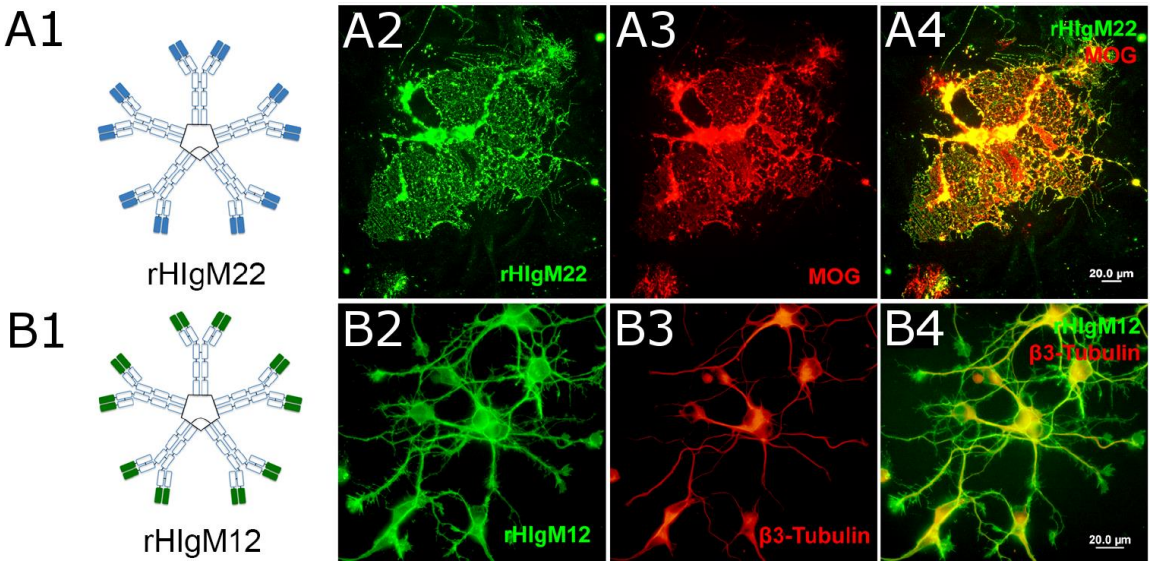

Figure 7: rHIgM22 and rHIgM12 bind to different cell types. Illustrations and fluorescence micrographs of IgMs bound to oligodendrocytes or neurons. (**A1-A4**) rHIgM22 (**green**) binds to oligodendrocytes (**red**). (**B1-B4**) rHIgM12 (**green**) binds to neurons (**red**). Details of the fluorescent secondary antibodies can be found in the text. Figure adapted from: Xu, et al. Sci. Rep. 2013, 3, 2267.[5]

Another unique aspect of these antibodies is that they are natural autoantibodies, a surprising class of antibodies. Unlike the typical antibody targets, which are foreign molecules (as a flag for destruction), natural autoantibodies bind to the body's own molecules. They are "germline", meaning they show up before an individual's immune system has developed, by being coded in the genes. And unlike the very specific binding of typical antibodies, they are polyreactive, meaning they bind to many different types of molecules. With this polyreactivity, they have much lower affinity for their targets, meaning they do not bind strongly to these targets.

The functions of natural autoantibodies had remained a mystery for decades, but many functions are being discovered. One function is to bind to debris such as DNA and damaged lipids from the billions of dying or dead cells, as flags for removal by macrophages and dendritic cells. Many natural antibodies, up to one third of those studied, also bind to and aid in cleanup of oxidized waste products from the metabolism of cells, such as oxidized low-density lipoprotein (LDL). They can also bind to pathogens directly

or can work in conjunction with other molecules, such as carbohydrate-binding lectins, to indirectly kill the microbes. In addition, they can bind to immune cells such as macrophages and appear to reduce macrophage death by altering the way they digest debris.[6,7]

To help understand the binding properties of these antibodies, the Mayo Clinic researchers teamed up with our lab at the University of Minnesota to develop technology that could validate proposed molecular binding partners and measure their affinity and kinetics. The theory behind the affinity and kinetics of molecular interactions and experimental methods to measure these properties will be discussed in the following section.

2.2 Affinity and Kinetics

Generally, for a drug to cause a physiological change, it must bind to a molecule in the body that is associated with a disease. Usually the target molecule is either an enzyme or a receptor on a cell surface, and the drug either blocks or enhances its normal physiological function. A common approach by the pharmaceutical industry when searching for new drugs is to start by looking for the strongest binding chemical compound to the target receptor or enzyme.[8,9] A stronger binder stays in its target longer, prolonging its physiology effect, resulting in a smaller dosage and less frequent dosing of the drug. There are exceptions to this rule, as some diseases benefit from a short effect, but many diseases benefit from longer effects. Therefore the binding strength of drug candidates to their targets is a key parameter to measure.

Recently it has been argued that another metric other than the binding strength is more predictive of a drug's success - the kinetics of the molecular interaction.[8,9] Binding strength is an equilibrium concept, whereas kinetics are the rates of the chemical reaction that result in that equilibrium.

The simplest chemical model of the molecular interaction between a drug and receptor is shown in Equation (1)

$$A + B \underset{k_d}{\overset{k_a}{\rightleftarrows}} AB \quad (1)$$

where A represents the drug, B represents the receptor, and AB represents drug bound to receptor. The reaction occurs in both directions. In the forward direction, reactants A and B bind together (association), and in the reverse direction, the complex AB unbinds (dissociation).

The study of kinetics is the study of the rates, or speed, of the reaction. Many drug-receptor reactions are first order reactions, meaning the rates are dependent on the concentrations of the reactants and products. Binding events occur due to collisions and correct orientations between the drug and binding site, and are held together by the sum of electrostatic, van der Waals, and hydrogen bond forces. An increased concentration of reactants will result in a more rapid and greater number of collisions and bound drugs. Conversely, the unbinding event occurs solely due to thermally driven motion overcoming the binding forces.

The rate of the forward reaction is proportional to the concentrations of the drug and the receptor and a proportionality constant termed the association kinetic rate constant, k_a:

$$rate_{forward} = \frac{d[AB]}{dt} = k_a[A][B] \quad (2)$$

The rate of the reverse reaction is proportional to the concentration of the complex AB and a proportionality constant termed the dissociation kinetic rate constant, k_d:

$$rate_{reverse} = -\frac{d[AB]}{dt} = k_d[AB] \quad (3)$$

As the concentrations change during the reaction, these rates also change, until they reach a balanced state with the forward rate equal to the reverse rate, in a state of dynamic equilibrium. In this steady state, drug and receptor molecules continue to bind and unbind, but the overall concentrations of reactants and products are no longer changing:

$$rate_{forward} = rate_{reverse} = \frac{d[AB]}{dt} = k_a[A][B] = k_d[AB] = 0 \qquad (4)$$

The strength of the reaction is described by the equilibrium dissociation constant, K_D. This constant is defined as the concentration of drug needed to fill half of the receptors. It can be derived from the rate equations by some rearrangement to get:

$$K_D = \frac{[A][B]}{[AB]} = \frac{k_d}{k_a} \qquad (5)$$

where [A] is the concentration of A which results in half of B being bound to A.

A low K_D indicates a strong binding molecular pair. Only a low concentration of drug is needed to fill half of the receptors at equilibrium. A low K_D could be due to a large k_a, or a small k_d. As mentioned above, these kinetic rate constants may be better than K_D for predicting a drug's success, in particular a small k_d. In the next section, a common method for obtaining kinetic rate constants will be described.

SPR Kinetic Experiments

A common technique to measure reaction kinetics is with a surface plasmon resonance (SPR) biosensor. These instruments typically contain a planar sensor in which one of the reactants are attached to the surface, while the other reactant is flowed over the surface. For drug studies, a common orientation is to attach the target of the drug to the sensor surface, and flow over multiple drug candidates.

A schematic of a nanohole array based SPR instrument is shown in Figure 8. To generate surface plasmon resonance, broadband light is directed onto the chip. It passes through PDMS and a solution and impinges on the metallic film. Surface plasmons are generated and resonate, and tunnel through the nanoholes, then re-emit as photons light on the opposite side. This transmitted light enters a spectrometer, impinges on a grating, spreading the light into its component wavelengths which then get collected by a CCD.

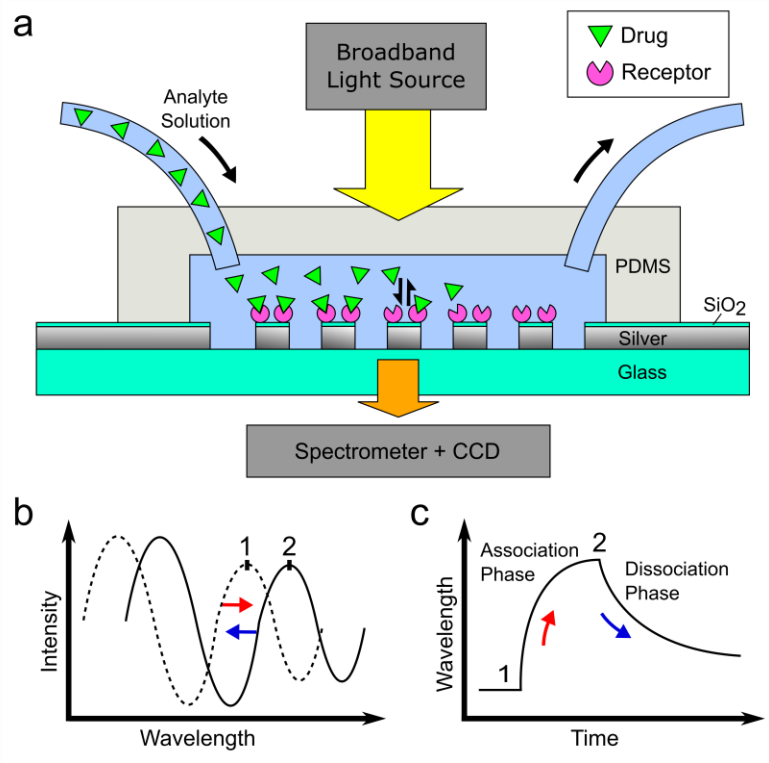

Figure 8: Schematic of SPR instrument and data obtained during a binding kinetics experiment. (**a**) The microfluidic chip is composed of two parts: a plasmonic sensor base (glass slide with a silver film with nanoholes) bonded to a flow-cell top (transparent polydimethylsiloxane (PDMS)) through which solutions of molecules can be injected. The chip is placed on a microscope stage. White light projects onto the chip and generates surface plasmons which resonate at the metal surface, tunnel through the holes and radiate as light. The light enters a spectrometer and is split into component wavelengths and collected by a CCD. The resonating plasmons are sensitive to the changes in the refractive index of the liquid above the surface. Receptors are injected into the chip and are immobilized on the surface. During a kinetics experiment, a drug is injected over those receptors. (**b**) If the drug binds to the receptors, there is a red shift in the surface plasmon resonant wavelengths (peak at position 1 shifts to position 2). During the washing phase, the drug unbinds from receptors, and the resonant wavelength blue shifts (peak at position 2 shifts to position 1). (**c**) Plotting the shift of the SPR peak over time enables calculation of the kinetic rates of the reaction.

The resonating SPR signal is strongest at certain wavelengths. As molecules accumulate on the surface, the dielectric (and refractive index) of the medium at the surface changes, and the SPR resonant frequency red shifts to longer wavelengths. By tracking the

peak or dip over time as solutions are injected and binding or unbinding takes place, the rate of reaction is measurable, without requiring any labeling of the molecules.

The SPR binding experiment consists of two phases – the association phase followed by the dissociation phase. The preparation for the experiment includes the attachment of the receptor to the sensor surface, and blocking exposed regions to prevent nonspecific binding of the drug on the surface. The experiment then begins with the association phase. In this phase the drug in solution is injected over the surface and can bind with receptors. During this phase, both binding and unbinding occurs. In terms of the chemical model, the full reaction takes place. Ideally, this phase is continued until equilibrium is reached, but it is not essential, and in some cases it is difficult to reach equilibrium. The next phase that takes place is the dissociation phase. In this phase, only buffer (without drug) is injected over the surface, and the only chemical reaction that occurs is the unbinding of the molecular complexes. Because only one reaction is occurring, and is concentration independent, it is best to start analysis with the dissociation phase.

Dissociation Phase

During the dissociation phase, buffer without drug is injected over the sensor surface. Bound drug can unbind and get washed away. In chemical formula terms, only the reverse reaction takes place:

$$A + B \underset{k_d}{\leftarrow} AB \tag{6}$$

Because the dissociation phase includes only the reverse reaction, the only unknown parameter that needs to be determined is k_d. The differential equations for dissociation are:

$$\frac{d[AB]}{dt} = -k_d[AB] = \frac{dR}{dt} = -k_d R \tag{7}$$

$$R = sensor\ response,\ R \propto [AB]$$

where R represents the sensor response (resonant wavelength shift) which is proportional to the concentration of complex AB. Rewriting equation (7) in the integrated form gives:

$$\int \frac{1}{R} dR = -k_d \int dt \tag{8}$$

$$\ln R = -k_d t + c \tag{9}$$

$$R = e^{-k_d t} e^{c} \tag{10}$$

$$R = R_a e^{-k_d t} \tag{11}$$

where R_a is the maximum sensor response at infinity, and t is time. The plot of the dissociation data over time has the form of an exponential decay curve. Curves can be analytically fit to the data using the above equation and the least squares fit method, to determine k_d.

Association Phase

Once k_d is determined, the association phase can be analyzed to find k_a. Both the forward and reverse reactions occur during the association phase:

$$\frac{d[AB]}{dt} = k_a[A][B] - k_d[AB] \tag{12}$$

Because the total receptor quantity is fixed and none are bound to drug at the beginning of the experiment,

$$[B]_0 = [B] \; at \; t = 0$$

where $[B]_0$ equals the total receptor concentration, which is the maximum amount of complexed molecules, R_{max}.

$$R_{max} = response \; when \; all \; receptors \; filled \tag{13}$$

$$R_{max} = [B]_0 \tag{14}$$

As drug binds to the receptor, the amount of free receptor is the total receptor concentration minus the complexed receptor concentraion:

$$[B] = [B]_0 - [AB] \tag{15}$$

Equation (15) can be substituted into equation (12):

$$\frac{d[AB]}{dt} = k_a[A]([B]_0 - [AB]) - k_d[AB] \tag{16}$$

A key component of these experiments is to hold the drug concentration, [A], constant:

$$[A] = C \tag{17}$$

Thus the remaining variable is the sensor response, R, which is measured over time:

$$\frac{dR}{dt} = k_a C(R_{max} - R) - k_d R \tag{18}$$

The association phase data produces a curve that can be fit with the integrated form of this equation. The integration is as follows. First the terms are rearranged:

$$\frac{dR}{dt} = k_a C R_{max} - (k_a C + k_d)R \tag{19}$$

$$Let: \quad a = k_a C R_{max}, \quad b = k_a C + k_d \tag{20}$$

$$\frac{dR}{dt} = a - bR \tag{21}$$

Rearranging and integrating both sides:

$$\int \frac{1}{a - bR} dR = \int dt \tag{22}$$

$$Let: \ u = a - bR, \ du = -bdR \ \rightarrow \ dR = -\frac{1}{b}du \tag{23}$$

$$-\frac{1}{b}\int \frac{1}{u} du = \int dt \tag{24}$$

$$-\frac{1}{b}\ln u = t + c \tag{25}$$

$$\ln u = -b(t + c) \tag{26}$$

$$u = e^{-bt}e^{c} = ce^{-bt} \tag{27}$$

$$a - bR = ce^{-bt} \tag{28}$$

$$R = -\frac{ce^{-bt} - a}{b} = \frac{a - ce^{-bt}}{b} \tag{29}$$

$$at\ t = 0, R = 0, so:\ 0 = \frac{a - c}{b},\ \ c = a \tag{30}$$

$$R = \frac{a(1 - e^{-bt})}{b} \tag{31}$$

$$R = \frac{Ck_aR_{max}\left[1 - e^{-\left((Ck_a + k_d)t\right)}\right]}{Ck_a + k_d} \tag{32}$$

Equation (32) gives a curve that describes the association data. Fitting this curve by the least squares method to minimize the error determines k_a. Now both kinetic rate constants have been determined. Their ratio, k_d/k_a gives the equilibrium dissociation constant, K_D.

A case of two dissociating rate constants to describe two dissociating events, such as a fast and slow decay, can be expressed as (33):

$$R = R_ae^{-k_{d,fast}t} + R_be^{-k_{d,slow}t} \tag{33}$$

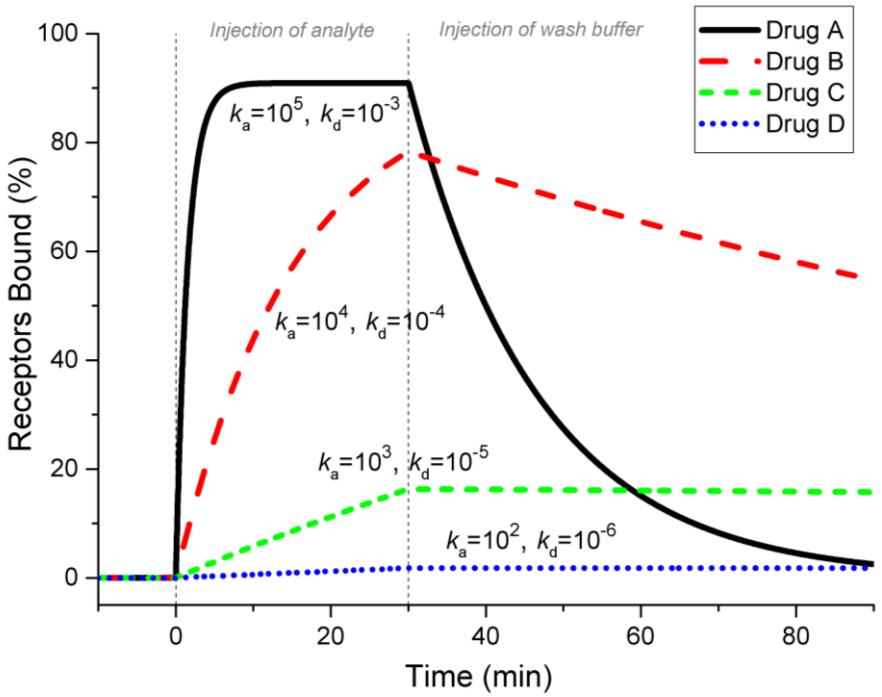

Figure 9: Drugs with the same dissociation equilibrium constant, K_D, may have very different kinetic rate constants, k_a and k_d. Analytically derived kinetic curves show four hypothetical drugs (A, B, C, and D) having the same affinity (K_D = 10 nM), but different kinetic rate constants (listed beside each corresponding curve). This plot illustrates how the standard K_D parameter does not capture all aspects of drug binding behavior. The half-life of drug in receptor, $t_{1/2}$, varies wildly for each drug. Drug A complexes with its target quickly, but also dissociates quickly ($t_{1/2} \approx 12$ min), whereas drugs B, C, and D stay bound for much longer ($t_{1/2} \approx 2$ hr, 19 hr, and 8 days). The off rate, k_d, is in many cases an improved predictor of the effectiveness of a drug.[8,9]

Kinetic Dissociation Rate Constants Give More Information

The reason why determining the kinetics constants are better than just the thermodynamic constants given by the commonly performed enzyme-linked immunosorbent assays (ELISA), is that drugs with the same K_D can have different rate constants. A hypothetical example of this is depicted in Figure 9. This figure plots the kinetic equations for four drug candidates, all with the same K_D, but varying k_a and k_d by one order of magnitude each. Another way to think about the k_d is by the half-life, $t_{1/2}$, which is the time it takes for half of the drug to unbind. The equation that relates these two parameters:

$$t_{1/2} = \frac{\ln(2)}{k_d} \tag{34}$$

The half-lives for the hypothetical drug molecules A, B, C, and D are $t \approx 12$ min, 2 hr, 19 hr, and 8 days. The smaller the k_d, the longer the residence time of the drug in its target. While a drug with a higher k_a initially forms complexes more rapidly than a drug with a lower k_a, this could be overcome by giving a larger dose of the drug with a low k_a. Also, a low k_a may be less significant for drugs that are uptaken into cells, because the chance for rebinding after unbinding increases the effective local concentration.

2.3 The Sensor

Surface Plasmon Resonance Biosensors

Surface plasmon resonance (SPR) sensing is a useful technique for measuring biomolecular interactions because molecules do not need conjugated reporter tags (e.g., fluorescent or radioisotopic), and the measurements of the binding reaction can be collected in real-time, allowing determination of kinetic rates. SPR sensors function as thin-film refractometers, detecting changes in the refractive index of a dielectric medium (e.g., air or water) immediately adjacent to the metal surface. The effective refractive index at the surface increases when drug molecules are injected over and bind to receptor molecules attached to the metal surface. As the refractive index increases, the SPR resonant wavelength increases proportionally.

Surface plasmon resonance derives its name from (1) the phenomenon occurring at the surface of the metal, (2) electrons in the metal behaving as a plasma (i.e., moving together as an electron cloud around positive nuclei), and (3) this plasma resonating at certain frequencies of applied external electromagnetic fields. A plasmon is the smallest unit, or quantum, of the collective oscillations of the free electrons in conductive mediums.

The first observation of plasmons was in diffraction gratings in metal in 1902 by R.W. Wood at Johns Hopkins University.[10,11] He noticed that at some angles of light directed on the grating, the reflected and refracted light was extinguished. It took many decades to

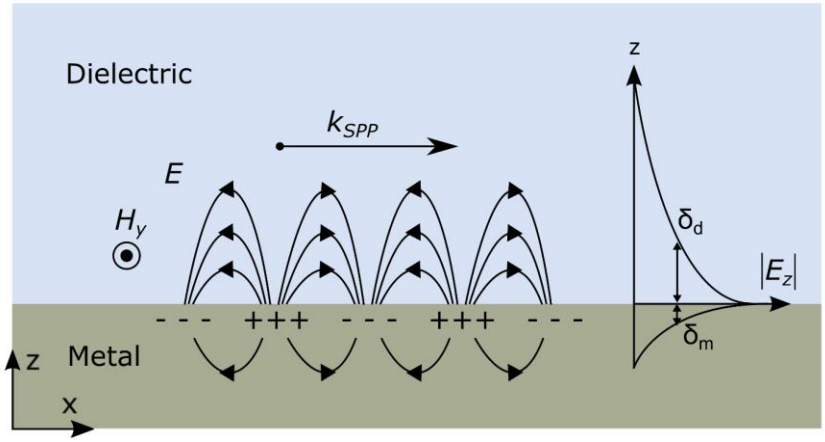

Figure 10: Surface plasmon polariton at a metal surface. With appropriate excitation configurations, photons of light can couple to the free electrons in a metal, creating travelling surface plasmon polaritons (SPP), which are collective oscillations of electrons at the surface of a metal, creating an electromagnetic field that decays away from the surface, and can be used for thin film sensing.

deduce that this light extinction was due to light energy coupling to and oscillating the plasma instead of reflecting off of the metal.[12–19]

At the interface of the metal conductor and dielectric medium, surface plasmons generate an evanescent electromagnetic field that decays exponentially into both media, as can be seen in Figure 10. The plasmon ripples along the surface as a surface plasmon polariton (SPP) with wavelength, λ_{spp}. A polariton is a coupled electromagnetic wave with an electric excitation. Gold and silver are the most commonly used metals for plasmonics, since they dampen surface plasmons the least, although other metals have been used, such as copper and aluminum. The dielectric material are gases or liquid solutions of chemical and biological molecules. The electromagnetic waves used to generate plasmons are most often in the visible regime, but other regimes are possible (e.g., UV, infrared, microwave).

One key element missing in Figure 10 is a coupler between light and the metal. To get massless photons to interact with relatively much bigger electrons in the metal, a special configuration is needed. The most common configurations utilize either prisms in the Kretschmann or Otto setups,[20–22] gratings,[10,11] or waveguides. The most successful instrument commercially, which has been around since the 1990s, is the Biacore line of

instruments (GE Healthcare), which use the Kretschmann configuration.[23] Prisms are good couplers, giving ~10x greater sensitivity than the grating method.[24] The downsides are that the spot size is larger resulting in lower throughput, and some alignment of the light source and detector is necessary for a home-built instrument, although they are pre-aligned in commercially available instruments. One downside of these top-of-the-line commercially available instruments is that they can cost up to hundreds of thousands of dollars. However, the upside is that some are fully robotically automated, so all that is needed is pipetting the starting solutions into Eppendorf tubes. The experiment can be set up to run overnight, enabling higher throughput.

For the prism method, a thin metal film (50 nm) is coated on the surface of the prism. Broadband light is directed through one of the angled sides of the prism, hitting the metal surface at an angle. At the angle at which light is totally reflected (total internal reflection), some wavelengths do not reflect, instead transducing their energy into plasmons. The prism causes the reflected light to spread out into its component wavelengths, which then get collected by a charge coupled device (CCD). The wavelengths that induce SPR do not get reflected and appear as a dark band. As molecules bind to the metal surface, the angle which induces plasmon resonance changes and the dark band shifts position. The first chemical sensing and immunosensing with SPR was performed by Nylander et al.[25,26]

Nanohole Arrays SPR Sensors

In this research project, the sensor architecture consists of a thin metal film with an array of subwavelength holes, or "nanoholes", a structure more similar to the gratings than prisms. This approach originated from a surprising discovery made by Ebbesen et al. in 1998[27] regarding metallic films with holes smaller than the wavelength of light. Light theory by Bethe[28] predicts that the intensity of light passing through subwavelength holes should drop by the 4^{th} power of the ratio of hole radius to light wavelength. Instead, Ebbesen et al. found a much higher amount of light made it through an array of nanoholes, as much as unity (when normalizing to the hole), naming the effect "extraordinary optical transmission" (EOT). They attributed this extra energy due to surface plasmons, with the

nanoholes acting as a funnel in which light energy gets converted to surface plasmons which funnel through to the opposite side and reradiate as a photon, thanks to the grating-like effect of the nanoholes.

The discovery of the EOT effect spurred research into nanohole arrays as SPR sensors. Efforts have been made to improve sensor characteristics. To increase signal to noise, one structural modification explored overlapping holes[29] which could create more intense plasmonic "hot spots" where the two holes met. Another design modification included Bragg-mirrors, which are a series of grooves surrounding the arrays to reflect plasmon waves to create isolation from other sensing spots, allowing for greater signal and more sensors/chip, leading to higher throughput.[30–32] The first demonstration of biosensing with nanohole arrays was by Brolo et al.[33] Nanohole arrays also present other interesting opportunities. They have been explored as nanochannels, which causes all of the analyte to pass very close to surface attached receptors, giving a much higher level of detection in a sample.[34,35] The nanoholes could enable studies with hole-spanning biologically mimicking lipid bilayers embedded with transmembrane proteins with access to both sides of the proteins for studies of functional changes in protein behavior upon binding by drugs. Other improvements have included surface coatings to improve stability of silver which can oxidize easily.[36] Special architectures have allowed receptors to be confined in certain regions to increase the detection limit.[37] In addition, others have found ways to make these arrays by cheaper methods.[38]

The nanohole array configuration is useful in that it has very simple optical alignment and can easily be multiplexed. These nanohole array chips are fabricated on standard glass slides which can be used on any microscope, without special and more difficult to setup optical alignment components.

Across all sensor architectures, the SPR resonance is monitored by either wavelength modulation, angle modulation, or intensity modulation. Each has its advantages and disadvantages. An advantage of intensity based SPR is its capability to do not just a single measurement, but 2D images of measurements. An initial proposal for this research project was to include 2D imaging, but this technique also has some downsides, the biggest being

that it is more sensitive to fluctuating intensity from the light source. As a less high throughput but more stable alternative, we chose to multiplex our measurements using an imaging spectrometer to conduct 1D spectral measurements (from a line on the chip), which still allowed us to collect spectra from multiple channels at once.[39]

Another helpful advance for SPR sensors has been regarding surface chemistry. A popular and successful surface coating on Biacore chips has been a 100 nm thick hydrogel carboxymethylated dextran surface, which receptors can be conjugated to, increasing the total amount of analyte that can be captured, leading to a larger resonance change and SPR resonance shift.[40–45]

SPR Instrument Used in These Experiments

The equipment used in the kinetic experiments for this dissertation consisted of nanohole array based SPR sensor chips, an inverted optical microscope, and an imaging spectrometer. The basic setup can be seen in Figure 11.

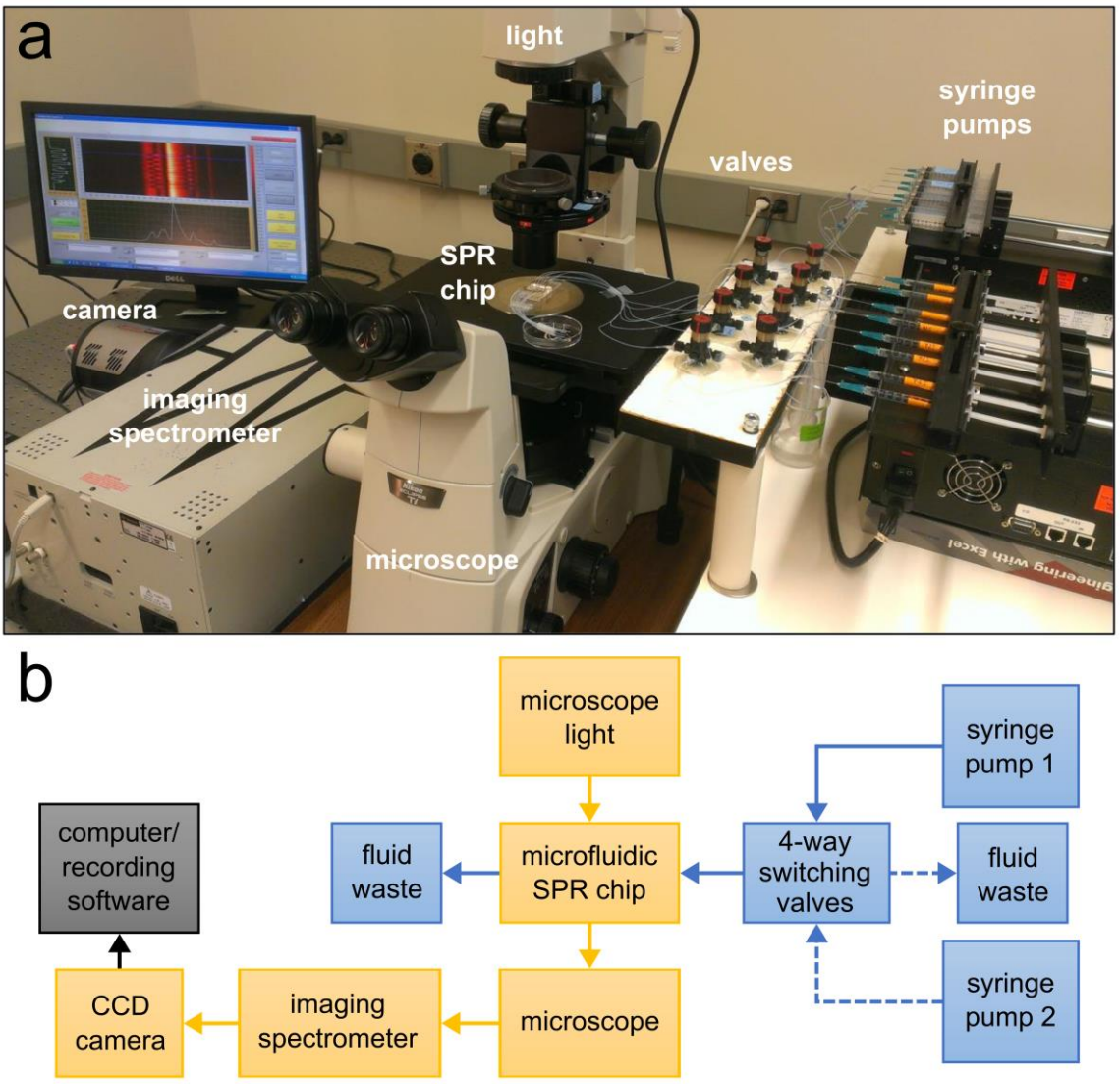

Figure 11: Binding kinetics experimental setup. (**a**) Image of experimental setup. Syringe pumps (right) push syringes filled with various solutions of rinsing buffer, receptors, or analytes through tubing and valves, to a microfluidic SPR chip on the microscope stage (center). White light is projected onto the chip, and SPR transmits certain wavelengths through the chip and into a slit in the imaging spectrometer (left), hitting a grating which spreads the light into its component wavelengths, which get collected on a CCD camera. A false colored image and intensity line profile can be seen on the computer screen. (**b**) Schematic of setup.

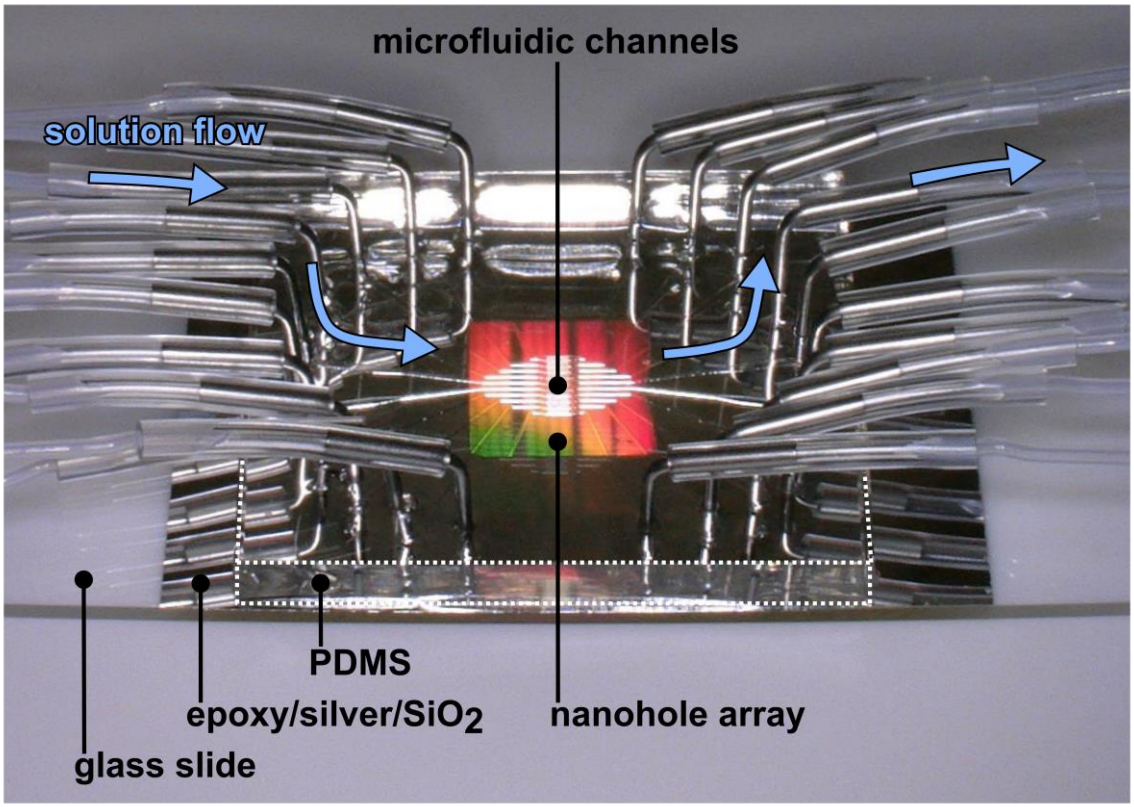

Figure 12: Microfluidic SPR nanohole array device. The device consists of the plasmonic sensor, which is a glass slide coated with a thin (100 nm) silver film with a square array of billions of nanoholes (~150 nm diameter, 500 nm periodicity, visible as an iridescent square in the center), coated with a thin SiO_2 layer (~15 nm), bonded to a transparent PDMS slab (3-4 mm thick) with multiple channels (50 × 100 μm) inset in its base. This microfluidic design features 10 channels, each which splits into 5 channels in the center of the nanohole array, giving a total of 50 channels. Chips used for the Mayo antibody binding kinetics experiments were of a simpler 8 channel design because it was easier to work with. Solutions are injected through the silicone tubes connected to the metal tubes which penetrate into the PDMS and connect to the channels.

Microfluidic Chip with Large Area Nanohole Array

The Oh lab designs and develops plasmonic sensors. One of our accomplishments has been the development of a large area nanohole array[46] which can be seen in the middle of the chip in Figure 12. A useful advantage of using nanohole array based chips is that the light is perpendicular to the chip, so it is very simple setup, and can be used with microscopes already in most labs. A significant advantage of a large area of nanoholes is

a stronger transmission signal. Other benefits include simple alignment of the PDMS chip during chip fabrication and ease of finding the array during experiments.

To fabricate these large area nanohole arrays, we used a combination of nanoimprint lithography and template stripping methods. We first spun-coated thermal resist on ~25 × 25 mm silicon wafers. We then used a nanoimprinter to press an 8 × 8 mm silicon mold with a surface consisting of a square array of circular pillars (~200 nm diameters, spaced 500 nm apart) into the thermal resist of the first silicon pieces, and cured the resist with heat, creating a mask with the inverse of the pillars, i.e. holes. To etch into the silicon wafer, we used a deep trench etcher, followed by removal of the nanoimprint mask, resulting in a silicon mold of a large area nanohole array. To make the sensor, we deposit a metal on this silicon nanohole array mold. We then use a template stripping method, in which we transfer the metal to a glass slide. We first put a drop of UV curable epoxy on a glass slide and place the mold on it. Then we cure the epoxy with a UV light. Finally, the silicon mold can be removed, leaving the glass slide covered with the metal with nanohole array. Because the mold was an ultrasmooth silicon wafer, this smoothness gets transferred to the metal which is great for plasmonics, giving a 2-5× better signal.[47] This silicon mold also can be cleaned and reused, allowing repeated metal depositions and template stripping to produce many chips, significantly driving down the cost and time to make each chip.

The upper half of the chip is a simple microfluidic chip made of polydimethylsiloxane (PDMS). We have made microfluidic chips with many channels (n = 50, 15 μm wide, 30 μm walls in between channels) but one of the challenges is interfacing this with the macroscopic world, i.e. syringes and syringe pumps. Also, it becomes harder to avoid leaks

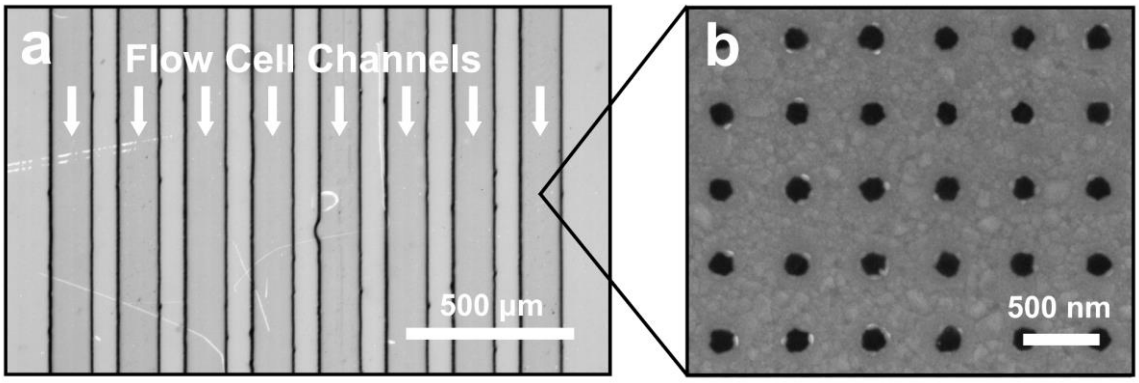

Figure 13: Microfluidic channels and nanohole array surface of the SPR chip. (**a**) Brightfield micrograph of PDMS microfluidic channels of the SPR chip (top down view). White arrows indicate direction liquid flow in the 8 channels. Channels are 100 µm wide and 50 µm tall, and have 100 µm thick walls between them. (**b**) Scanning electron microscope micrograph (SEM) of the nanohole array in the silver film. Holes have diameters of ~150 nm with periodicity of 500 nm. In both (**a**) and (**b**) the conditions are dry, and the SEM is taken before PDMS has been bonded to it. This figure was adapted from this author's publication: Xu, et al. Dis. Model. Mech. 2015, 8(8), 831-842.

because the pressure increases as the channels narrow (pressure = force/area: as the area goes down, the pressure goes up). So we settled on a simple 8 channel design which we had validated already: 100 µm wide channels with 100 µm wide walls between channels. To make these we used standard soft lithography. First the pattern was designed using computer software (AutoCAD) and sent to a company which printed it on film with high resolution. We then used photolithography to transfer this design to SU-8 polymer on a silicon wafer, resulting in channels made of hardened SU-8. PDMS was mixed and poured on the SU-8 mold, and cured overnight. The PDMS was cut and peeled off the mold, and holes poked at the inlets and outlets of the channels. Before use, it was cleaned with acetone, methanol, isopropanol, and water, and blown dry with N_2 gas. A top down image through PDMS chip and a scanning electron microscopic image of the sensor can be seen in Figure 13.

Thin SiO_2 Surface Coating

The nanohole array surface was coated with a thin, conformal SiO_2 coating.[46,48] This coating enabled two important capabilities: (1) permanent bonding to the PDMS chip

which helps prevent leaks, and (2) the formation of a biologically mimicking lipid bilayer by inducing rupture of lipid vesicles, which will be discussed in the next section. To make this thin coating, we used an atomic layer deposition (ALD) machine (Cambridge Nanotech, Savannah model). This allowed us to make a 12-18 nm thick conformal film on the chip. When we made nanohole arrays with the cheaper silver instead of gold, this offered an additional benefit: prevention of oxidation of the silver, which can reduce the SPR signal.

Imaging Spectrometer

The imaging spectrometer used in these experiments allowed for higher throughput experiments, and could allow up to 50 channels at once. A schematic of the light path through the SPR chip and inside the imaging spectrometer, and the subsequent recorded CCD output can be seen in Figure 14. The logistics of manually injecting this high number of solutions was challenging to carry out, however. So for more manageable experiments, four channels were the typical number used during experiments in this dissertation.

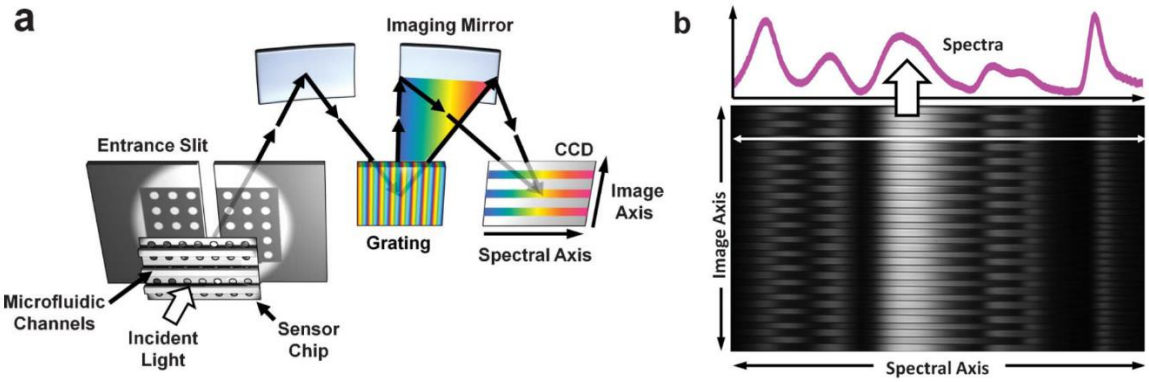

Figure 14: Imaging spectrometer schematic and data for multiplexed experiments. (**a**) Schematic of SPR chip (nanohole array + microfluidic channels) used with the imaging spectrometer. Light from the chip passes into the entrance slit of the imaging spectrometer, gets separated by a grating, and collected on a CCD, allowing simultaneous collection of spectra from multiple channels. (**b**) CCD photograph and a plot of the line profile of the intensity (from the white line). Figure reproduced and adapted from Lee et al., 2012 by permission of The Royal Society of Chemistry.[39]

2.4 Supported Lipid Bilayers

Coating the Sensor with Lipid Bilayers

The Mayo antibodies bind to unknown receptors in cell membranes, so the methods we proposed to attach receptors to the sensor surface were to either (1) use processed membrane extracts (for rHIgM22) or (2) form a mimic of the cell membrane on the sensor surface, a supported lipid bilayer, and incorporate hypothesized receptors (for rHIgM12).

Lipid bilayers are two dimensional fluid membranes composed of lipids and proteins.[49] Most lipids are amphipathic molecules, which means they have a hydrophobic ("water fearing") hydrocarbon chain tail(s) and a hydrophilic ("water loving") headgroup. This amphipathicity causes them to self-assemble into micelles and spherical bilayers (vesicles, or liposomes) when placed in an aqueous solution (headgroups facing water and tails facing each other).

Various methods exist for forming a lipid bilayer on a surface. Some of the most common methods are: Langmuir-Blodgett film transfer[50] and vesicle rupture.[51] The vesicle rupture process is simple and has been studied in great detail by multiple modalities (AFM, QCM, SPR) and has been utilized in other biosensors.[52–62] We chose the latter technique because it could easily be incorporated in a microfluidic device. To make the vesicles used in the vesicle rupture method, lipids in organic solvents are first mixed in a vial and dried under vacuum, followed by addition of an aqueous solution, which induces formations of lipid vesicles.

These vesicles can be deposited on a surface and if the surface is hydrophilic enough, the vesicles can rupture on the surface and form a continuous lipid bilayer. The most typical surface used for vesicle rupture is silicon dioxide (SiO_2), also called silica. Typical microscope glass slides have a high percentage of silica, and vesicles are often ruptured directly on this glass after some cleaning/preparation steps to render it more hydrophilic. Metals, however, do not induce rupture and bilayer formation, so we used an atomic layer deposition (ALD) instrument to coat a thin (~15 nm), conforming layer of silica[48] on the surface of our sensors to facilitate vesicle rupture.

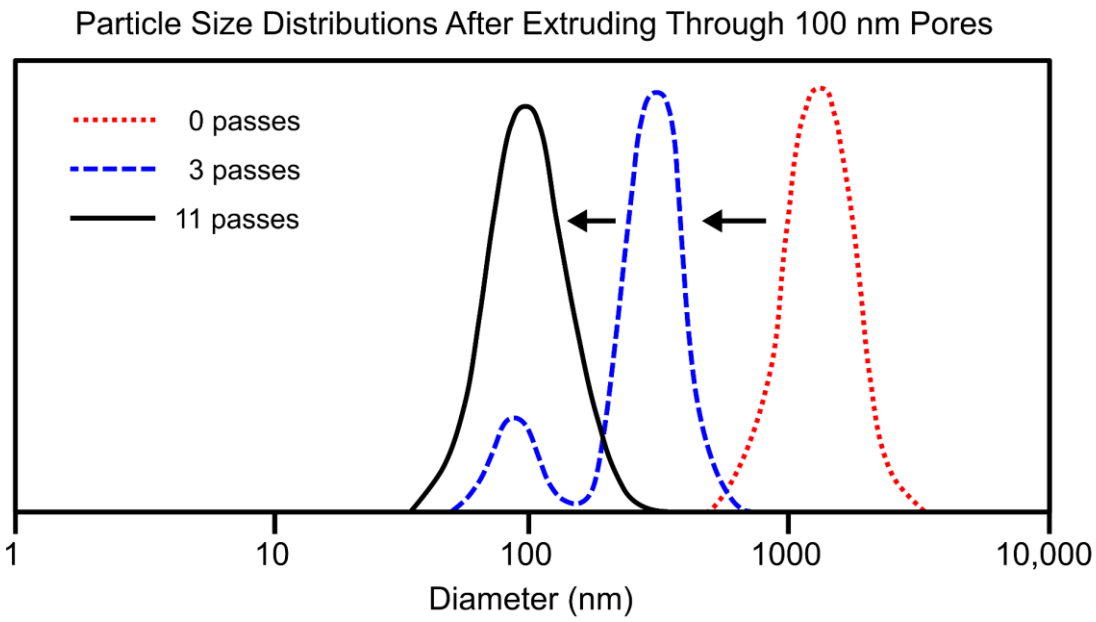

Figure 15: Extrusion process creates defined particle size. In the extrusion process, solutions of molecules can be passed through a polycarbonate membrane with pores of defined sizes, enabling formation of particles of defined sizes. With increased number of passes, the average particle diameter approaches the pore size. This figure depicts lipid vesicles extruded through pores with a diameter of 100 nm. The distribution starts centered near 1000 nm, and after 11 passes it has become centered near 100 nm in diameter. Figure adapted from Lasic, 2006.[63]

To fabricate small unilamellar vesicles (SUVs) less than 200 nm in diameter, a common method is to sonicate and then extrude the vesicles. Sonicating is the application of ultrasonic waves in a water bath which create air bubbles which expand and collapse, breaking the vesicles which then reform, resulting in smaller vesicles. In order to improve the lipid bilayer quality, it is helpful to form unilamellar (single layer) vesicles of a defined size before applying them to a surface to rupture. However, sonication results in multilamellar (multiple layered) vesicles of various sizes. To help with this problem, an extrusion process is also performed, in which vesicles are put through a filter with defined pore sizes, which breaks and reforms the vesicles, producing more unilamellar vesicles of a tighter size distribution[63], as seen in Figure 15. An additional treatment which can be performed is freeze-thaw cycling which increases encapsulation efficiency of soluble

molecules within the vesicles. In this study, no encapsulation was needed, so only sonication and extrusion were performed.

Fluorescence Recovery After Photobleaching

A simple way to confirm if the vesicles have ruptured and formed a planar lipid bilayer is by a fluorescence recovery after photobleaching (FRAP) experiment,[64] as shown in Figure 16. In a FRAP experiment to see if lipid vesicles have ruptured, typically fluorescent lipids are conjugated to some of the lipids in the vesicles. After the vesicles have been applied

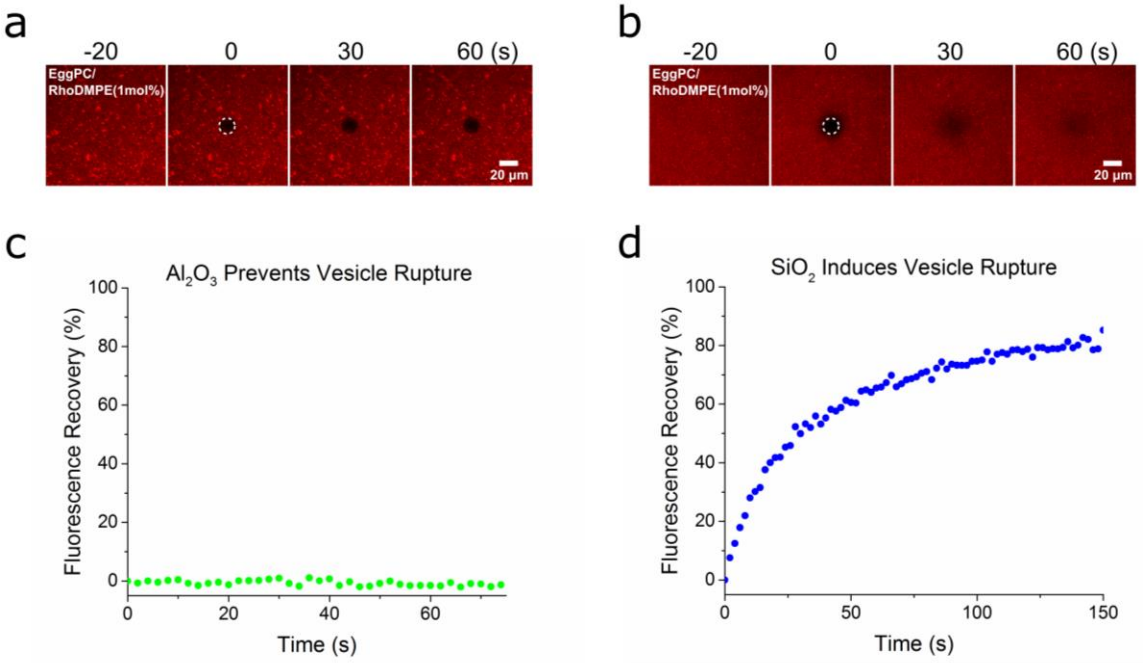

Figure 16: FRAP experiments confirm supported lipid bilayer formation. Fluorescence images (**a, b**) and analyzed data (**c, d**) from a fluorescence after photobleaching (FRAP) experiment confirms whether or not a supported lipid bilayer (SLB) has formed from vesicles (spherical lipid bilayers). Vesicles were applied to two surfaces: Al_2O_3 (**a, c**), and SiO_2 (**b, d**). Vesicles were composed of egg PC/Texas Red-DHPE (1% w/v). A laser was used to bleach fluorescent lipids in a circular region (indicated by white dashed lines in **a** and **b**), and the fluorescence intensity was measured in that region over time (**c, d**). Fluorescence does not recover on the Al_2O_3 sample indicating vesicles remained intact on the surface. Fluorescence recovers on the SiO_2 sample, indicating vesicles have ruptured and fused to form an SLB.

to the surface, the fluorescence of the surface is imaged. Then a bleaching step is performed, in which an intense light is directed on a section of the sample in order to destroy the fluorophores in that area. The fluorescence of the surface is then imaged for several minutes. If the vesicles ruptured and formed a planar bilayer, lipids will be diffusing laterally across the entire surface, the bleached molecules will diffuse away and unbleached molecules will diffuse into the bleached area (fluorescence recovery). If the vesicles did not rupture, and therefore are not continuous across the surface, they are unable to replenish depleted fluorescent molecules into the bleached area, so there will be no fluorescence recovery in that spot. A diffusion coefficient can be calculated from an exponential curve fit to the intensity recovery data. The time it takes to recover 50% of the final illumination is $t_{1/2}$, which can be entered into the following equation:

$$D = \frac{0.224\ r^2}{t_{1/2}} \tag{35}$$

where D is the lipid diffusion coefficient, and r is the radius of the bleached spot[65]. The diffusion coefficient for lipids in supported lipid bilayers is typically between 1-3 $\mu m^2/s$.

Hankel Transform Method

The Hankel transform method for analyzing FRAP data[66] offers some improvements to the traditional FRAP analysis methods. Some challenges with fluorescent lipid bilayers are low signal to noise, photobleaching during the long imaging sequences, uneven illumination during imaging, and a bleaching area without a well-defined bleached spot. One of the challenges with imaging lipid bilayers on reflective surfaces with a thin (less than 1 micrometer) transparent spacer, is that standing waves from incident or outgoing light can have destructive interference,[67] resulting in weaker fluorescence output, and can reduce efforts to bleach the bilayer, lengthening the bleaching duration. Ideally, the bleaching duration should be less than $1/10^{th}$ the characteristic diffusion time, τ_D ($\tau_D = r^2/4D$). The shortest bleaching duration we could obtain was roughly 10 seconds, when ideally it would have been less than one second. With this improved FRAP method,

fluorescence intensity of the bleached spot is radially averaged to reduce fluctuations in the weak fluorescence signal. This averaged intensity profile is then put through a Hankel transform, which is an alternate version of a Fourier transform, to perform spatial frequency analysis. This method therefore does not need to know the bleached spot profile, allowing for experiments with non-ideal bleach durations.

3 Kinetics of IgM O4 and rHIgM22 to Myelin Particles

3.1 Contributions

In this chapter, the SPR chip fabrication and experiments were carried out by the author. Experiments were planned and interpreted with the help of Nathan Wittenberg and Sang-Hyun Oh and our collaborators at the Mayo Clinic: Moses Rodriguez, Arthur Warrington, Xiaohua Xu, Jens Watzlawik, and Bharath Wootla. Antibodies and myelin membrane extracts were provided by these collaborators. Daehan Yoo helped make molds for the SPR chips, and several group members helped build the spectroscopy setup, including Nathan Lindquist, Tim Johnson, and Si Hoon Lee.

The findings in this chapter are unpublished, but are included here because they show progress in our aim to measure binding kinetics between rHIgM22 and myelin. Hopefully these results can provide some background for others who may continue this research. The problem we encountered was a surprising inability to detect binding between rHIgM22 and myelin. After several attempts to solve this problem, a second therapeutic antibody, rHIgM12, became a more feasible experimental target, so we shifted our efforts to study this second antibody, which is presented in chapter 4.

The partial progress we made on this project include the successful application of a membrane processing step, extrusion, to use native cellular membranes in SPR binding experiments. Using this extrusion method we were able to measure binding between mouse IgM O4 and native myelin membrane.

3.2 Introduction

Multiple sclerosis (MS) is an immune-mediated disease in which the body attacks its own oligodendrocytes and their myelin sheaths that wrap around the axons of neurons. Loss of myelin reduces signal conduction and protection of axons, and can lead to death of neurons

and formation of scars ("sclerae") in the central nervous system. Currently there is no cure for MS.

A surprising therapeutic approach to treat MS was discovered several decades ago when Dr. Moses Rodriguez and his colleagues serendipitously discovered several mouse antibodies that induced regeneration of myelin in mice. Among these antibodies was mouse IgM O4, a commercially available antibody commonly used to bind to and identify oligodendrocytes at a certain stage of development. The antibodies bound to oligodendrocytes and induced calcium influx into the cells. And in two mouse models of MS, the antibodies increased the amount of myelin sheathes and spontaneous body movement.

A mouse antibody could be toxic to humans, so Rodriguez and colleagues ingeniously searched for a human antibody in samples of human serum (the portion of blood without cells or coagulation factors). These serum samples came from human patients with macroglobulinemia, a disorder which produces an excess of antibodies. The researchers found some human antibodies that behaved in a similar fashion to the mouse antibodies. and developed one into a recombinant form, giving it the name rHIgM22. Animal efficacy studies confirmed rHIgM22 has the same therapeutic effects in mice. After passing toxicology studies in primates, rHIgM22 was entered into phase I clinical trials, which it recently successfully completed (identifier: NCT01803867, https://clinicaltrials.gov/ct2/show/NCT01803867).

The goal of this research project was to determine the binding kinetics (the rates of binding and unbinding) between rHIgM22 and an unknown receptor in myelin membrane of oligodendrocytes. Knowing the binding kinetics between a potential drug and its target in the body is useful because it can help to understand how it will behave in the body. In many drug strategies, it is useful to have a drug stay bound to its receptor for a longer period of time, thus increasing the duration of its physiological effect, as well as leading to a smaller drug dosage needed or longer time between doses.

To measure the binding kinetics between rHIgM22 and myelin, we chose to use a homebuilt surface plasmon resonance (SPR) biosensor. SPR is an optical phenomenon

which can be utilized to measure the binding kinetics between two molecules without needing the attachment of fluorescent or radioisotopic labels, which can alter binding behavior. To produce SPR, light is directed onto a metal film, and with the aid of a prism or grating, photons are coupled to free electrons in the metal and generate surface plasmons which resonate at certain wavelengths. These surface plasmons evanescently decay within a few hundred nanometers from the surface, and are where the binding reaction will take place. First one of the binding molecules, such as a receptor in a cell membrane as is the case with rHIgM22, gets attached to the surface in some manner. Then a solution of the second binding molecules is flowed over the attached receptors. As molecules bind to receptors on the surface, the plasmonic resonance shifts to longer wavelengths, a signal which gets detected and recorded. In a final step, a solution with no molecules is injected over the bound molecules, and as these molecules unbind and are washed away, the plasmonic resonance shifts back to shorter wavelengths. From the shifts during these two experimental steps, the rates of binding and unbinding can be calculated.

For the SPR sensor, we fabricated metal films perforated with an array of "nanoholes" – holes with diameters of nanometer dimensions (~150 nm in diameter, 500 nm periodicity). This nanohole array architecture allows for simple microscope alignment without the need for prisms or angled lights or detectors. Our lab has developed methods to fabricate a large area array (8 × 8 mm, > 200 million holes) which gives a larger signal and easy alignment during fabrication.[46]

For these binding experiments between rHIgM22 and myelin membrane, the receptor to be attached to the sensor surface was unknown. We proposed taking myelin membrane extracted from mice, which would include the unknown receptors, and passively adsorbing this extracted membrane to the sensor surface. The challenge with this approach is that SPR is a very thin film technique and can only detect changes occurring within a few hundred nanometers from the surface. Extracted myelin membrane particles are much larger, >1 μm in diameter. This large size is possibly due to the complicated multilayered structure of myelin with proteins acting as glue to hold layers together[68]. So, to reduce the particle sizes, we decided to use ultrasonication and extrusion through filter paper with

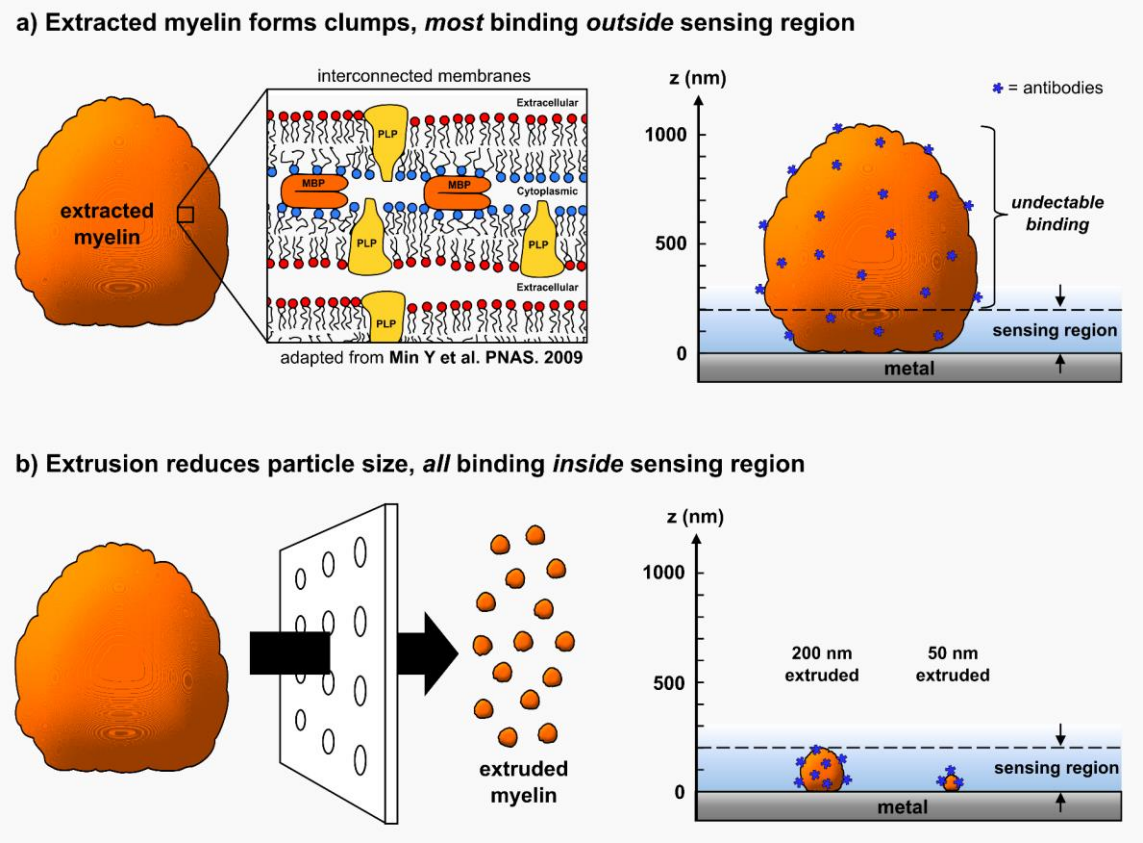

Figure 17: Extracted myelin particles were too large for SPR, so extrusion was used to reduce their sizes. (**a**) Myelin is a multilayered structure with many proteins interconnecting the layers, leading to extracted myelin forming micrometer-sized clumps. Most detection of rHIgM22 binding to the myelin would be outside the SPR sensing region, which is only a few hundred nanometers. (**b**) Extruding the myelin through a polycarbonate filter with defined pore sizes can reduce the particle size into the sensing window so all binding can be detected. Inset image in of myelin membrane in (**a**) is adapted from Min et al., 2009, copyright by the National Academy of Sciences.[68]

pores of defined sizes, a common procedure for forming lipid vesicles of defined sizes. This large particle challenge and attempted size reduction is depicted in Figure 17.

Figure 18 depicts the SPR sensor surface during a binding experiment, where a solution of IgMs interacts with adsorbed extruded myelin particles. A second antibody, mouse IgM O4, was also tested against myelin as a positive control to verify extruded myelin was present. The receptor of IgM O4 is sulfated galactocerebroside (sulfatide), a glycolipid in the lipid bilayer.

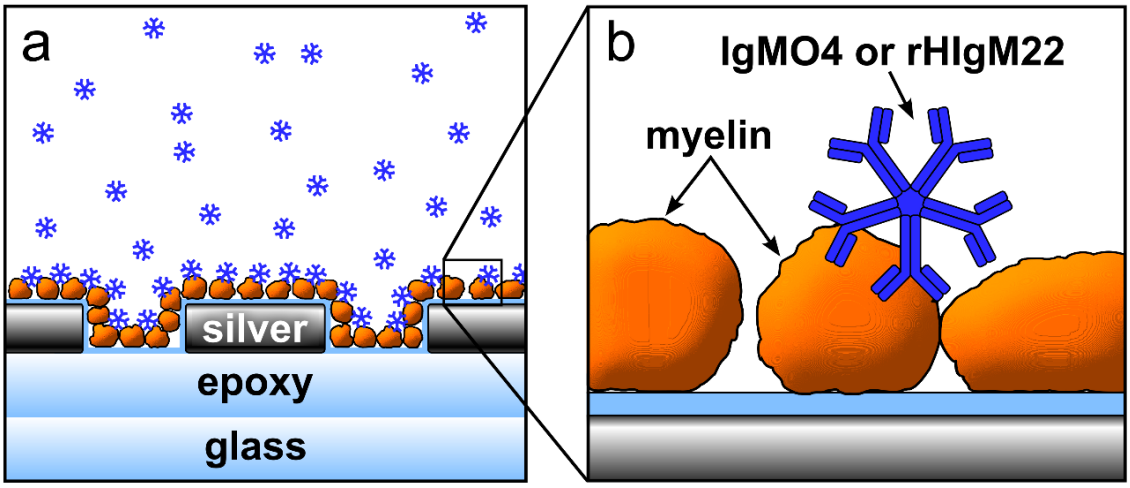

Figure 18: SPR chip coated with extruded myelin particles interacting with IgM O4 or rHIgM22. Schematic of the nanohole array sensor coated with extruded myelin interacting with a solution of IgM O4 or rHIgM22 during a binding kinetics experiment. (**a**) Chip consists of a silver film (100 nm thick) with nanoholes (~150 nm diameter, 500 nm spacing) on a glass slide, coated with SiO_2 (~15 nm thick) and bonded to a microfluidic chip. The surface is then coated by passive adsorption of extruded myelin particles, with nominal diameter of 50 nm or 200 nm. Mouse IgM O4 or rHIgM22 are then injected and binding is monitored. (**b**) Close-up view of the binding interaction.

Binding was able to be detected between mouse IgM O4 and extruded myelin, and the calculated equilibrium and rate constants were similar to previous studies. The calculated equilibrium rate constant was: $K_{D,\,apparent} = 2.6 \pm 3.6 \times 10^{-9}$ M. The calculated kinetic rate constants were, for association: $k_a = 2.5 \pm 0.0 \times 10^4\ M^{-1}s^{-1}$, and for dissociation: $k_{d,\,fast} = 6.8 \pm 0.7 \times 10^{-3}\ s^{-1}$ and $k_{d,\,slow} = 6.6 \pm 0.3 \times 10^{-5}\ s^{-1}$.

However, binding was unable to be detected between rHIgM22 and extruded myelin. Many conditions were varied to elucidate what factors might be the cause of this failure, but ultimately, none of the tested factors were responsible. After significant effort was given to this problem, a second potentially therapeutic antibody became a better target of study, and it was more crucial to gain the kinetics for it. Chapter 4 covers the pursuit of this binding pair. Unfortunately, we could not solve the undetectability problem of rHIgM22 to myelin, but it could be picked up and pursued at a later date. We gained some knowledge that the extrusion method and natural membrane method works for at least some

binding pairs. In addition, the extrusion process knocks out the receptor of myelin, which may help us discover the identity of the unknown receptor.

3.3 Materials and Methods

Antibodies

Antibodies were provided by our collaborators at the Mayo Clinic. Mouse monoclonal IgM O4 was produced by hybridomas and purified by PEG precipitation and gel filtration chromatography.[69] rHIgM22 was expressed in F3B6 cells. Original antibodies were obtained from serum of human patients with Waldenstrom's macroglobulinemia. The antibodies were sequenced, and the heavy and light chains were incorporated into plasmids which were then transfected into the cells. Control IgM came from human serum.[5]

Myelin Extraction

Myelin from SJL/J mice whole brains was isolated by our collaborators at the Mayo Clinic. Preparation of myelin was carried out in accordance with an established protocol.[69] It was tested for MOG, MAG, CNP, PLP, and MBP by anti-myelin antibodies by ELISA. Membranes were stored in a -20°C freezer.

Sonication

The first step to reduce the size of the myelin particles was ultrasonication. The myelin was enclosed in Eppendorf tubes and placed in an ultrasonic bath. Initially, the particles were sonicated for a total of 45 minutes (three 15 minute durations with brief rest periods in between to allow for some cooling). During this treatment, we observed that the water bath became quite warm. After early tests failed to detect binding between rHIgM22 and myelin (data not shown), we suspected heat from the bath could be breaking down antigens, so for the following experiments, we reduced the sonication time dramatically and lowered the bath temperature. Water in the bath sonicator was chilled to 6°C prior to sonication. Frozen myelin in PBS (1 mg/ml) was thawed and diluted with PBS. The diluted myelin

was sonicated for 15 s, let sit for 5 s to let it cool down, and then sonicated for 15 more seconds.

Myelin Extrusion

After sonication, myelin membrane was extruded (Avanti Polar Lipids) through a filter to create particles of defined diameters, a similar size reduction of lipid vesicles by this process was shown in Figure 15. The extrusion filter was a polycarbonate film with etched tracks, with pore diameters of either 200 or 50 nm. This procedure has been shown to reduce the size of vesicles from a wide distribution to a much tighter distribution centered around the diameter of the pore, after 11 passes. We were unable to achieve all 11 passes with myelin, as it became increasingly difficult to push the myelin through with each pass. By 7 passes it was very difficult to push through the 50 nm pores. For the 200 nm filter it was much easier. It is possible the filter may have been getting clogged with myelin. Reducing the number of passes could result in larger than expected myelin particles, and some material may have been getting left behind in the filter.

Immunohistochemistry

To verify rHIgM22 could bind to myelin membrane, extruded (50 nm) and unextruded myelin was incubated in 96 well plates. 100 µL of 50 µg/mL myelin was added to each well and allowed to sit overnight to dry out, followed by washing with 300 µL PBS twice. Each well was blocked with 100 µL 5 wt % BSA in PBS for 1 hr. Without washing, 100 µL of 50 nM rHIgM22 was added to wells for 1 hr, followed by washing with PBS 3X. Finally, 100 µL of 10 µM FM 1-43 or 0.010 mg/mL fluorescent 2nd anti-human antibody was added to wells and incubated for 1 hr, followed by washing and imaging.

Silicon Nanohole Array Mold

The sensors used in these experiments consisted of an array (periodicity = 500 nm) of nanoholes (diameter = 150 nm) in a silver film (thickness = 100 nm), covered by a PDMS microfluidic chip. First, a nanohole array in silicon was made using nanoimprint

lithography. A 100 nm thick thermal oxide was grown on a silicon wafer by wet oxidation at 1100°C for 11 min. The wafer was then broken into five ~30 × 30 mm pieces and rinsed with water and blown dry with N_2 gas. Thermal nanoimprint resist (NXR-1025, Nanonex Corp, NJ) was spin-coated at 3500 rpm for 1 min on the wafer pieces, followed by baking at 150°C for 1 min. A large 8 × 8 mm silicon nanoimprint stamp with a square array of pillars, 210 nm diameter, 350 nm depth, 500 nm periodicity, coated with a hydrophobic SAM (heptadecafluoro-1,1,2,2-tetrahydrodecyl)trichlorosilane, Gelest Inc., PA) was then nanoimprinted into the thermal resist, at a pressure of 300 psi and baked at 130°C for 2 min (Nanoimprinter). The thermal resist acted as a mask to allow etching holes into the underlying silicon. The oxide layer was etched by a gas mixture of 25 sccm CF_4 and 50 sccm Ar at 150W for 4 min (STS etcher, "PJSOXIDE" recipe). The nanoimprint resist mask was then removed by soaking in acetone for 30 min, followed by oxygen plasma to clean the surface at 100 sccm O_2 at 100W for 5 min (STS etcher, "O2CLEAN" recipe). Using the thermal oxide nanohole mask, the silicon was etched in the deep trench etcher for 2 min (DRIE, "CNF-14mT" recipe), followed by an oxygen plasma cleaning for 15-30 min (STS etcher, "O2CLEAN" recipe). The silicon oxide mask was then removed using a wet chemical etch (buffered oxide etch, which is a 1:10 dilution of HF acid). This last step left the surface hydrophobic, so to make it hydrophilic to get it ready for template stripping, the chips were soaked in piranha solution, a 1:1 mixture of 96% sulfuric acid to 30% hydrogen peroxide (*CAUTION: this mixture is explosive, especially when organics are added to it*), for 10 min at 120°C, followed by extensive washing in deionized water and drying off with an N_2 gas.

Template Stripped Metal Film

The SPR sensor was then made by depositing metal on the silicon mold and transferring it to a glass slide, the surface of which was shown in Figure 13. First, silver was deposited on the silicon nanohole array molds using an electron beam metal evaporation. 100 nm silver was deposited at 0.1-0.2 Å/s for the first 10 nm, followed by 90 nm at 1 Å/s (Temescal or CHA evaporator). Glass slides that would be used to bond to and peel off

the metal were cleaned with acetone, methanol, and isopropyl alcohol to remove any dust particles, followed by deionized water cleaning and N_2 gas drying. Optical epoxy (NOA 61, Norland Products Inc.) was applied to the glass slide with two small droplets (2.7 µL each) followed by placement of glass slide on the metal surface and making sure there was barely enough epoxy to cover the metal. The mated pieces were placed glass side down and left overnight to let as much epoxy come out of the nanoholes as possible. The epoxy was then cured by UV light for 3 hours, and then inverted and cured under UV light for 3 more hours. The epoxy was then aged on a hotplate at 55°C for at least 6 hours. The template-stripping process was then carried out by using a razor blade to pop the silicon mold off, leaving behind the glass/epoxy/silver surface.[46,47] Right after the stripping process, a thin (15-25 nm), conformal film of silicon dioxide was added to the surface by alternate layer deposition,[48] a variation of atomic layer deposition (ALD machine, Cambridge Nanotech), thus capping the silver, preventing further oxidation.

Microfluidic Chip

A microfluidic chip was then made by soft lithography and bonded to the SPR sensor, the finished product was shown in Figure 12. First, a mold of the channel pattern was made with epoxy (SU-8) on silicon. A design was made in AutoCAD, sent to a company to produce a film mask (CAD/Arts Services). The film mask was transferred to a square chrome-on-glass mask by photolithography. Next, a silicon wafer was cleaned by piranha solution (sulfuric acid and hydrogen peroxide, 1:1; *CAUTION: this solution is explosive*) and diluted HF (buffered oxide etchant, 10:1), and SU-8 50 was spin-coated at 2000 RPM for 30 s to make a 50 µm thick film. Baking was done at 65°C for 6 min then 95°C for 20 min. The chrome hard mask pattern was transferred to the SU-8 and baked at 65°C for 1 min an 95°C for 5 min, and then put in developer for 10 min. The last step to make this mold was coating it with a SAM release layer (the same SAM used on the nanoimprint mold). Finally, polydimethylsiloxane (PDMS) (Sylgard 184, Dow Corning) was mixed (10:1 part A:B), degassed, and poured on the SU-8 mold and placed and heated on a hotplate overnight at 55°C. 25 × 25 mm squares of PDMS were cut and peeled off the

mold, and holes were punched for inlets and outlets. The punched PDMS was washed with isopropyl alcohol, methanol, and acetone, followed by DI water and nitrogen gas to dry them. They were then placed in O_2 plasma at 100 sccm, 75 Watts, 7 seconds (Asher) along with the glass slide with nanohole array, and then shortly afterward the PDMS chip was attached to the glass slide.

Solution Preparation

Solutions of phosphate buffered saline (PBS, 0.01 M, pH 7.2) were degassed for several hours in a vacuum chamber. Most of the solutions were then loaded into syringes for buffer only injections, while a small fraction was mixed with either concentrated myelin or antibody solutions to achieve desired concentrations of myelin (50 μg/mL) or antibodies (50 nM or 1 μM), and then loaded into syringes. A stock solution of bovine serum albumin (BSA, 5 wt % in PBS, pH 7.2) had been prepared and loaded into syringes previously to allow time to get rid of air bubbles. Solutions were kept at 4°C until needed in the experiment, and were allowed to warm up to room temperature for roughly 30 min before being used in the experiment.

Spectroscopic Kinetic Measurements

Microscope/Spectrometer

The assembled microfluidic chip was placed on an inverted microscope stage (Eclipse Ti-S, Nikon). A figure and schematic of this setup was shown in Figure 11. The optical train included a broadband light source, 2X (NA = 0.06) objective, an imaging spectrometer (MS257, Newport Corp.), and CCD camera (PIXIS 400B, Princeton Instruments). The imaging spectrometer and camera were controlled with custom LabVIEW (National Instruments) and analyzed with MATLAB (MathWorks) software.

Syringes with PBS were loaded into the syringe pumps (PHD2000, Harvard Apparatus) and connected to silicone tubing, which was connected to 4-way valves (IDEX, Upchurch Scientific). PBS was flushed through the valve to get rid of air bubbles, and the connected to the microfluidic chip, and gently flushed to get rid of air bubbles.

Kinetic Experiments

For the kinetic experiments, first 0.01 M PBS, pH 7.2, was injected in the channels for 30 min to establish a stable baseline. Then a solution of myelin particles (50 μg/mL), or PBS in the control channels, was injected for 1 hr, followed by washing of nonadsorbed particles with PBS for 1 hr. Next, the surface was blocked by 5% (w/v) BSA in PBS, followed by washing of nonadsorbed particles with PBS for 1 hr. Lastly, the antibodies were injected over the surface (association phase), followed by washing (dissociation phase). rHIgM22 was typically 50 or 100 nM concentrations. Kinetic experiments were performed at room temperature (~25°C).

Kinetic Data Processing and Analysis

Spectral images of the channels were recorded by the CCD camera, as was shown in Figure 14. The vertical axis of the images corresponds to a line from the chip (across the channels) projected into the entrance slit of the spectrometer. The horizontal axis of the images corresponds to that entering light spread into its component wavelengths by the grating inside the spectrometer. In this manner, spectra from 8 microfluidic channels could be collected simultaneously. Using MATLAB (MathWorks), the pixels in the images corresponding to each channel were selected to obtain a spectrum for each channel. To smooth the spectra, a 5th order polynomial was fit to a dip near 700 nm, and a minimum was calculated. A dip was chosen instead of a peak because it was more stable due to the light source intensity fluctuated a bit, probably because it did not have a power stabilizing feedback control. Plotting the position of the dip vs. time gave association and dissociation curves.

Nonlinear least squares curve fitting could then be performed as previously reported.[70,71] First, using Origin (OriginLab Corp), a double exponential decay was fit to the dissociation data to find $k_{d,\,fast}$ and $k_{d,\,slow}$,

$$R = R_a e^{-k_{d,fast}t} + R_b e^{-k_{d,slow}t}$$

followed by curve fitting to the association data using these dissociation rate constants and the analyte concentration to find k_a,

$$R = \frac{Ck_aR_{max}\left[1 - e^{-\left((Ck_a + k_d)t\right)}\right]}{Ck_a + k_d}$$

Finally, the apparent equilibrium constant, $K_{D,\ apparent}$, was calculated by $k_{d,\ slow}$ / k_a. Data with obvious drift in signal or other obvious artifacts were excluded from the analysis.

3.4 Results

SPR Binding Experiments

Figure 19 shows typical SPR binding experiments between IgMs and myelin particles. The plots show the change in the surface plasmon resonance wavelength over time as various solutions are injected over the sensor surface. Panels A1 (which includes both the preparation and the kinetics steps) and A2 (which includes just the kinetics step) show mouse IgM O4 (50 nM) injected over myelin particles (red/darker trace), and a control channel with no myelin particles (gray/lighter trace). Similarly, panels B1 and B2 show rHIgM22 (50 nM) injected over myelin (blue/darker trace) and non-myelin (gray/lighter trace) surfaces. The myelin particles were extracted myelin membrane extruded through 50 nm diameter pores. The resonant wavelength shift due to incubation with myelin particles is ~3.5 nm. Any exposed surface was then blocked with BSA (5 wt %), to block nonspecific binding of antibodies in the final step of the experiment, the kinetics step. The high concentration of BSA used to maximize blocking causes a large resonance shift due to a large refractive index difference of the solution vs. PBS-only solution (what is known as the "bulk shift"). The resonance quickly returns back after washing after the higher refractive index BSA solution is replaced with PBS. In the channels with adsorbed myelin (darker traces), there was very little net shift after BSA injection, indicating good coverage of adsorbed myelin and little exposed surface needing to be blocked with BSA. In the channels without myelin particles (lighter traces), there was a significant net shift after BSA blocking (~1.5 nm), indicating a large amount of BSA adsorbed and remained on the

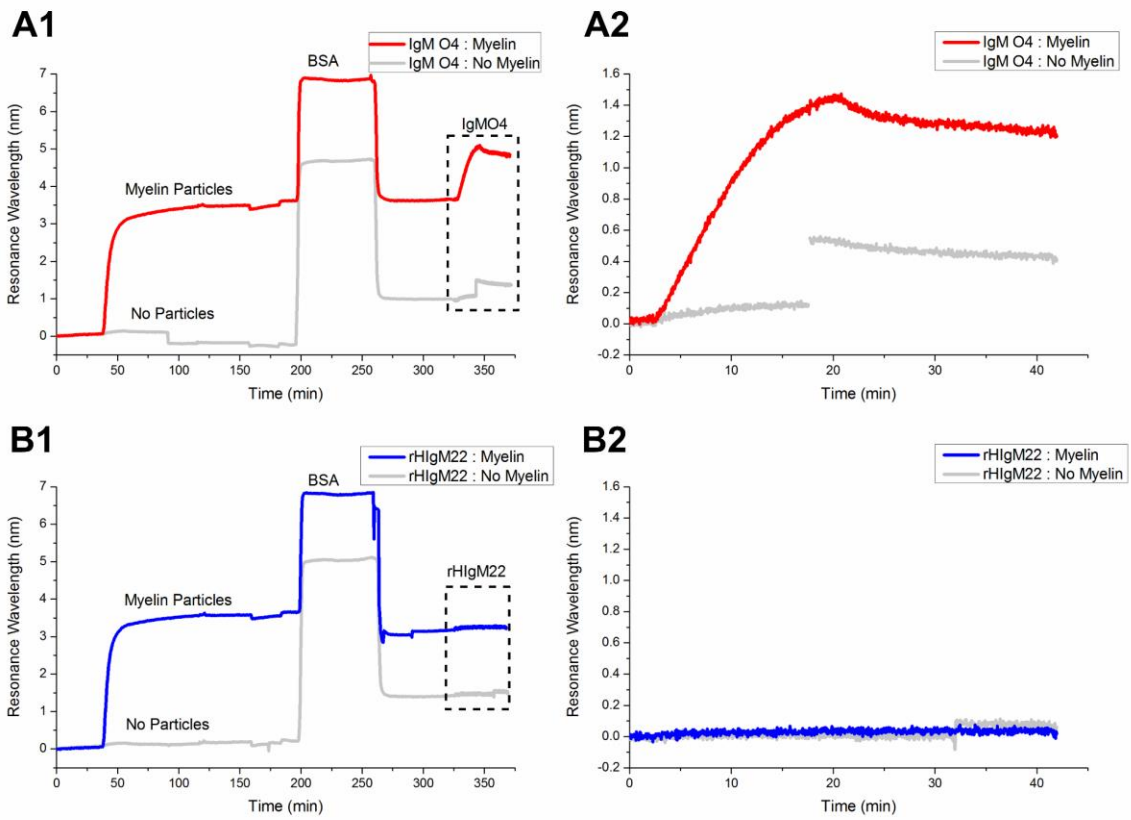

Figure 19: Typical SPR binding curves between IgM O4 or rHIgM22 and extruded myelin particles. Sensorgrams from four microfluidic channels. Panels on the left show the entire course of the experiment, which includes the preparation steps and the final binding kinetics step (**dashed boxes**). Panels on the right show the binding kinetics step enlarged and offset. (**A1-A2**) Channels with IgM O4 and myelin (**red/darker trace**) or no myelin (**gray/lighter trace**). (**B1-B2**) Channels with rHIgM22 and myelin (**blue/darker trace**) or no myelin (**gray/lighter trace**). Panel **A2** shows IgM O4 bound to myelin but not the non-myelin surface, as expected. Panel **B2** shows the surprising non-binding between rHIgM22 to myelin, a problem that persisted in our subsequent experiments.

surface due to the lack of myelin on the surface. In the final step, the kinetics step of the experiment, antibodies were injected over the myelin or non-myelin surfaces. The large shift of the red/darker trace in A2 indicates that IgM O4 bound to myelin. A much smaller shift of the gray/lighter trace in A2 shows that very little IgM O4 bound to the BSA-only surface. Conversely and surprisingly, almost non-existent shifts of either trace in panel B2 indicate that rHIgM22 did not bind to myelin (blue/darker trace) or the BSA-only surface

(gray/lighter trace). This lack of binding between rHIgM22 and myelin was a consistent result throughout all of our subsequent SPR experiments.

Some small jumps appear in the data and these are likely due to small air bubbles passing through the microfluidic channels. In some experiments, such as those which use lipid bilayers, air bubbles will disrupt the lipid bilayers and ruin the experiment. In these experiments, sporadic air bubbles often did not significantly alter the amount of material on the surface as seen by the return close to the previous SPR resonance level. And based on separate experiments (by our collaborators at the Mayo Clinic, data not shown) in which the myelin was actually dried out before rHIgM22 was incubated over it, which resulted in binding, indicates that air bubbles likely would not disrupt receptors in the myelin.

Nonetheless, over time we implemented additional measures to get rid of the air bubbles in microfluidic channels with great success. One helpful procedure was to initially inject isopropyl alcohol to lower surface tension and wet all the connections, preventing air bubbles from getting trapped and coming loose later. This procedure reduced air in the four-way valves and the connections on the chip. Another helpful procedure was to degas all solutions in the vacuum pump for several hours, followed by very slow drawing up of the solutions with the syringes, and careful inspection of the syringe and needle hubs to make sure air did not get trapped anywhere. An additional helpful procedure was to prepare the BSA solution several days before the experiments, because mixing and withdrawing this solution into syringes can form bubbles which are stable for many hours. The last helpful measure was to alter the procedure for switching syringes during the experiment, by priming the new syringe to form a bead at the tip of the needle, lowering the silicone tubing so liquid beaded at its end (due to gravity), and then connecting them, so as not to introduce any air bubbles. These measures greatly helped eliminate bubbles during experiments.

The main goal for these binding experiments was to determine binding kinetics between rHIgM22 and myelin, but our first experiments showed no detectable binding. To determine the cause of this lack of binding, several factors were then tested. These factors included: new antibody, higher antibody concentration, larger extrusion pores, new

Table 1 Myelin Binding Experiment Conditions Tested and Results

Condition Tested	IgM O4 to myelin	rHIgM22 to myelin
new rHIgM22	specific binding	*very little binding*
higher concentration rHIgM22 (20× higher)	specific binding	*no binding*
larger pores during extrusion (200 vs. 50 nm diameter)	specific binding	*nonspecific binding*
new myelin	specific binding, nonspecific binding	*no binding*
unextruded myelin and oligodendrocyte membrane	specific binding, nonspecific binding	*no binding*

myelin, and unextruded myelin and oligodendrocyte membranes. Table 1 summarizes these kinetic experiments, and the following figures show the SPR sensorgrams from the experiments. Table 1 indicates that in all the conditions tested, binding between mouse IgM O4 and myelin occurred, and binding between rHIgM22 and myelin was either nonexistent, close to nonexistent, or had less specific binding than nonspecific binding.

One possible source of the lack of binding could have been degradation of rHIgM22. Proteins in solution can degrade over time or get contaminated. One simple way to test this would be to try a newer stock of the protein. So we obtained a newer stock of rHIgM22 from our Mayo Clinic collaborators. The results from this experiment are shown in Figure 20. Figure 20 is presented in the same manner as Figure 19, the only difference is the experimental use of a new stock of rHIgM22 (blue/darker traces in B1-B2). As can be seen in panel B2, there is very little to no binding of rHIgM22 to myelin (blue/darker trace).

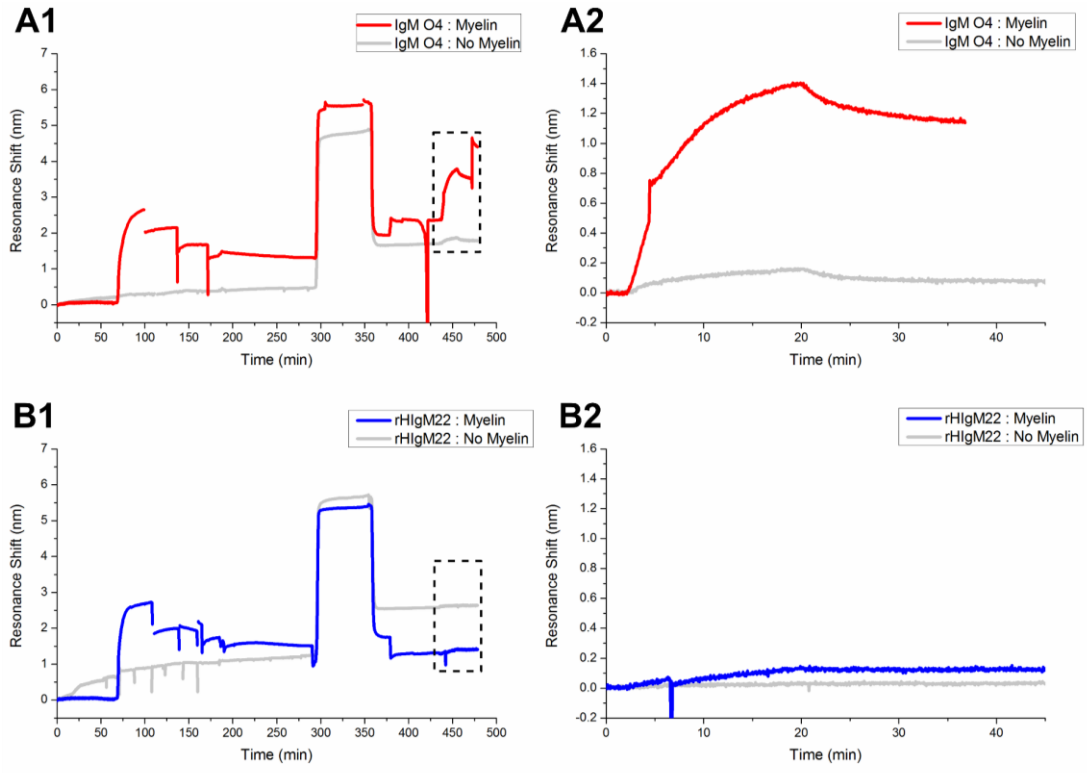

Figure 20: Troubleshooting non-binding of rHIgM22 to myelin: testing new rHIgM22. SPR curves from antibodies injected over myelin particles, using a new stock of rHIgM22 to test if the previous antibodies had gone bad. Panel **B2** shows that rHIgM22 did not bind to myelin (**blue/darker trace**), indicating the antibody stock was not the problem.

Another possible source of apparent non-binding might be a smaller amount of binding between rHIgM22 and myelin vs. IgM O4 and myelin. There may be fewer receptors in myelin membrane or a weaker affinity for rHIgM22 and myelin than IgM O4 and myelin. A way to increase the amount of bound antibody could be to increase the concentration of rHIgM22, so we increased the concentration 20-fold, from 50 nM up to 1 µM. The results from this experiment are shown in Figure 21. Figure 21 is presented in the same manner as Figure 19, the only difference is the experimental addition of a higher concentration of rHIgM22 (panels C1-C2). Panel C2 shows that the higher concentration of rHIgM22 does not lead to detectable binding to myelin. There is a slight shift in the resonant wavelength,

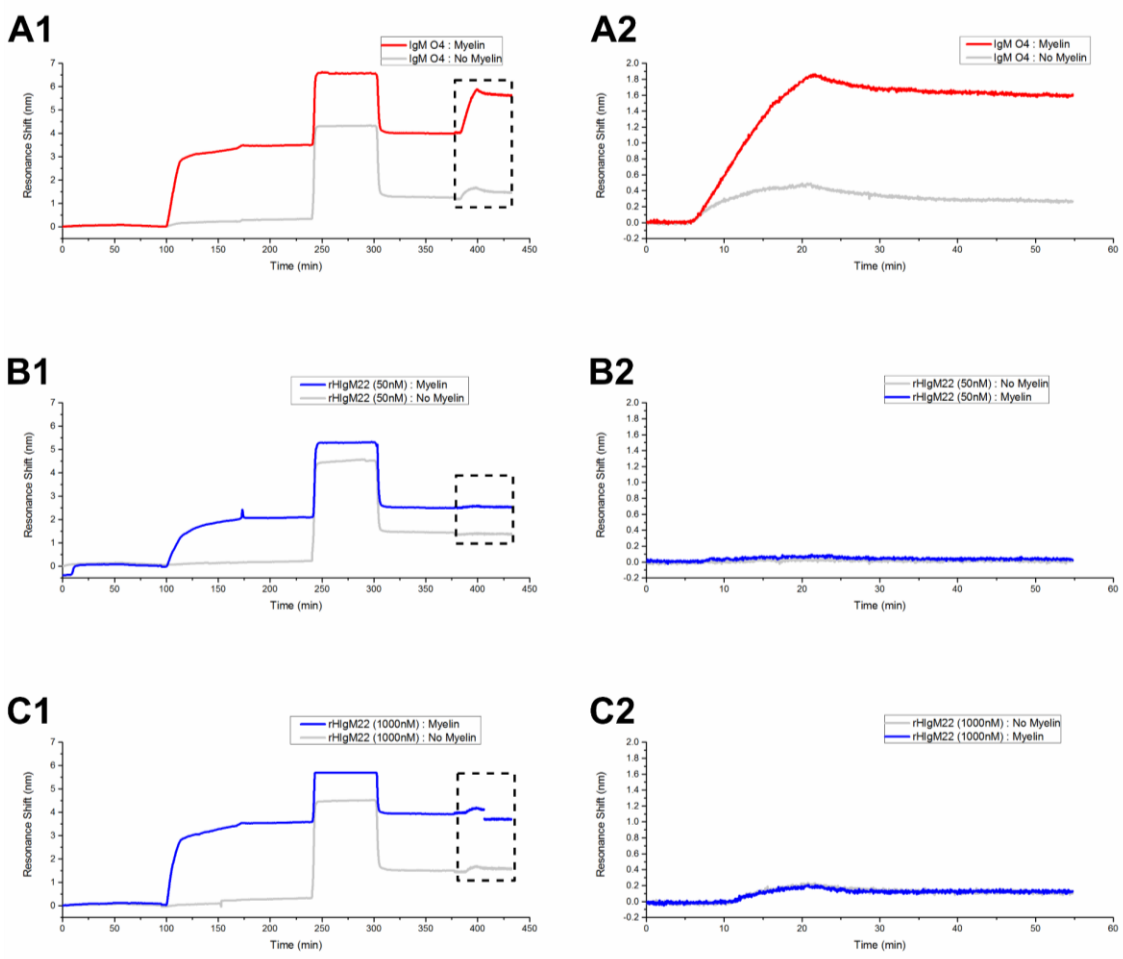

Figure 21: Troubleshooting non-binding of rHIgM22 to myelin: testing a higher concentration of rHIgM22. SPR curves from antibodies injected over myelin particles, using a 20× higher concentration of rHIgM22 (1 μM instead of 50 nM). Panel **C2** shows that even with the higher concentration of antibody, no significant difference in specific and nonspecific binding between rHIgM22 and myelin was detected (**blue/darker trace**).

but it is the same in both the channel with myelin (blue/darker trace) and channel without (gray/lighter trace), revealing that it is due to nonspecific binding.

Another possible cause of lack of binding between rHIgM22 and myelin could be that the extrusion process was filtering out the receptors in myelin. The extrusion process required high pressure to push the myelin through the 50 nm filter, increasingly with each pass. This likely indicates some membrane was getting stuck in pores. The receptor could

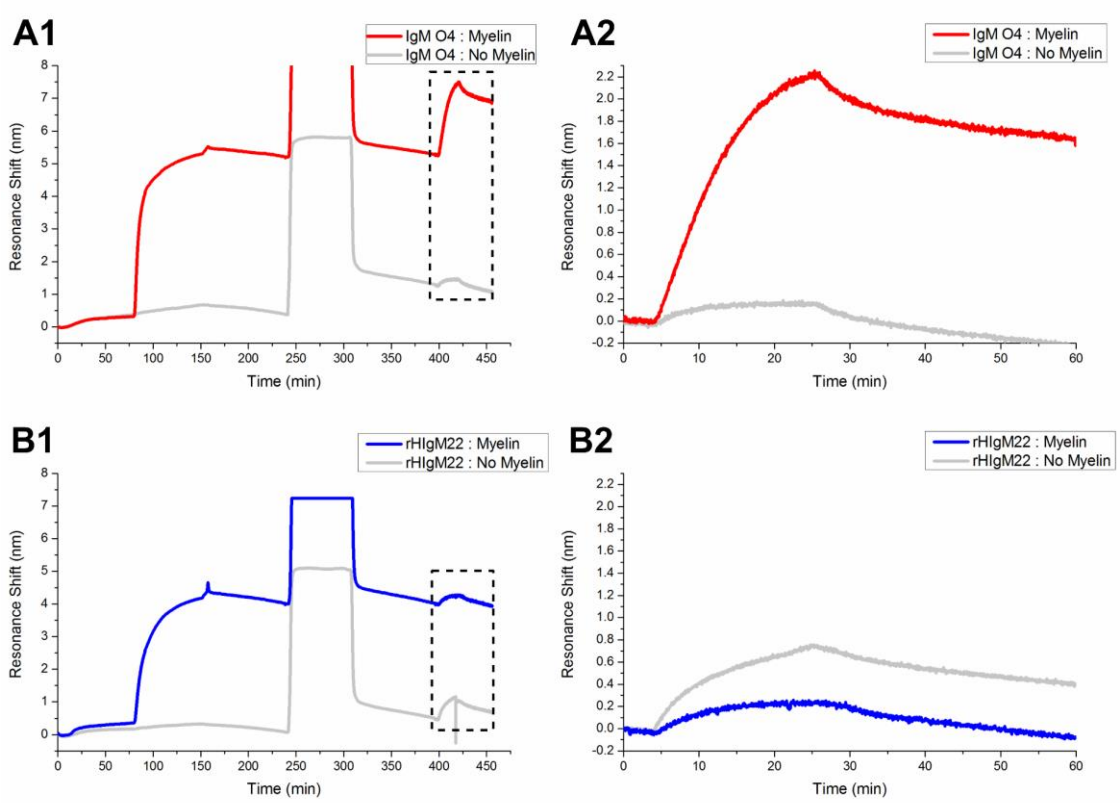

Figure 22: Troubleshooting non-binding of rHIgM22 to myelin: testing extrusion through larger pores. SPR curves from antibodies injected over myelin particles of a larger size due to extrusion through a filter with larger pores (200 nm vs. 50 nm diameters), to prevent possible receptor loss in the extrusion filter. Panel **B2** shows some resonance shift between rHIgM22 and myelin (**blue/darker trace**), but it is likely nonspecific binding, as there is a similar shift for IgM O4 to non-myelin (**A2, gray/lighter trace**) and even greater shift for rHIgM22 to non-myelin (**B2, gray/lighter trace**).

be getting preferentially stuck in the filter. So to allow more membrane to pass through the pores, we tried extruding through a larger pore size (200 vs. 50 nm diameters). The pressure needed to carry out the extrusion was noticeably less. The results from the subsequent SPR binding experiment are shown in Figure 22. Figure 22 is presented in the same manner as Figure 19, the only difference is the experimental change of size of myelin particles used (darker traces). Myelin particles were extruded through 200 nm pores instead of 50 nm pores prior to adsorption on the surface to prevent possible removal of receptor by the extrusion filter. The results in this experiment were imperfect, but they

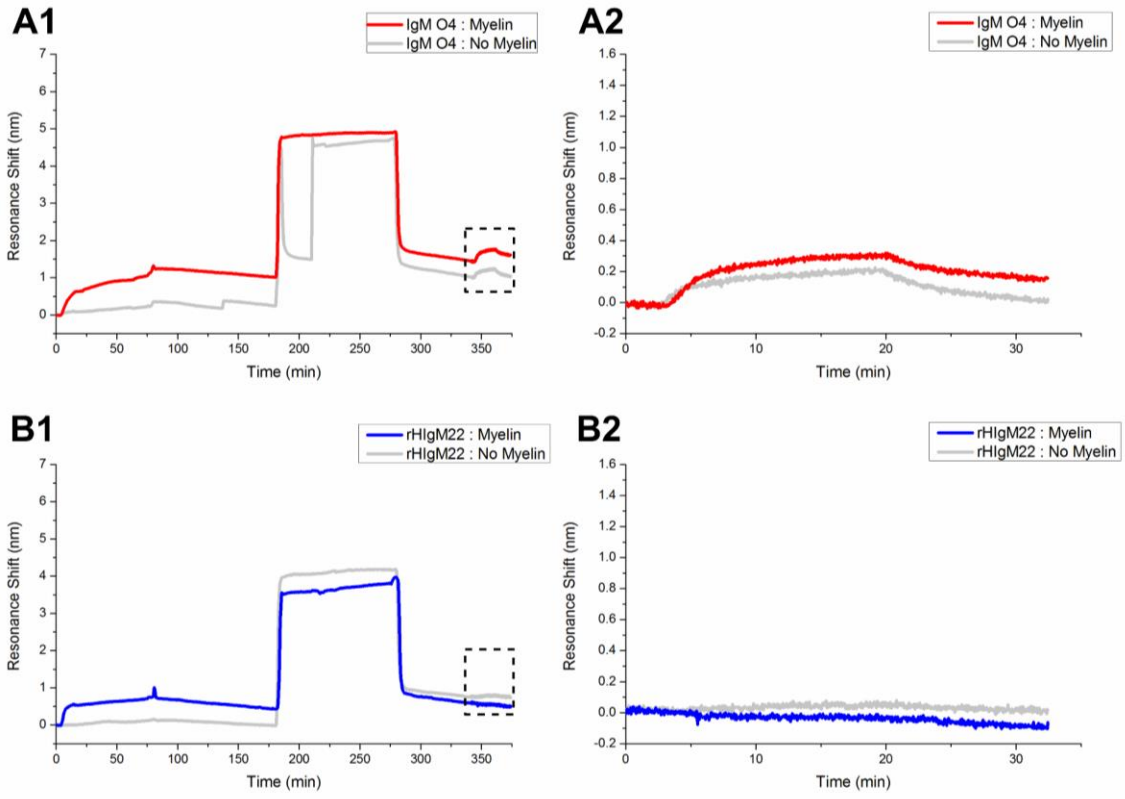

Figure 23: Troubleshooting non-binding of rHIgM22 to myelin: testing new myelin. SPR curves from antibodies injected over myelin particles, using a newer stock of extracted myelin membrane. Panel **B2** shows that once again, no binding is detected between rHIgM22 and myelin (**blue/darker trace**).

likely indicate that rHIgM22 did not bind to myelin. There was a small resonance shift for rHIgM22 to myelin (blue/darker trace in B2), which could indicate binding. However, this is likely nonspecific binding, as there was a similar resonance shift in the IgM O4 to non-myelin surface (gray/lighter trace in A2), and even greater shift in the rHIgM22 to non-myelin surface (gray/lighter trace in B2).

Another possible cause of lack of binding between rHIgM22 and myelin might be degradation of the receptors in the myelin. So we obtained a newer stock of extracted myelin membrane from our Mayo Clinic collaborators. The results from this experiment are shown in Figure 23. Figure 23 is presented in the same manner as Figure 19, the only

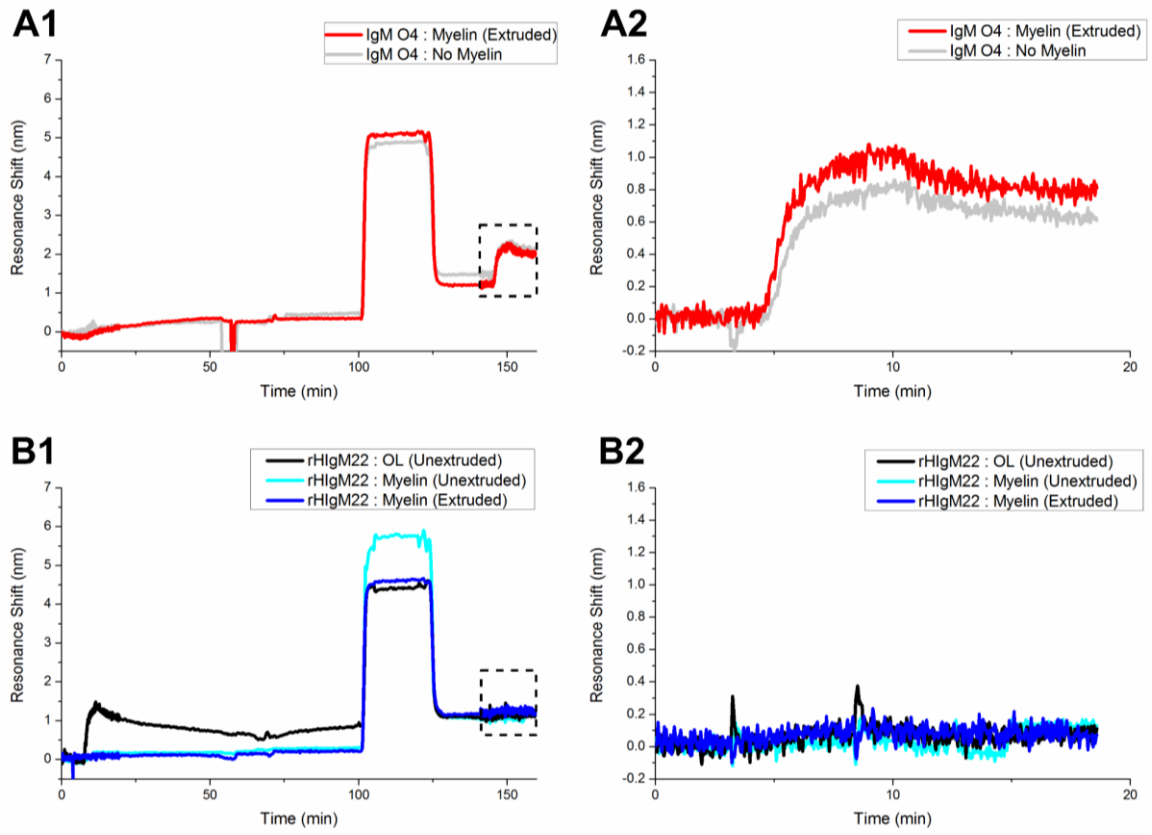

Figure 24: Troubleshooting non-binding of rHIgM22 to myelin: testing unextruded myelin. SPR curves from antibodies injected over extruded myelin, unextruded myelin, and unextruded membrane from cultured oligodendrocytes, which should also include the receptor for rHIgM22. Panel **B2** shows that, once again, no binding was detected between rHIgM22 and extruded myelin (**blue trace**), unextruded myelin (**cyan/lighter trace**), or unextruded oligodendrocyte membrane (**black trace**).

difference is the experimental change of using a newer stock of myelin (darker traces). Once again rHIgM22 did not bind to myelin (blue/darker trace in B2).

The last factor we tested was whether the receptor in the myelin might be reacting with polycarbonate filter we were using for extrusion. Proteins and lipids can react with surfaces differently, depending on hydrophobicity or electrostatic properties of the biomolecules and the surface materials. So to rule out the material of the extrusion filter as the problem, we tested binding of rHIgM22 to unextruded myelin. As a parallel test, we also included a channel with membrane from cultured oligodendrocytes (instead of extracted myelin

from mice), which should also include the receptor, but in different amounts. These results from this experiment are shown in Figure 24. Figure 24 is presented in the same manner as Figure 19, the only difference is the experimental change of including unextruded myelin (cyan/lighter trace) and oligodendrocyte membrane (black trace) in panels B1-B2. No binding is detected between rHIgM22 and extruded myelin, unextruded myelin membrane, or unextruded oligodendrocyte membrane. It is possible that binding of rHIgM22 occurred, but occurred outside of the sensing region of the sensor, since these particles were of micrometer dimensions. It is also possible that not many particles immobilized over the sensor surface that we were monitoring from, a region of roughly ~100 × 100 μm. The resonance shifts of the immobilized particles were not very large, most of them less than 1 nm (darker traces in panels A1 and B1). For this reason, this experiment could stand to be repeated, although there was a shift from oligodendrocyte membrane getting immobilized (black track in A1), but no detected binding to it (black trace in B2). This membrane should also include the receptor for rHIgM22, so it may be representative of the myelin membrane.

Sandwich Assay to Verify Binding

In these SPR experiments we could detect binding between IgM O4 and myelin particles, but not between rHIgM22 and myelin particles. So we decided to try an alternative method to SPR, immunohistochemistry, similar to what our collaborators at the Mayo Clinic used, to verify whether or not we could detect binding between rHIgM22 and myelin in our lab, even though it would not give us the kinetic information we were after.

The immunohistochemistry experiment was similar to common enzyme-linked immunoassay (ELISA) experiments. First, myelin particles, extruded and unextruded, were added to wells of a 96-microwell plate, and were incubated overnight and allowed to dry out. The next day the wells were washed and blocked with BSA. The wells were then incubated with rHIgM22, followed by washing. Finally, the wells were incubated with a fluorescent secondary antibody, followed by washing. Alternatively, to verify that membrane remained in wells, some wells were not incubated with antibodies, but instead

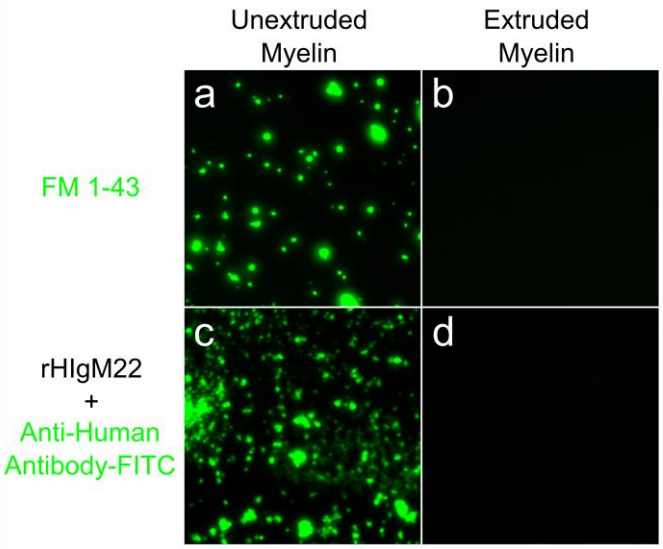

Figure 25: Immunohistochemistry experiment to detect binding between rHIgM22 and myelin. Fluorescence micrographs from an immunohistochemistry experiment, performed as an alternative method to SPR, to determine if binding existed between rHIgM22 and extruded and unextruded myelin, and if membrane existed after the extrusion process. Unextruded (**a, c**) and extruded (**b, d**) myelin particles were incubated in wells of a microwell plate. The wells were then washed and either incubated with the lipophilic dye FM 1-43 (**a, b**) which fluorescently labels lipid bilayers, or with rHIgM22 followed by a fluorescent secondary anti-human IgM antibody (**c, d**). Fluorescence from FM 1-43 shows that unextruded membrane is present (**a**), but extruded myelin may not be present (**b**). Fluorescence from antibody binding show rHIgM22 bound to unextruded myelin (**c**), but not detectably to extruded myelin (**d**).

with FM 1-43, a fluorescent dye that partitions into lipid bilayers. The results from the immunohistochemistry experiment are shown in Figure 25.

The immunohistochemistry experiment, shown in Figure 25, reveals that the extrusion process could be removing much of the membrane, as evidenced by FM 1-43 staining, which detected unextruded membrane (fluorescence in panel a), but not extruded membrane (lack of fluorescence in panel b). We expected some fluorescence to extruded membrane that should be there, that we detected in the preparation steps of the SPR experiments by a resonance shift when particles are injected. Also, in those experiments, IgM O4 specifically binds to myelin particles. It is possible the fluorescence signal in this

immunohistochemistry experiment is too faint to be detected. Ideally this experiment would be performed with an amplification step.

A second finding from the immunohistochemistry experiment is that rHIgM22, as in the SPR experiments, did not detectably bind to extruded membrane (lack of fluorescence in panel d), but surprisingly, finally bound to myelin, in unextruded form (fluorescence in panel c). Some detectable binding reveals that the receptors and antibodies are still functional. The lack of detection of binding to extruded membrane may indicate extrusion is knocking out the receptor, or the fluorescence signal is once again too weak for detection. This assay should be repeated with enzyme linked antibodies.

To summarize the immunohistochemistry experiment analysis, the findings may not be entirely conclusive because of limitations of the detection limit, but they suggest that extrusion may be knocking out the receptors, and that rHIgM22 and the receptors in unextruded myelin are still functional.

Calculation of Kinetic Constants of Mouse IgM O4 to Myelin Particles

Our primary goal was to measure binding between rHIgM22 and myelin, but we never were able to detect this binding with SPR experiments. After testing many conditions to elucidate the source knocking out binding, our collaborators at the Mayo Clinic found potential antigens to a second therapeutic antibody, rHIgM12, which were more feasible to test by SPR. So we moved our focus to testing binding kinetics between that antibody and its proposed antigens, which is presented in chapter 4. We chose to put testing of rHIgM22 and myelin on hold, and were unable to revisit it.

However, we could still accomplish a secondary aim: evaluate if the extruded membrane could be used to obtain kinetic constants by analyzing the binding data between mouse IgM O4 and myelin particles. Figure 26 shows the data and results of this analysis. Figure 26 shows binding data between mouse IgM O4 (50 nM) and extruded (50 nm diameter) myelin particles (red/darker data circles), and non-myelin surfaces (gray/lighter data circles). A biphasic exponential decay curve (decaying black trace) was fit to the dissociation data by the least squares fitting method, as an approximation of the

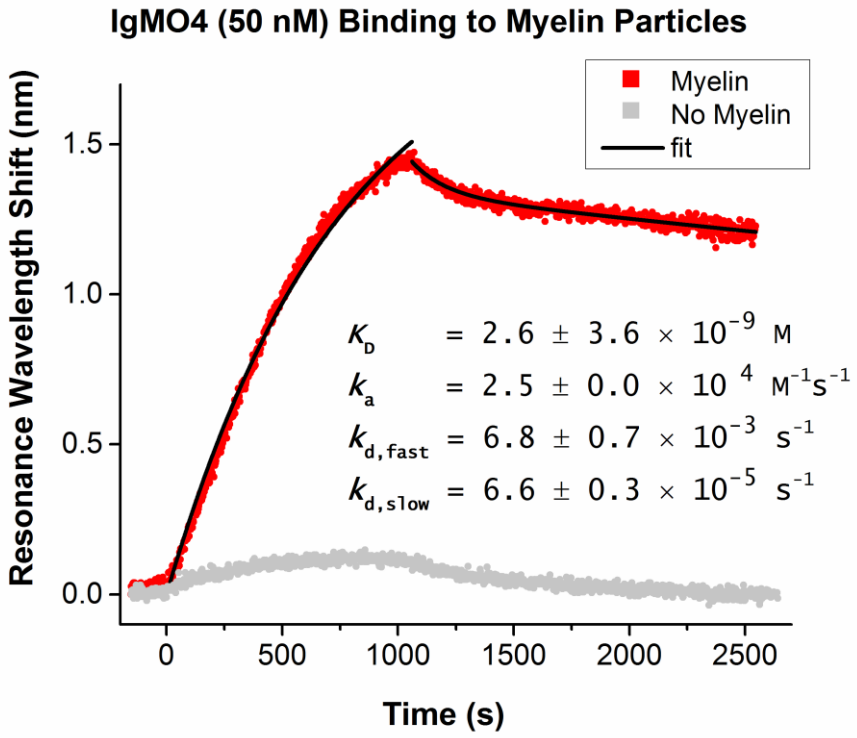

Figure 26: Kinetic binding curves of mouse IgM O4 to surfaces incubated with and without myelin particles. Curves (**black lines**) were analytically fit to the data (**red/darker circles**) to obtain kinetic constants. The large shift in the myelin channel indicates specific binding between IgM O4 and myelin (**red/darker circles**), and very little nonspecific binding in channels without myelin (**gray/lighter circles**).

multivalency of the IgMs, to give $k_{d,\,fast}$ = 6.8 ± 0.7 × 10^{-3} s^{-1} and $k_{d,\,slow}$ = 6.6 ± 0.3 × 10^{-5} s^{-1}. The slow k_d was then used to fit a monophasic exponential curve (rising black trace) to the association data, giving k_a = 2.5 ± 0.0 × 10^4 $M^{-1}s^{-1}$. Only the slow k_d was used because it would have a greater effect on the reaction rate. The ratio of $k_{d,\,slow}$ over k_a gives the apparent equilibrium dissociation constant, $K_{D,apparent}$ = 2.6 ± 3.6 × 10^{-9} M.

3.5 Discussion

Mouse IgM O4 binding to extruded myelin particles is detectable by SPR

The primary goal of this study was to determine binding kinetics between rHIgM22 and an unknown receptor in myelin. SPR sensing was the method chosen to obtain this information because it can obtain kinetic constants and does not require adding a fluorescence or radioisotope tag, which can alter binding behavior. The first challenge was deciding what molecule to immobilize on the sensor, because we had not yet identified the receptor or receptor complex in myelin. We only knew that the antibody bound to myelin and oligodendrocyte membrane. So instead of choosing an individual receptor, we chose to immobilize extracts of animal membrane, which would include the unknown receptors. A technical challenge with this approach is that the extracted myelin formed micrometer-scale clumps, whereas the sensing window for SPR is only a few hundred nanometers, so the majority of the antibody binding events would likely be outside this window and would go undetected.

Therefore, to further reduce the size of myelin membrane clumps, we chose to extrude myelin membrane through track-etched pores of known diameters, a method commonly used for producing lipid vesicles of known sizes. In most of the experiments we extruded the myelin through pores with 50 nm diameters; in one experiment through pores with 200 nm diameters. We then injected the myelin particles over the SiO_2 surface, resulting in >1 nm resonance wavelength shifts in all experiments (except for the unextruded myelin test), which did not shift back during an hour long washing with PBS solution, evidence that the particles had passively adsorbed to the surface. After myelin immobilization, any vacancies on the surface were blocked by an injection of a high concentration of BSA, followed by a washing step. In channels with myelin, usually some BSA remained on the surface after washing, indicating some gaps that needed to be blocked, but the resonance shifts were less than the myelin immobilization step. In channels without myelin (the negative controls), a much larger amount of BSA adsorbed, due to the entire surface needing to be coated with BSA.

Table 2 Mouse IgM O4 Binding Constants to Myelin and Sulfatide in SLB

Antibody	Antigen	K_D ($\times 10^{-9}$ M)	k_a ($\times 10^4$ $M^{-1}s^{-1}$)	$k_{d,\ slow}$ ($\times 10^{-5}$ s^{-1})	$k_{d,\ fast}$ ($\times 10^{-3}$ s^{-1})	Ref
IgM O4	extruded myelin particles	2.6 ± 3.6	2.5 ± 0.0	6.6 ± 0.3	6.8 ± 0.7	this study
IgM O4	2% Sulf in SLB	2.2 ± 0.6	26.5 ± 17.1	37.3 ± 11.5	Unlisted	[69]

We then injected either rHIgM22 or mouse IgM O4 (as a positive control for myelin) over the surfaces. We had partial success with binding to the myelin particles: IgM O4 bound specifically, but rHIgM22 never bound at a detectable level. We analytically fit curves to the data and calculated the kinetic and equilibrium constants. The calculated equilibrium dissociation constant and kinetic rate constants were nearly identical to previous measurements and calculations, as shown in Table 2. Included in this table are results from a study by Wittenberg et al. which obtained kinetic constants of IgM O4 to purified sulfated galactocerebroside (Sulf) in a supported lipid bilayer (SLB).[69] The dissociation equilibrium constant is nearly identical between this particle-based study and that SLB-based study (K_D = 2.6 nM vs 2.2 nM), but the kinetic rate constants vary by up to an order of magnitude ($k_a = 2.5 \times 10^4$ vs. 2.7×10^5 $M^{-1}s^{-1}$, and $k_d = 6.6 \times 10^{-5}$ vs. 3.7×10^{-4} s^{-1}).

There is a difference in kinetic rate constants between the two preparations (extruded myelin particles vs. receptors embedded in SLBs) by roughly ten-fold (association) and five-fold (dissociation). One potential cause of this difference in rates may be the inclusion of other proteins and lipids in the animal membrane preparation, which may present the sulfatide receptor differently than the simpler receptor-doped SLB membrane. The SLB preparation used a base mixture of phosphatidyl choline lipids from chicken eggs mixed with 2% of the receptor, sulfatide. In the extruded membrane preparation, it is possible that all of the original molecules from the membrane are present. In addition to

phosphatidyl choline lipids, this mixture would include cholesterol (a major constituent in myelin), proteins (which make up ~30% of myelin) such as myelin basic protein (MBP), myelin associated glycoprotein (MAG), myelin oligodendrocyte glycoprotein (MOG), and proteolipid protein (PLP), and other lipids such as phosphatidyl ethanolamines, glycerols, serines, inositols, and other sphingolipids. Cholesterol and sphingolipids have been demonstrated to form lipid rafts, which can alter sphingolipid orientation and diffusion rate. It is likely that sulfatide, a sphingolipid, would partition into a lipid raft, and thus may present sulfatide differently than in a supported lipid bilayer without cholesterol or other sphingolipids, which can lead to different binding properties. In some cases, this clustering of sphingolipids can alter binding strength by multivalent binders like the decavalent IgMs. Shi et al. showed as the percentage of glycosphingolipid, GM1, in a supported lipid bilayer increases from 0.2 to 10%, the binding affinity to it by pentavalent cholera toxin can change by almost ten-fold.[72]

Steric hindrance by larger molecules may also reduce binding interactions to smaller molecules in membranes. Sulfatide is a small molecule consisting of a lipid with a sulfated galactose sugar as its headgroup. Larger lipids and proteins, such as glycosylated molecules, could block binding to these smaller molecules, lowering the association rate.

Also, some proteins and peptides bind more strongly to more highly curved membranes. For example, one study found the neural protein alpha-synuclein bound more strongly to vesicles with decreasing diameters (~45 nm was the strongest, ~180 nm was the weakest).[73] It is possible that IgM O4 binds more strongly to more positively curved membranes, such as the extruded particles compared to the planar SLB, contributing to its lower dissociation rate.

Unable to determine why rHIgM22 did not bind to myelin particles

We tested several conditions to determine why rHIgM22 did not bind to extruded myelin particles. These conditions included, a new stock of antibodies (to check for protein degradation), a very high concentration of antibody (to increase amount of binding and give a larger signal), larger myelin particles (in case receptor was getting removed with the

smallest filter pore size), new myelin extracts (to check if receptor had deteriorated), and unextruded myelin and oligodendrocyte membrane (to evaluate filter effects). No single tested factor resulted in detectable binding of rHIgM22 to myelin. Perhaps the cause is multifaceted and combinations of these tested factors may be responsible. Or possibly the tests run were not extensive enough. Some of the tests could be modified, such as an immunohistochemistry experiment using amplifying molecules like an enzyme-linked antibody. Some of the tests could be rerun, such as the unextruded membrane test, which was not entirely clear if enough membrane entered the sensing area of the chip. And it is possible that a better blocking agent rather than BSA could remove more of the nonspecific binding by the antibodies. Some of these factors and potential improvements will now be discussed in greater detail.

Pore sizes may be too small

The possibility of the extrusion filter removing rHIgM22 receptors in myelin due to restrictively small pore diameters was tested by increasing extrusion pore diameters, extruding with 200 nm pores instead of 50 nm pores. The pressure from the syringes during extrusion with 50 nm pores was fairly high, and the process had to be stopped after several passes, reducing the number of passes through the filter from the recommended (for lipid vesicles) 11 passes down to 7 passes. Upon switching to the 200 nm filters, the pressure decreased greatly, meaning less membrane was getting caught in it. However, binding between rHIgM22 and myelin still was not detected. It is possible myelin and its receptors may still have been getting caught in the extrusion filter. So it may be helpful to extrude with larger pores, such as 400, 800, or 1000 nm diameter pores to reduce this potential clogging. Additionally, it may help to pass the particles through multiple filters, first through larger pores and then smaller pores, to gradually reduce particle sizes.

Receptor may be interacting with polycarbonate filter

Another factor which may be causing the binding knockout between rHIgM22 and extruded myelin could be the extrusion filter material. The unknown receptor could be

getting adsorbed and denatured on the polycarbonate extrusion membrane. Biomolecules vary on how strongly they adsorb to different materials. Proteins can form electrostatic bonds, hydrogen bonds, and hydrophobic interactions with surfaces, to varying levels depending on the protein structure, surface properties, and solution conditions. After proteins adsorb to a surface, they can change shape and lose function or binding properties.[74,75] One study tested adsorption and shape change of the protein human serum albumin (HSA) on polycarbonate membranes (contact angle: 47°) and polycarbonate membranes modified with the polymer, poly(N-vinylpyrrolidone) (PVP) to be more hydrophilic (contact angle: 20°). They found the protein adsorbs to both membranes, but binds more quickly and immediately changes shape on the more hydrophobic polycarbonate membrane.[76] It may be possible that the unknown receptor of rHIgM22 is a protein that gets denatured on the polycarbonate surface of the extrusion filter.

Another material interaction could be occurring with the lipids of myelin. Lipids in aqueous solutions adsorb differently on different surfaces. On hydrophobic surfaces, lipids adsorb with the tail groups contacting the surface. Conversely, on hydrophilic surfaces, lipid headgroups face the surface (with their tail groups facing other lipid tail groups, forming micelles, vesicles, or planar bilayers).[77] It is possible that extrusion through polycarbonate membrane strips lipids from the myelin which may be the receptor or part of the receptor complex for rHIgM22. This scenario may be less likely since the lipid receptor for IgM O4, sulfatide, was still present in the extruded membrane, and these polycarbonate membranes are the only membranes routinely sold for lipid vesicle preparations, with no stated adverse effects.

The effect of extrusion filter material on binding between rHIgM22 and myelin could be tested by extruding myelin with filters of different materials and measuring binding capability before and after extrusion. It may be beneficial to use an enzyme linked immunosorbent assay (ELISA) for this test, since it is a little simpler and higher throughput than the SPR experiments, as many conditions with many replicates can be tested at once. The ELISA is similar to the immunohistochemistry experiment run in this project but with better amplification of low signal. The different materials tested could include a

commercially available filter such as Millipore's low-protein binding polyethersulfone or hydrophilic polytetrafluoroethylene (PTFE) filters (www.emdmillipore.com), or by modifying a polycarbonate filter with PVP as done by Henry et al., 2003.[76] One potential downside to this approach is that it is not clear if other filter types, which are not track-etched, would reduce particle sizes in a similar manner to track-etched membranes.

An alternative approach to the extrusion method could be to create giant plasma membrane vesicles (GPMV) of myelin by chemically blebbing oligodendrocytes, and then rupturing the GPMVs on the sensor surface. Chemical blebbing creates giant plasma vesicles simply by adding chemicals to the medium cells are in, inducing the cell membrane to bud and pinch off from the cells.[78] It is important to planarize these membranes because they will be much larger than the SPR sensing region, having diameters much greater than 1 μm in diameter. It is possible that once GPMVs are applied to the chip they may rupture on the hydrophilic SiO_2 surface, similar to many lipid vesicle types. However, the cell-derived GPMVs might not rupture, as they might have a high concentration of cholesterol, a molecule that hardens the membrane which makes it harder for vesicles to rupture.[79,80] If these myelin GPMVs do not rupture, one way to induce them to rupture may be by changing the osmolarity of the surrounding solution. Alternatively, a protein, such as myelin basic protein (MBP) could be applied to the surface before the GPMVs, which would attract the membrane to the surface, stressing the vesicles and increasing likelihood of rupture.

Another approach to force GPMVs to rupture, could be to combine with a unique microfluidic technique which hydrodynamically drives movement of SLBs across surfaces.[81] In this novel technique, an SLB is formed in half of a microfluidic channel, and the membrane vesicles are incubated in the other half of the channel.[79] By flowing the fluid at a high rate, the shear force from the liquid moves the SLB and as it reaches adsorbed vesicles they rupture and fuse into the bilayer. The GPMVs could be adsorbed on the bare half of the channel and then the bilayer could be pushed until it ruptures these vesicles, planarizing them. Alternatively, unextruded myelin particles could also be tried instead of GPMVs. My earliest project involved implementing this shear force technique, and could

be a future project for myself or another lab member. The preliminary results from this project are included in Appendix A.

One side benefit of forming a lipid bilayer on the surface is that it might help with blocking. Persson et al showed that lipid bilayers did a better job than BSA at blocking the surface from nonspecific adsorption of quantum dots.[82] In the current project, which used BSA for blocking, there was sometimes nonspecific binding of varying degrees, making it harder to interpret data in some cases. It may be better for future experiments to block by rupturing lipid vesicles to form bilayer patches, instead of adsorbing BSA which can desorb.

Adsorbed myelin morphology may alter binding to rHIgM22

Another factor that might be contributing to decrease of binding between rHIgM22 and myelin particles, might the final morphology of the adsorbed myelin on the sensor surface. While it was argued above that planarization of the membrane might be advantageous, it is also possible that planarization could reduce binding, and that planarization has already been occurring. rHIgM22 is hypothesized to bind to lipid rafts. Lipid rafts are stiffer regions of the lipid bilayer that float in the fluid two dimensional membrane, and are mainly composed of sphingolipids, cholesterol, and proteins.[83] Some lipid rafts have been shown to need curvature to form. Ryu et al. have shown that some model lipid rafts in SLBs only localize at areas of negative curvature.[84] Therefore, a protein that only binds to intact rafts, which may include rHIgM22, may need a curved membrane to bind, and if planarization has been occurring, this could be reducing binding affinity. IgM O4 may still have been able to bind to myelin because its receptor is a simple sulfatide that does not need to be presented in a lipid raft.

We assumed that the extruded myelin particles were tangled aggregates of lipids and proteins (not hollow lipid spheres), with diameters approximately the size of the pores they were extruded through, and adsorbed to the surface in this morphology. We assumed the particle morphology was lipid-protein aggregates, and not vesicles, because myelin membranes are naturally multilayered structures with proteins linking membranes together

like glue.[68] It is possible that this is a wrong assumption, and the particles instead become vesicles during extrusion, and subsequently rupture on the hydrophilic SiO_2 surface. However, if hollow vesicles are the morphology and are adsorbing to the sensor surface, they may not rupture if they have a high cholesterol content due to their natural cell origin. So planarization of the myelin seems unlikely.

Nonetheless, it could be beneficial to rule out some of these questions by doing more characterization of the myelin particles. Dynamic light scattering is a simple process to determine particle size, and this could be performed before and after extrusion. Cryogenic transmission electron microscopy (cryo-TEM) could be used to obtain detailed morphology of the particles. Cryogenic scanning electron microscopy (cryo-SEM) or atomic force microscopy (AFM) performed in liquid could be used to gain nanometer resolution of the particles once they are applied to the sensor surface. Also, after particles have been applied to the surface, formation of a lipid bilayer could be determined by fluorescence recovery after photobleaching (FRAP), if a fluorescent label (e.g., the lipophilic FM 1-43) is applied to the lipid membrane.

If myelin vesicles have been forming by extrusion, and *not* rupturing on the sensor surface, they might be able to be induced to rupture by extruding with a high salt concentration solution, then diluting with a low salt concentration solution before applying the vesicle solution to the sensor.

If myelin vesicles have been forming by extrusion, and *have been rupturing* on the sensor surface, they could be prevented from rupturing by changing the sensor surface to become more hydrophobic. SiO_2, a very hydrophilic material which induces lipid vesicles to rupture, was used in these experiments. Alternatively, the sensor can be coated with aluminum oxide (Al_2O_3) instead of SiO_2, or with no coating and simply a bare metal surface. The challenge with not using SiO_2 is that a mechanical clamp would be needed to keep the PDMS attached to the chip and leaks would be more likely.

Hopefully, the actual receptors will be identified by biochemical and molecular biological assays performed by our Mayo Clinic collaborators, and we can incorporate this receptor into a supported lipid bilayer on the sensor surface. In the meantime, the

experiments performed in this project and follow-up projects may help lead to identifying the receptor(s), such as whether or not it is a protein, lipid, lipid raft component, or curvature dependent binding event.

In addition, the particle method might possibly provide a more accurate measurement of the kinetic values than one using an artificial supported lipid bilayer with the receptor incorporated in it, as it will incorporate many endogenous lipid and protein species which may alter the presentation of the receptor in a more natural way, which may alter the binding properties.

Growing cells directly on the sensor

Yet another approach could be to grow oligodendrocytes directly in the microfluidic chip, and then inject the antibodies directly over them. This method is probably the least feasible option, because binding events are only detectable within a few hundred nanometers of the sensor surface, and since cells are much larger than this, on the order of micrometers, very few binding antibodies would be detected by SPR. Additionally, it will be challenging to grow these delicate oligodendrocytes over several weeks in these microfluidic chips, but it could be attempted, so it is worth mentioning this option.

3.6 Conclusions

The goal of this project was to measure binding kinetics of rHIgM22 to an unknown receptor in myelin membrane using a nanohole based SPR biosensor. Because the receptor was unknown, we elected to passively adsorb extracted myelin membrane on the sensor surface. Due to very narrow SPR sensing window, within a few hundred nanometers from the surface, and much larger micrometer-sized myelin particles, we used an extrusion process to reduce the myelin particle size to the sensing window dimensions. This size reduction enabled the real-time label free detection of binding between myelin and the standard oligodendrocyte-labeling mouse IgM O4, which has been shown to help in mouse models of MS. However, we were unable to detect binding between myelin and the more

clinically relevant, potentially MS-treating, rHIgM22. This report shows that the extrusion and passive adsorption of extracted membrane is a potential approach for incorporating natural membranes onto SPR chips, although it may not work for certain receptors, which limits its applicability until further understanding of the binding knockout between rHIgM22 and myelin is achieved.

Including natural membranes on SPR chips is advantageous for several reasons. First, it allows unknown receptors to be incorporated on the sensor, allowing for screening and comparing of potential drugs with disease implicated membranes. This approach could help with future antibody studies by our Mayo Clinic collaborators. Their library of antibodies could be screened over myelin particles or other nervous tissue, to select the antibodies with the tightest binding profiles for further efficacy studies. Second, this whole membrane approach will present the receptors in a more natural state, by including more of the surrounding molecules, and thus may give more accurate kinetic rate constants. Many of the molecules in membranes are not commercially available or are highly expensive and unstable. Using this simple whole membrane extract approach could circumvent these limitations.

An obvious apparent downside to this approach is that is that it may not work for all membrane-protein interactions, such as rHIgM22 to the unknown receptor in myelin. Hopefully, further study will pinpoint what is breaking down the binding between this antibody and its receptor, and a solution can be found to enable this method to work for all molecular binding pairs.

Binding was observed between IgM O4 and extruded myelin, enabling the calculation of the apparent equilibrium dissociation constant, $K_{D,\ apparent} = 2.6 \pm 3.6 \times 10^{-9}$ M, the association kinetic constant, $k_a = 2.5 \pm 0.0 \times 10^4\ M^{-1}s^{-1}$, and the dissociation kinetic constants, $k_{d,\ fast} = 6.8 \pm 0.7 \times 10^{-3}\ s^{-1}$ and $k_{d,\ slow} = 6.6 \pm 0.3 \times 10^{-5}\ s^{-1}$.

4 Kinetics of rHIgM12 to Gangliosides

4.1 Contributions

In this chapter, the SPR chip fabrication and experiments were carried out by the author. Experiments were planned/interpreted with the help of Nathan Wittenberg and Sang-Hyun Oh as well as our collaborators at the Mayo Clinic, which includes Moses Rodriguez, Arthur Warrington, Xiaohua Xu, Jens Watzlawik, and Bharath Wootla. Antibodies were provided by these collaborators. Daehan Yoo, of our group, helped make molds for the SPR chips, and several group members helped build the spectroscopy setups, including Nathan Lindquist, Tim Johnson, Si Hoon Lee, and Jonah Shaver.

The second aim of this dissertation was to validate the binding partners and measure binding kinetics between rHIgM12 and gangliosides in SLB membranes using a nanohole array based SPR biosensor. The findings are presented here and are published in Xu et al., 2015.[85]

4.2 Introduction

Amyotrophic lateral sclerosis (ALS) is a disease in which motor neurons die, causing the muscles they innervate to atrophy, as illustrated in Figure 2. This process tragically leads to paralysis and death within 3-5 years, and there is currently no cure for ALS. One strategy for reversing ALS is to protect and regenerate neurons. As mentioned in the previous chapters, Dr. Rodriguez and his lab have discovered remarkable IgM antibodies which bind to oligodendrocytes, causing them to regenerate myelin, and have been therapeutic in animal models of MS. While creatively searching and finding these therapeutic human IgMs by searching through a Mayo Clinic serum bank from patients with monoclonal gammopathy which produces an excess of IgM antibodies, they discovered two novel human IgMs, sHIgM12 and sHIgM42, that bound to neuronal membranes and induced extension of their neurites, with a magnitude similar to laminin.[86] They realized these

neurite extending antibodies could be therapeutic in neuron degenerating diseases, such as amyotrophic lateral sclerosis (ALS) or stroke. So they generated a recombinant form of this antibody, rHIgM12, and tested it in mouse models of ALS, which resulted in functional improvements. Thus this antibody shows promise as a therapeutic drug for ALS. To learn more about the binding behavior of rHIgM12, they sought to determine its kinetic binding profile.

Initially the receptors for rHIgM12 were unknown. Xiaohua Xu et al. found that rHIgM12 colocalized with GM1 and lipid raft components.[87] From this result, they hypothesized that rHIgM12 may bind to a ganglioside. So they tested this antibody against multiple gangliosides using thin layer chromatography (TLC), discovering it appeared to bind to GD1a and GT1b, but not GM1 or GD1b. Based on these findings, we proposed to test the binding of rHIgM12 to these gangliosides in supported lipid bilayers (SLB) using our nanohole array based surface plasmon resonance (SPR) biosensor.

Gangliosides are sphingolipids with an oligosaccharide headgroup, and are found in the lipid bilayer of cell membranes, found throughout the body, but in higher concentrations in the nervous system. An illustration of the major brain gangliosides is

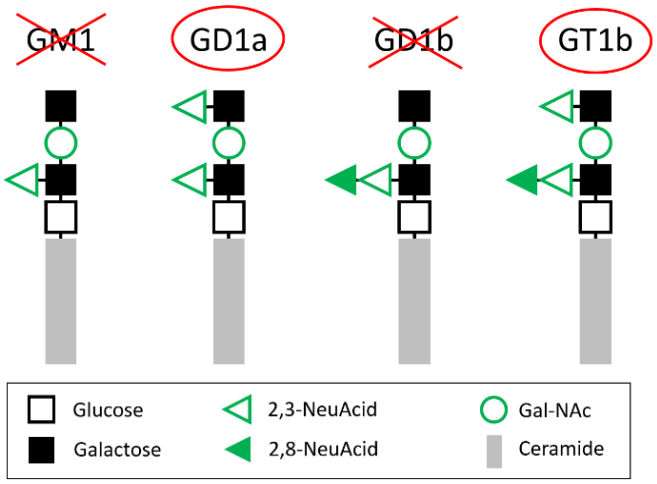

Figure 27: Structure of major brain gangliosides. Illustration of major gangliosides found in the brain and their simplified structures. The proposed antigens of rHIgM12, GD1a and GT1b, are indicated by red circles. Figure adapted from Vyas et al., 2001.[88]

shown in Figure 27. Gangliosides vary by the number or position of saccharides or sialic acids, which are variations of nine-carbon neuraminic acid.[88]

SPR is a thin film sensing technique able to measure molecules binding at its surface, within a sensing range of a few hundred nanometers. Because gangliosides are cell membrane receptors, a great approach to attach these receptors to an SPR sensor is by forming a receptor-doped lipid bilayer directly on the sensor surface. A lipid bilayer is a thin, two dimensional fluid membrane of ~4-6 nm thickness, which positions binding molecules well within the SPR sensing range. Another benefit to using a lipid bilayer to embed a receptor on an SPR sensor is that it may be oriented more similarly to its natural state than some immobilization strategies which can leave receptors in random orientations, some of which position the epitopes facing the surface. In additions, lipid bilayers are great at blocking the surface, so this helps reduce non-specific binding of test molecules.

Figure 28 is a schematic of the SPR chip used during the binding kinetic experiments in this report. The SPR sensor is a template-stripped silver nanohole array coated with a conformal layer of SiO_2, which is covered by a supported lipid bilayer (SLB) doped with the gangliosides, GT1b or GD1a. rHIgM12 is injected above the surface and can bind to gangliosides.

In these SPR binding kinetics experiments, we detected binding between rHIgM12 and GT1b (5 mol %) or GD1a (5 mol %) in SLBs, but not to GM1 (5 mol %) in SLBs or egg PC-only SLB (no receptor). In addition, we did not detect binding between a control human antibody, S128, to GT1b (5 mol %) in SLBs. Curves were analytically fit to the data using a least squares fitting, first a biphasic exponential decay curve to the dissociation data, followed by a monophasic exponential curve to the association data using the slower of the two dissociation rate constants. The rate constants between rHIgM12 and GT1b were calculated to be: $k_a = 2.19 \pm 0.196 \times 10^4\ M^{-1}s^{-1}$, $k_{d,\ slow} = 4.72 \pm 1.15 \times 10^{-4}\ s^{-1}$, and $k_{d,\ fast} = 8.37 \pm 1.58 \times 10^{-3}\ s^{-1}$. The rate constants between rHIgM12 and GD1a were calculated to be: $k_a = 1.79 \pm 0.516 \times 10^4\ M^{-1}s^{-1}$, $k_{d,\ slow} = 4.43 \pm 1.38 \times 10^{-4}\ s^{-1}$, and $k_{d,\ fast} = 7.94 \pm 1.60 \times 10^{-3}\ s^{-1}$. From these kinetic rate constants, the equilibrium constant, K_D,

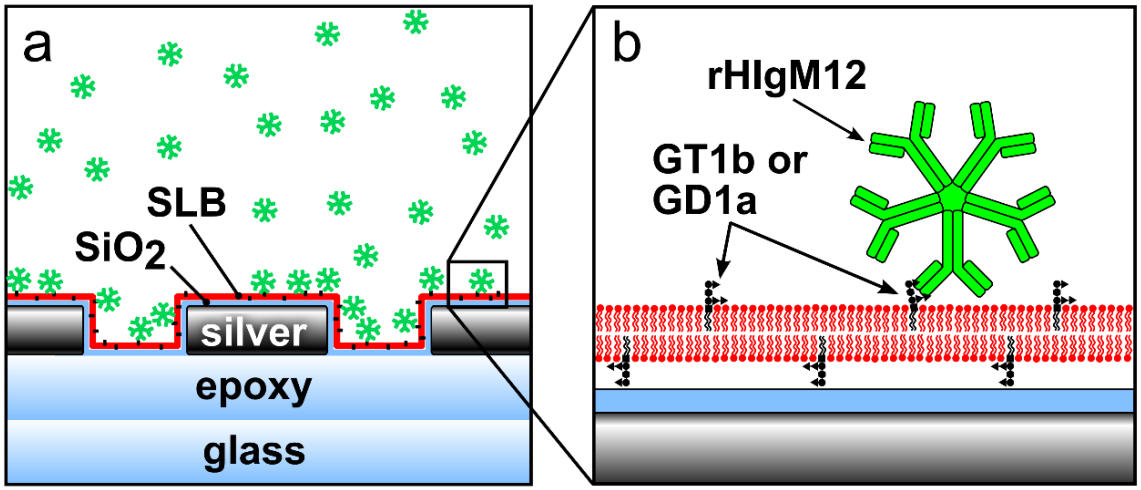

Figure 28: SPR chip coated with SLB doped with ganglioside receptors interacting with rHIgM12. Schematic of the nanohole array sensor coated with a supported lipid bilayer (SLB) doped with gangliosides GD1 or GT1b interacting with a solution of rHIgM12 during a binding kinetics experiment. (**a**) Chip consists of a silver film (100 nm thick) with nanoholes (~150 nm diameter, 500 nm spacing) on a glass slide, coated with SiO_2 (~15 nm thick) and bonded to a microfluidic chip. The surface is then coated by an SLB formed by vesicle rupture. rHIgM12 is then injected and binding is monitored. (**b**) Close-up view of the binding interaction.

was calculated. For rHIgM12 to GT1b, K_D = 24.8 ± 7.9 nM. For rHIgM12 to GD1a, K_D = 42.3 ± 20.6 nM. These low K_D's for rHIgM12, in the tens of nanometers, are at the lower end of dissociation constants of natural autoantibodies which are usually in the range of 10^{-5} to 10^{-8} molar.[6] Their high affinity may be related to their therapeutic effectiveness.

4.3 Materials and Methods

Some materials and methods here are identical or very similar to those of chapter 3, including source of antibodies, fabrication of SPR chips, solution preparation, experimental setup, and data analysis. The differences include different antibody, formation of supported lipid bilayers with ganglioside receptors, validation of SLB formation, and kinetic experiment procedure.

Antibodies

Antibodies were provided by our collaborators at the Mayo Clinic. rHIgM22 was expressed in F3B6 cells and rHIgM12 was expressed in CHO cells. Original antibodies were obtained from serum of human patients with Waldenstrom's macroglobulinemia, were sequenced, and plasmids were generated for the heavy and light chains and were transfected into the cells. Control IgM came from human serum.[5]

SPR Sensor Fabrication

Silicon Nanohole Array Mold

The sensors used in these experiments consisted of an array (periodicity = 500 nm) of nanoholes (diameter = 150 nm) in a silver film (thickness = 100 nm), covered by a PDMS microfluidic chip. In the first step, a nanohole array in silicon was made using nanoimprint lithography. A 100 nm thick thermal oxide was grown on a silicon wafer by wet oxidation at 1100°C for 11 min. The wafer was then broken into five ~30 × 30 mm pieces and rinsed with water and blown dry with N_2 gas. Thermal nanoimprint resist (NXR-1025, Nanonex Corp, NJ) was spin-coated at 3500 rpm for 1 min on the wafer pieces, followed by baking at 150°C for 1 min. A large 8 × 8 mm silicon nanoimprint stamp with a square array of pillars, 210 nm diameter, 350 nm depth, 500 nm periodicity, coated with a hydrophobic SAM (heptadecafluoro-1,1,2,2-tetrahydrodecyl)trichlorosilane, Gelest Inc., PA) was then nanoimprinted into the thermal resist, at a pressure of 300 psi and baked at 130°C for 2 min (Nanoimprinter). The thermal resist acted as a mask to allow etching holes into the underlying silicon. The oxide layer was etched by a gas mixture of 25 sccm CF_4 and 50 sccm Ar at 150W for 4 min (STS etcher, "PJSOXIDE" recipe). The nanoimprint resist mask was then removed by soaking in acetone for 30 min, followed by oxygen plasma to clean the surface at 100 sccm O_2 at 100W for 5 min (STS etcher, "O2CLEAN" recipe). Using the thermal oxide nanohole mask, the silicon was etched in the deep trench etcher for 2 min (DRIE, "CNF-14mT" recipe), followed by an oxygen plasma cleaning for 15-30 min (STS etcher, "O2CLEAN" recipe). The silicon oxide mask was then removed using a wet chemical etch (buffered oxide etch, which is a 1:10 dilution of HF acid). This last step

left the surface hydrophobic, so to make it hydrophilic to get it ready for template stripping, the chips were soaked in piranha solution, a 1:1 mixture of 96% sulfuric acid to 30% hydrogen peroxide (*CAUTION: this mixture is explosive, especially when organics are added to it*), for 10 min at 120°C, followed by extensive washing in deionized water and drying off with an N_2 gas.

Template Stripped Metal Film

The SPR sensor was then made by depositing metal on the silicon mold and transferring it to a glass slide, the surface of which was shown in Figure 13. First, silver was then deposited on the silicon nanohole array molds using an electron beam metal evaporation. 100 nm silver was deposited at 0.1-0.2 Å/s for the first 10 nm, followed by 90 nm at 1 A/s (Temescal or CHA evaporator). Glass slides that would be used to bond to and peel off the metal were cleaned with acetone, methanol, and isopropyl alcohol to remove any dust particles, followed by deionized water cleaning and N_2 gas drying. Optical epoxy (NOA 61, Norland Products Inc.) was applied to the glass slide with two small droplets (2.7 µL each) followed by placement of glass slide on the metal surface and making sure there was barely enough epoxy to cover the metal. The mated pieces were placed glass side down and left overnight to let as much epoxy come out of the nanoholes as possible. The epoxy was then cured by UV light for 3 hours, and then inverted and cured under UV light for 3 more hours. The epoxy was then aged on a hotplate at 55°C for at least 6 hours. The template-stripping process was then carried out by using a razor blade to pop the silicon mold off, leaving behind the glass/epoxy/silver surface.[46,47] Right after the stripping process, a thin (15-25 nm), conformal film of silicon dioxide was added to the surface by alternate layer deposition,[48] a variation of atomic layer deposition (ALD machine, Cambridge Nanotech), thus capping the silver, preventing further oxidation.

Microfluidic Chip

A microfluidic chip was then made by soft lithography and bonded to the SPR sensor, the finished product was shown in Figure 12. First a mold of the channel pattern was made

with epoxy (SU-8) on silicon. A design was made in AutoCAD, sent to a company to produce a film mask (CAD/Arts Services). The film mask was transferred to a square chrome-on-glass mask by photolithography. Next, a silicon wafer was cleaned by piranha solution (sulfuric acid and hydrogen peroxide, 1:1; *CAUTION: this solution is explosive*) and diluted HF (buffered oxide etchant, 10:1), and SU-8 50 was spin-coated at 2000 RPM for 30 s to make a 50 μm thick film. Baking was done at 65°C for 6 min then 95°C for 20 min. The copper hard mask pattern was transferred to the SU-8 and baked at 65°C for 1 min and 95°C for 5 min, and then put in developer for 10 min. The last step to make this mold was coating it with a SAM release layer (the same SAM used on the nanoimprint mold). Finally, polydimethylsiloxane (PDMS) (Sylgard 184, Dow Corning) was mixed (10:1 part A:B), degassed, and poured on the SU-8 mold and placed and heated on a hotplate overnight at 55°C. 25 × 25 mm squares of PDMS were cut and peeled off the mold, and holes were punched for inlets and outlets. The punched PDMS was washed with isopropyl alcohol, methanol, and acetone, followed by DI water and nitrogen gas to dry them. They were then placed in O_2 plasma at 100 sccm, 75 Watts, 7 seconds (Asher) along with the glass slide with nanohole array, and then shortly afterward the PDMS chip was attached to the glass slide.

Membrane Formation

Vesicle Formation

Vesicles were formed by a self-assembling method. Lipids used were L-α-phosphatidylcholine from chicken egg (egg PC) (Avanti Polar Lipids), GD1a and GT1b from bovine brain (Sigma), GM1 from bovine brain (Avanti), and 1,2-dimyristoyl-sn-glycero-3-phosphoethanolamine-N-(lissamine rhodamine B sulfonyl) (Rho-DMPE) (Avanti). Vesicles were used within 8 days of formation.

First, lipids stored in chloroform were mixed to desired ratios: egg PC only, egg PC/GT1b (95/5 mol %), egg PC/GD1a (95/5 mol %), or egg PC/GM1 (95/5 mol %) to obtain 1 mg lipid per mixture. For FRAP experiments, a fluorescent lipid, Rho-DMPE,

substituted 1 mol % of the egg PC. Next, the chloroform was evaporated off using a chamber connected to a vacuum pump for several hours.

Next, 0.5 mL of "EDTA buffer" was added to the lipid films, initiating self-assembly of vesicles. "EDTA buffer" was a calcium-free buffer composed of 100 mM NaCl, 10 mM tris(hydroxymethyl)aminomethane (Tris), and 1 mM ethylenediaminetetraacetic acid (EDTA), set to pH 6.5. The volume added made the vesicle solution concentration 1 mg lipid / 0.5 ml buffer. This hydration step was allowed to continue for several hours.

To make the vesicles unilamellar with 200 nm diameters, several steps were performed. First, the small vials of vesicles were sonicated for 10 minutes in a bath sonicator, which breaks the vesicles into smaller sizes, but a wide distribution of sizes and lamellarities. Finally, the vesicles were extruded to the final desired size by 15 passes through a polycarbonate filter with 200 nm pore diameters (Avanti Mini-Extruder, Avanti Polar Lipids, Inc.), resulting in a distribution of sizes nominally centered at 200 nm. This process also creates unilamellar vesicles which helps form a better bilayer.

Fluorescence Recovery After Photobleaching (FRAP)

FRAP experiments were carried out on an upright laser-scanning fluorescent upright confocal microscope (Olympus FluoView FV1000 BX2, Olympus), using FluoView software, and a 60× water objective (NA = 0.9). A bleaching experiment consisted of imaging an area (~211 × 211 μm) for 3 frames, then directing all lasers to be used at 100% in a smaller, circular spot (radius = ~10 μm) for ~10 s, then imaging for up to 10 minutes, monitoring the recovery of fluorescent molecules into the bleached spot.

FRAP images were analyzed with the software ImageJ (freely available by the NIH), Origin, and a MATLAB routine. For the plot of intensity recovery over time in the bleached spot, each image was normalized to background intensity by dividing the mean intensity of the bleached area from a mean intensity of a circular spot of the same size as the bleached spot on the side of the image. To get the diffusion coefficient, the routine by Jönsson and colleagues,[66] was used which takes a radial average of each spot and does a Hankel Transform to better estimate diffusion for spots that are not ideally bleached

(bleaching typically should be 1/10th the recovery time, but we had to bleach for a longer period of time).

Solution Preparation

Solutions of phosphate buffered saline (PBS, 0.01 M, pH 7.2) were degassed for several hours in a vacuum chamber. Most of the solutions were then loaded into syringes for buffer only injections, while a small fraction was mixed with antibody solutions to achieve desired concentrations (50, 100, or 200 nM), and then loaded into syringes. A stock solution of bovine serum albumin (BSA, 5 wt % in PBS, pH 7.2) had been prepared and loaded into syringes previously to allow time to get rid of air bubbles. Solutions were kept at 4°C until needed in the experiment, and were allowed to warm up to room temperature for roughly 30 min before being used in the experiment.

Spectroscopic Kinetic Measurements

Microscope/Spectrometer

The assembled microfluidic chip was placed on an inverted microscope stage (Eclipse Ti-S, Nikon) or a free-space optical setup. A figure and schematic of the microscope was shown in Figure 11. The optical train included a broadband light source, 2X (NA = 0.06) objective, an imaging spectrometer (MS257, Newport Corp.), and CCD camera (PIXIS 400B, Princeton Instruments). The imaging spectrometer and camera were controlled with custom LabVIEW (National Instruments) and analyzed with MATLAB (MathWorks) software.

Syringes with isopropyl alcohol were loaded into the syringe pumps (PHD2000, Harvard Apparatus) and connected to silicone tubing, which was connected to 4-way valves (IDEX, Upchurch Scientific). Isopropyl alcohol was flushed through the valve to get rid of air bubbles, and the connected to the microfluidic chip, and gently flushed to get rid of air bubbles for 20 minutes, followed by extensive washing with PBS.

Kinetic Experiments

For the kinetic experiments, first a supported lipid bilayer (SLB) was formed by diluting the vesicles to 1 mg/mL with 0.5 mL Tris buffer with calcium (100 mM NaCl, 10 mM Tris, 10 mM $CaCl_2$, pH 6.5), treating the SiO_2 surface with O_2 plasma (100 sccm O_2, 75W, 7 s, Asher), and then applying the vesicles to the SiO_2 surface as quickly as possible. The hydrophilic surface induced vesicle rupture and bilayer formation in a self-assembled fashion,[50,55] which we demonstrated with fluorescence after photobleaching (FRAP) experiments.[64,66]

During the rest of the experiment, all solutions consisted of 0.01 M phosphate-buffered saline (PBS), pH 6.5, with or without antibodies. After vesicle incubation, residual vesicles were rinsed off the surface. Next the surface was then blocked by 2% (w/v) bovine serum albumin (BSA) in PBS, followed by a washing step. Lastly, the antibodies were injected over the surface (association phase), followed by washing (dissociation phase). rHIgM12 was injected at 50, 100, or 200 nM and the control antibody S128 was injected at 100 nM. Kinetic experiments were performed at room temperature (~25°C).

Kinetic Data Processing and Analysis

Spectral images of the channels were recorded by the CCD camera, as was shown in Figure 14. The vertical axis of the images corresponds to a line from the chip (across the channels) projected into the entrance slit of the spectrometer. The horizontal axis of the images corresponds to that entering light spread into its component wavelengths by the grating inside the spectrometer. In this manner, spectra from 8 microfluidic channels could be collected simultaneously. Using MATLAB (MathWorks), the pixels in the images corresponding to each channel were selected to obtain a spectrum for each channel. To smooth the spectra, a 5th order polynomial was fit to a dip near 700 nm, and a minimum was calculated. A dip was chosen instead of a peak because it was more stable due to the light source intensity fluctuated a bit, probably because it did not have a power stabilizing feedback control. Plotting the position of the dip vs. time gave association and dissociation curves.

Nonlinear least squares curve fitting could then be performed as previously reported.[70,71] First, using Origin (OriginLab Corp), a double exponential decay was fit to the dissociation data to find $k_{d,\ fast}$ and $k_{d,\ slow}$,

$$R = R_a e^{-k_{d,fast}t} + R_b e^{-k_{d,slow}t}$$

followed by curve fitting to the association data using these dissociation rate constants and the analyte concentration to find k_a,

$$R = \frac{Ck_a R_{max}\left[1 - e^{-((Ck_a + k_d)t)}\right]}{Ck_a + k_d}$$

Finally, the apparent equilibrium constant, $K_{D,\ apparent}$, was calculated by $k_{d,\ slow}$ / k_a. Data with obvious drift in signal or other obvious artifacts were excluded from the analysis.

4.4 Results

Fluorescence Recovery After Photobleaching (FRAP)

To confirm vesicles applied to the sensor surface ruptured and formed a supported lipid bilayer, fluorescence recovery after photobleaching (FRAP) experiments were performed. These experiments were identical to the conditions of the kinetics experiments except for a few minor details. In these experiments, 1 mol % of fluorescently conjugated lipids (Texas Red-DHPE) were substituted in for egg PC lipids, for visualizing the membrane. Also the experiments were not performed in a microfluidic channel under flow conditions, but in a static condition, in a PDMS ring. Both of these differences are presumably minor differences.

FRAP results are shown in the Figure 29. Panel (a) shows the imaged area at t = -20, 0, 30, and 240 s. After t = -20 s, the bleaching lasers were turned on in a circular spot, and t = 0 s refers to the first frame imaged right after the bleaching step. The area in which fluorophores were bleached (and thus is black) is indicated by the dashed white circle. At t = 30 s, some of the fluorescence has recovered, meaning some of the bleached Texas Red conjugated lipids had diffused out of the bleaching region, while other lipids with

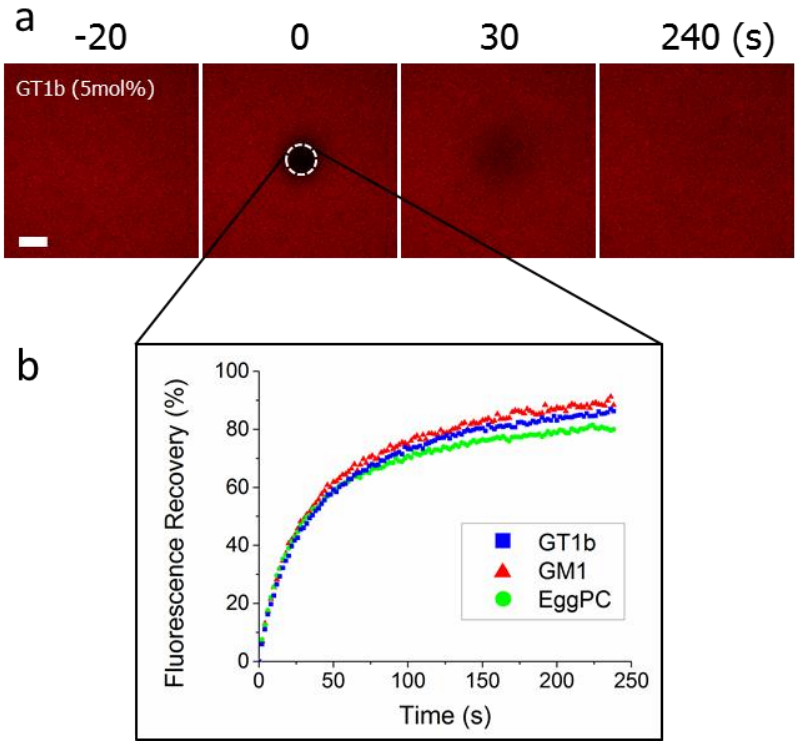

Figure 29: FRAP experiment confirms SLBs have formed from vesicles doped with gangliosides. Fluorescence recovery after photobleaching (FRAP) experiments were performed on chip surfaces coated with lipid vesicles doped with gangliosides to confirm rupturing occurred and a continuous supported lipid bilayer (SLB) had formed. (**a**) Fluorescence images of sample exposed to vesicles composed of egg PC with 5 mol % GT1b and 1 mol % Texas Red-DHPE. Bleaching lasers were activated between t = -20 s and 0 s, with images taken before and after bleaching. The circular region that was bleached is indicated by the dashed white line, and the intensity in this region is measured over time. Images at t = 30 and 240 s show a recovery of fluorescence in this spot, confirming a continuous lipid bilayer. If vesicles were still intact, no recovery would occur. (**b**) Mean fluorescence intensity over time in spot, normalized to pre/post bleach, for various lipid mixtures in vesicles. Calculated diffusion coefficient by the Hankel-Transform method[66] for membranes with egg PC only, GM1, or GT1b were D = 1.77 ± 0.09, 1.85 ± 0.01, and 2.02 ± 0.03 $\mu m^2/s$ (mean ± SEM), respectively. Scale bar indicates 20 µm. This figure was adapted from this author's publication: Xu, et al. Dis. Model. Mech. 2015, 8(8), 831-842.[85]

functioning Texas Red have diffused into this region. By t = 240 s, the fluorescence intensity has recovered to 90% of the starting level. Panel (b) is plot of the mean intensity in the spot over time, normalized to pre- and post-bleach intensities. Three membrane

mixtures are shown: membranes of egg PC alone, egg PC/GT1b (5 mol %), or egg PC/GM1 (5 mol %). All the membranes recovered, demonstrating that even with gangliosides in the vesicle mixtures, the vesicles still rupture on SiO_2. The diffusion coefficient for membranes with egg PC only, GM1, or GT1b were D = 1.77 ± 0.09, 1.85 ± 0.01, and 2.02 ± 0.03 $\mu m^2/s$ (mean ± SEM), respectively.

SPR Binding Kinetic Experiment Transmission Spectra

Figure 30 shows transmission spectra from a nanohole array during all the steps of an SPR binding kinetics experiment. Panel (a) shows the full spectrum collected, whereas panels (b)-(d) show a zoomed in view of the dip that is tracked during the experiment, before and after each step of the experiment. Panel (e) shows the wavelength shift of the dip over time. The 2 nm shift during the vesicle incubation stage (panel b) is evidence of the vesicles reaching the surface, and from the FRAP data we know they are rupturing during this step as well. The almost imperceptible shift before and after the BSA step (panel c) confirms nearly complete coverage with the lipid bilayer. A small shift after antibody injection (panel d) is evident indicates binding occurred, but it is the kinetic data shown in panel (e) that is most useful, showing in real-time antibodies binding during injection, and then dissociating during the washing step. The dip was chosen to be tracked instead of the peak because we found it to be slightly more stable. The peak has slightly more noise due to the light source not having a feedback loop to stabilize it. And the large shift during the BSA step is only due to a bulk shift of the highly concentrated BSA solution (2% w/v = 20 mg/ml ≈ 300 μM). The goal was to make sure any voids were completely filled with BSA to prevent all non-specific binding of antibody in the next step, and it looks like very few voids occurred, based on very little net BSA shift (panel c).

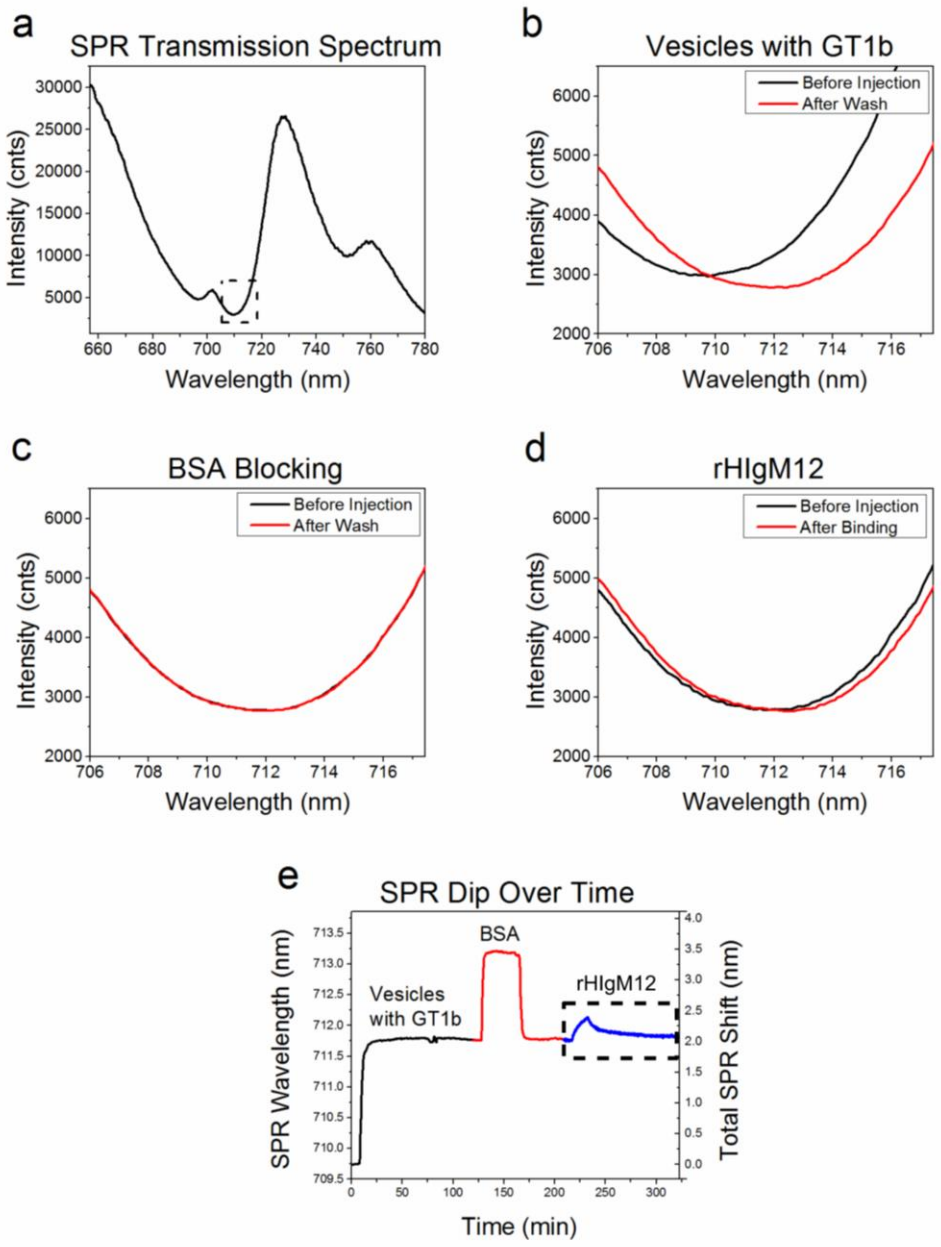

Figure 30: Transmission spectra from SPR chip during kinetic experiment between rHIgM12 and GT1b. Plots showing both the raw and processed kinetic data: (**a**) entire raw transmission spectra; (**b-d**) close up of the spectral dip before and after (**b**) vesicle incubation stage, (**c**) BSA blocking, and (**d**) rHIgM12 injection stages; (**e**) the dip is tracked over the course of the full experiment (preparation steps and kinetics step, which is indicated by the **dashed box**). The large shift during BSA blocking occurs due to the high concentration of BSA used. Only a small net shift due to BSA remains after the washing step, indicating that there were very few spots that needed to be blocked. This figure was adapted from this author's publication: Xu, et al. Dis. Model. Mech. 2015, 8(8), 831-842.[85]

SPR Binding Kinetic Curves

Figure 31 shows the SPR kinetic binding data between various concentrations of rHIgM12 and supported lipid bilayers doped with (a) 5 mol % GT1b, (b) 5 mol % GD1a, or (c) various negative control conditions. Two negative control experiments consisted of receptor alternatives: rHIgM12 injected over membrane with either 5 mol % GM1 or membrane with no receptor (egg PC alone). One negative control consists of an antibody alternative: S128 (another human IgM) injected over membrane with 5 mol % GT1b. Binding is clearly detected between rHIgM12 and GT1b and GD1a with up to ~1.2 nm shift, whereas no binding occurs in the negative control experiments. There is a small shift in the negative controls which could be due to nonspecific binding of IgMs to the surface or to bulk shift, since these concentrations which were all 100 nM.

The SPR binding curve data comes from the transmission minimum at ~700 nm plotted against the time course of the experiments. The experiments consist of two phases: the association phase, in which the antibody is injected over the membrane (starting at $t = 0$ s), and the dissociation phase, in which buffer only is injected over the membrane (staring at $t \approx 1200$ s). Analytical curves (black lines) are fit to the data by least squares analysis, from which the kinetic constants are obtained as fitting parameters. The equations used describe a single exponential association phase and double exponential decay phase. These are simplifications because the actual number of binding events could be as many as ten, due to the decavalent nature of the IgMs. However, it is difficult to discern greater than one binding event in the association phase (a phase in which both associating and dissociating events are occurring), or two dissociation events in the dissociation phase. There appears to be a fast and a slow dissociation rate, which are able to be differentiated during fitting. This analytical method we followed was used previously for the pentameric cholera toxin binding to GM1. This simplification also calculates the apparent equilibrium constant, $K_{D,\ apparent}$, using the slower dissociation rate constant because it is the rate determining step: $K_{D,\ apparent} = k_{d,\ slow} / k_a$. This analytical method, while not giving the individual kinetic constants for each binding event, does approximate the effective binding

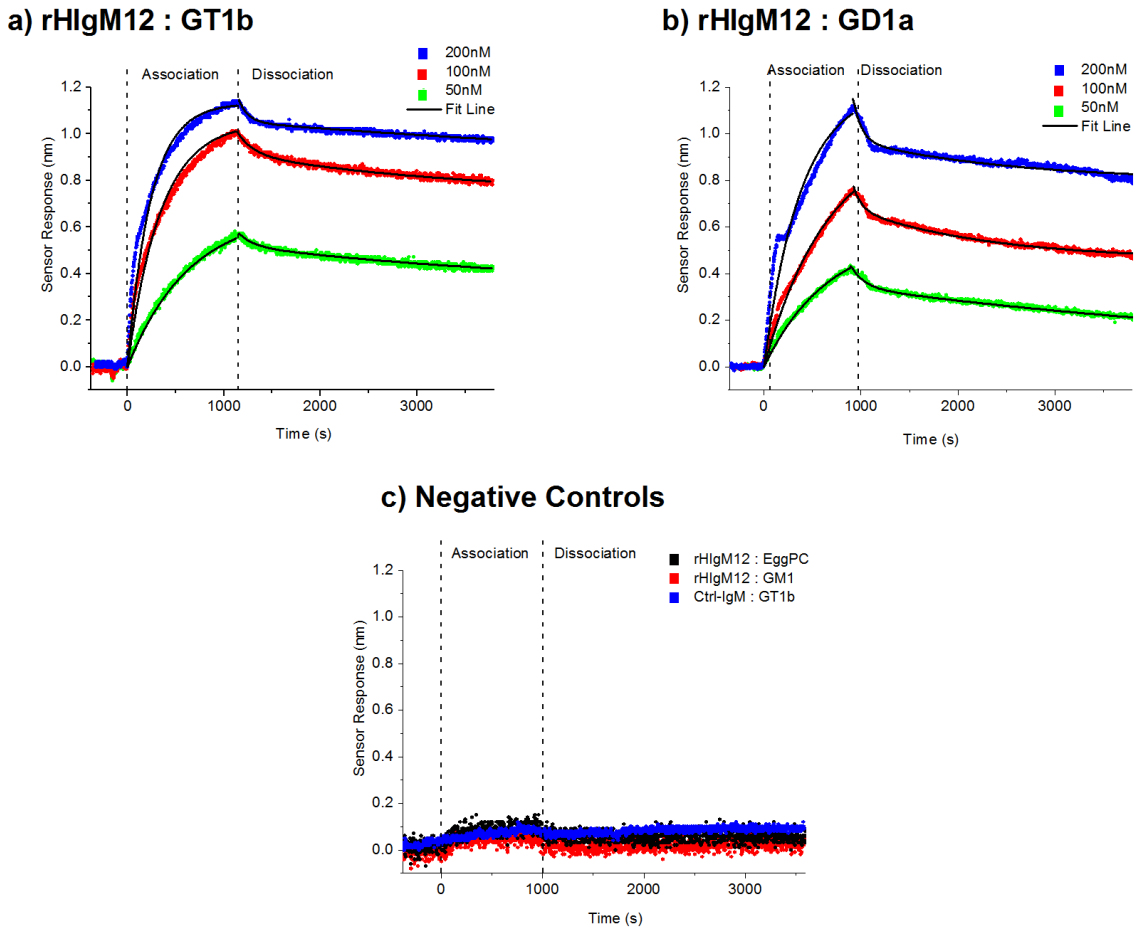

Figure 31: SPR kinetic curves of binding between rHIgM12 and gangliosides. SPR kinetic binding curves between rHIgM12 and supported lipid bilayers with 5 mol % (**a**) GT1b, (**b**) GD1a, or (**c**) GM1, egg PC only, or a control human IgM (S128) to membrane with 5 mol % GT1b. In panels (**a**) and (**b**), different concentrations of rHIgM12 are plotted with blue, red, and green squares indicating 200, 100, and 50 nM, and analytically fit curves are plotted in black. Binding is clearly evident between rHIgM12 and GT1b and GD1a and in a concentration dependent manner. In panel (**c**), no binding is observed in any of these negative control conditions. This figure was adapted from this author's publication: Xu, et al. Dis. Model. Mech. 2015, 8(8), 831-842.[85]

rate that will occur in the body since the entire pentameric IgM will be in the body, and not a monomeric species.

The kinetic constants were calculated to be: $K_{D,\ apparent}$ was 24.8 ± 7.9 nM and 42.3 ± 20.6 nM, respectively for GT1b and GD1a (mean ± SEM, N = 6 and 4, collected over 3

Table 3 Calculated Kinetic Rate and Thermodynamic Constants

Antibody	Antigen	K_D ($\times 10^{-9}$ M)	k_a ($\times 10^4$ $M^{-1}s^{-1}$)	$k_{d,\ slow}$ ($\times 10^{-4}$ s^{-1})	$k_{d,\ fast}$ ($\times 10^{-3}$ s^{-1})
rHIgM12	GT1b (5 mol % of SLB)	24.8 ± 7.9	2.19 ± 0.196	4.72 ± 1.15	8.37 ± 1.58
rHIgM12	GD1a (5 mol % of SLB)	42.3 ± 20.6	1.79 ± 0.516	4.43 ± 1.38	7.94 ± 1.60

and 2 days). The association rates between rHIgM12 and gangliosides were k_a = 2.19 ± 0.196 × 10^4 $M^{-1}s^{-1}$ to GT1b and k_a = 1.79 ± 0.516 × 10^4 $M^{-1}s^{-1}$ to GD1a. And the dissociation rates were $k_{d,\ slow}$ = 4.72 ± 1.15 × 10^{-4} s^{-1} and $k_{d,\ fast}$ = 8.37 ± 1.58 × 10^{-3} s^{-1} to GT1b, and $k_{d,\ slow}$ = 4.43 ± 1.38 × 10^{-4} s^{-1} and $k_{d,\ fast}$ = 7.94 ± 1.60 × 10^{-3} s^{-1} to GD1a. These results are compiled in Table 3.

4.5 Discussion

The IgMs studied in this report are monoclonal, polyreactive, natural autoantibodies. Their autoantibody designation refers to their binding to self-antigens, and their polyreactivity refers to their reactivity to many tissues instead of a single antigen. Their polyreactivity implies that they can't bind to each antigen as specifically, and thus bind less strongly to each antigen. Their affinities are typically on the order of 10^{-5}-10^{-8} M.[6] rHIgM12 has affinities on the lower end of this range, with $K_{D,\ apparent}$ of 24.8 ± 7.9 nM and 42.3 ± 20.6 nM, respectively for GT1b and GD1a. This high affinity could help explain why only a small dosage is needed for a therapeutic effect. A comparison with other natural autoantibodies of isotype IgM[89–92] can be seen in Table 4.

Table 4 Binding Properties of Natural Autoantibodies of Isotype IgM

IgM Antibody	Antigen	Method	K_D ($\times 10^{-9}$ M)	k_a ($\times 10^4$ $M^{-1}s^{-1}$)	$k_{d,\ slow}$ ($\times 10^{-4}$ s^{-1})	$k_{d,\ fast}$ ($\times 10^{-3}$ s^{-1})	Ref
rHIgM12	5% GT1b (in SLB)	SPR	24.8 ± 7.9	2.19 ± 0.196	4.72 ± 1.15	8.37 ± 1.58	this study
	5% GD1a (in SLB)	SPR	42.3 ± 20.6	1.79 ± 0.516	4.43 ± 1.38	7.94 ± 1.60	
mouse IgM O1	2% GalC (in SLB)	SPR	2.37 ± 0.56	69.8 ± 49.2	11.0 ± 5.1	-	69
mouse IgM O4	2% Sulf (in SLB)	SPR	2.19 ± 0.61	26.5 ± 17.1	3.73 ± 1.15	-	
F5-2	actin	SPR	40.3	1.85	7.46	-	89
	myosin		27.4	2.84	7.78	-	
	tubulin		68.0	1.67	11.4	-	
2E4	ssDNA	ELISA	40	-	-	-	90
	β-galactosidase		700	-	-	-	
	insulin		10,000	-	-	-	
274.RA.F11	IgG Fc frag.	ELISA	40,000	-	-	-	91
274.RA.F5	IgG Fc frag	ELISA	300	-	-	-	
Ab 50	IgG Fc frag	ELISA	10,000	-	-	-	92
	ssDNA		560	-	-	-	
	insulin		100,000	-	-	-	
	tetanus toxoid		6400	-	-	-	
Ab 52	IgG Fc frag	ELISA	30,000	-	-	-	
	ssDNA		1000	-	-	-	
	insulin		1000	-	-	-	
	tetanus toxoid		2500	-	-	-	

rHIgM12 binds strongly to membranes with GT1b and GD1a but not to GM1. This parallels another finding of avidity of other IgM antibodies (mouse IgMs O1 and O4).[69]

IgMs O1 and O4 bind to components of myelin in oligodendrocytes, and are used to determine the development stage of the oligodendrocyte. IgM O1 binds to galactocerebroside, a lipid with a galactose headgroup, with K_D = 2.37 ± 0.56 nM. IgM O4 binds to sulfatide, a lipid with a sulfate headgroup, with K_D = 2.19 ± 0.61 nM.

For antibody engineers, IgMs have not been considered an ideal molecule as a drug candidate. The pharmacokinetics of smaller (~150 kDa) and more specific monomeric IgGs can find and bind to their targets more tightly than the larger (~900 kDa) and less specific pentameric IgMs.[93] In addition, it goes against conventional logic that large molecules could pass the blood-brain barrier with its tight-junctions. However, it has been demonstrated by MRI that in mice with demyelinating disease, rHIgM22 injected outside the CNS, entered the CNS.[94]

In one respect, a low K_D (in the tens of nM) may not be surprising for IgM molecules. These antibodies are pentavalent antibodies, meaning they have up to ten binding sites. Multiple antigens bound simultaneously is referred to as avidity. Avidity is not just a summation of the individual binding events – each additional binding pair enhances the affinity of the other pairs. If one binding pair dissociates, the ligand does not freely diffuse away, effectively increasing the local concentration of the ligand, causing rebinding more likely to occur. Assuming multiple receptors can be reached by the ligand, increasing the binding capability of the ligand by two can increase avidity by an order of magnitude,[95] and increasing the binding capability to ten may increase avidity by 400 times.[96] Thus, a low K_D for a decavalent binder would not be surprising based on the avidity effect.

The equilibrium dissociation constant, K_D, has been a common metric in drug discovery to predict how well a drug candidate will bind in the body. However, it has been suggested recently that k_d is the better predictor of how well the drug candidate will stay bound.[8,9] A longer binding event can result in a lower drug dosage needed, and also may reduce off-target binding (to other receptors in the body) which are a big source of side-effects. A common way to discuss k_d is to put it in terms of half-lives, the amount of time that half the drug will stay bound. k_d is the inverse of the decay constant, τ. And $t_{1/2} = \tau \ln 2$. So, $t_{1/2} = 0.693 / k_d$. Some examples of drugs and their half-lives are shown in Table 5.

Table 5 Binding Affinity of Various Drugs

Drug	Target	K_D ($\times 10^{-9}$ M)	$k_{d,\ slow}$ ($\times 10^{-4}$ s^{-1})	$t_{1/2}$	Ref
losartan (Cozaar; Merck)	angiotensin II type 1 receptor (ATR1)	~350 nM	-	5 min	[8]
candesartan (Atacand; AstraZeneca)	angiotensin II type 1 receptor (ATR1)	~7 nM	-	66-152 min	[8]
aspirin	cyclooxygenase	-	-	irreversible	[98]
ibuprofen, naproxen	cyclooxygenase	-	-	reversible	
IgM O1	2% GalC (in SLB)	2.37 ± 0.56	11.0 ± 5.1	~11 min	[69]
IgM O4	2% Sulf (in SLB)	2.19 ± 0.61	3.73 ± 1.15	~30 min	
rHIgM12	5% GT1b (in SLB)	24.8 ± 7.9	4.72 ± 1.15	~25 min	this study
rHIgM12	5% GD1a (in SLB)	42.3 ± 20.6	4.43 ± 1.38	~26 min	

An example of increased efficacy by a slower dissociation rate is the comparison of the blood pressure lowering drugs candesartan and losartan. These antagonist drugs both target and block membrane-bound angiotensin II type 1 receptors, which causes the renin-angiotensin system to reduce blood pressure. Candesartan has a longer half-life however, possibly due to a more elaborate two-step receptor isomerization binding mechanism. Studies have shown candesartan has greater clinical efficacy than losartan as measured by maximum diastolic blood pressure and survival rate. These therapeutic advantages have been suggested to be due to candesartan's longer half-life.[8,97]

For some disease therapies, a fast kinetic profile is desirable. For example, the drug aspirin, which is often used to treat pain, inflammation, and fevers, binds to cyclooxygenase irreversibly, which platelets cannot overcome and can lead to bleeding, a

negative side effect for these treatments. In comparison, the similar drugs ibuprofen and naproxen bind to cyclooxygenase reversibly, thus advantageously do not result in bleeding. The desired clinical outcome, however, determine which drugs are best, and which kinetic profile is desired. The anti-coagulant behavior of aspirin is actually used to help prevent strokes, heart attacks, and blood clots.[98,99]

For many physiological events, a longer residence time of a molecule with its receptor leads to a longer biological effect.[100] In our study, the rHIgM12 half-lives (based on $k_{d,\,slow}$) are around 25 and 26 min for GT1b and GD1a, respectively. Compared to other therapeutic IgMs, rHIgM12 to GD1a or GT1b has similar average dwell times to IgM O4 to sulfatide, and longer average dwell times than IgM O1 to GalC..

To confirm that binding of rHIgM12 was specific to the gangliosides GT1b and GD1a, several negative control experiments were performed. In one negative control experiment, the SLB had no receptors (just egg PC), while another included 5 mol % GM1. In both cases no binding was detected to rHIgM12 (100 nM). In a third negative control experiment, an alternative human IgM (S128, 100 nM) was injected over GT1b. Again, no binding was detected.

It is worth adding a few comments on working with supported lipid bilayers in kinetic experiments. While it is beneficial to use supported lipid bilayers to mimic cell membranes with their two-dimensional fluidity, one major challenge with working with them is that they are extremely susceptible to air bubbles. A single air bubble can ruin an experiment. The air bubble can strip membrane off of the surface, which may not get refilled, and thus may present a bare surface which can result in nonspecific binding, which cannot be differentiated in the SPR signal. Great care is needed to degas solutions and make sure no air enters any of the equipment during long experiments. When this condition is achieved, supported lipid bilayers can be better at blocking surfaces from nonspecific binding than BSA.[82]

4.6 Conclusions

Nanohole array SPR biosensors were built and coated with fluid supported lipid bilayers with ganglioside receptors, GD1a and GT1b, verified by FRAP measurements. Binding kinetic experiments between rHIgM12 and GT1b or GD1a in supported lipid bilayers enabled calculation of association kinetic constants $k_a = 2.19 \pm 0.196 \times 10^4$ $M^{-1}s^{-1}$ (GT1b) and $1.79 \pm 0.516 \times 10^4$ $M^{-1}s^{-1}$ (GD1a), and dissociation rate constants $k_{d,\,slow} = 4.72 \pm 1.15 \times 10^{-4}$ s^{-1} and $k_{d,\,fast} = 8.37 \pm 1.58 \times 10^{-3}$ s^{-1} (GT1b), and $k_{d,\,slow} = 4.43 \pm 1.38 \times 10^{-4}$ s^{-1} and $k_{d,\,fast} = 7.94 \pm 1.60 \times 10^{-3}$ s^{-1} (GD1a). The thermodynamic equilibrium constants were calculated to be $K_{D,\,apparent} = 24.8 \pm 7.9$ nM (GT1b) and 42.3 ± 20.6 nM (GD1a). Control experiments of rHIgM12 to GM1 in SLB or egg PC-only membrane, and a control IgM, S128, to GT1b in SLB all resulted in no binding.

Future directions could include repeating the experiment with more membrane components to more closely mimic the actual cell membrane, such as including cholesterol and sphingomyelin. Typical cells have up to 30% cholesterol, and neurons have a high percentage of sphingolipids as well, so these mixtures would likely result in lipid raft formation. Lipid rafts could alter the presentation of the gangliosides, such as the tilt or packing density of the receptors, which may reduce the amount of binding due to steric hindrance by gangliosides or shielding by the large, decavalent IgM. With these more complex membranes, it is important to test above and below physiological temperature (37.5 °C), as lipid rafts in three part mixtures have melting temperatures in this range (~35-38°C).[101] Also the percentage of gangliosides could be altered. Cremer et al. showed that GM1 can self-cluster and reduce the binding affinity of cholera toxin.[72]

5 Overall Impact of Dissertation

The overall impact of this dissertation is twofold. First, this research has demonstrated that natural membranes can be incorporated on SPR chips using the extrusion method. There are several benefits to be able to use natural membranes for drug screening. One benefit is being able to incorporate cell membranes that are implicated in diseases to find candidate drugs which bind to them. This approach led our collaborators at the Mayo Clinic to discover rHIgM22 binding to myelin for treating multiple sclerosis and rHIgM12 binding to neuronal membrane for treating amyotrophic lateral sclerosis. Adding SPR during this discovery process will allow earlier comparisons of binding kinetics to find the strongest binders, a goal for many therapeutic drugs. Stronger binders may prolong a drug's effects, by continuing to act on the receptor. In addition, less drug may need to be administered. Conversely, in some physiological situations, a quick dissociating drug may be desired. Knowing the kinetic behavior will help determine which drug candidates to choose in each case. Another benefit of SPR is that no fluorescent tags need to be added to the drug, a process which takes time, costs money, and can alter binding behavior. A caveat to this membrane extrusion approach is that it worked for mouse IgM O4, but we had difficulty detecting binding of rHIgM22 to myelin. Further study to determine what caused this lack of detection, and further validation of this extrusion method with other molecules will be needed.

Second, this research has verified the binding partners and measured the binding kinetics between rHIgM12 and GT1b and GD1a. Knowing the kinetic rate constants help to compare it to other drugs, and hint at why such a small dosage may be needed.

References

(1) Kantarci, O. H.; Pirko, I.; Rodriguez, M. Novel Immunomodulatory Approaches for the Management of Multiple Sclerosis. *Clin. Pharmacol. Ther.* **2013**, *95* (1), 32–44.

(2) World Health Organization. *Atlas: Multiple Sclerosis Resources in the World 2008*; 2008.

(3) Kiernan, M. C.; Vucic, S.; Cheah, B. C.; Turner, M. R.; Eisen, A.; Hardiman, O.; Burrell, J. R.; Zoing, M. C. Amyotrophic Lateral Sclerosis. *Lancet* **2011**, *377* (9769), 942–955.

(4) Rodriguez, M.; Warrington, A. E.; Pease, L. R. Invited Article: Human Natural Autoantibodies in the Treatment of Neurologic Disease. *Neurology* **2009**, *72* (14), 1269–1276.

(5) Xu, X.; Wittenberg, N. J.; Jordan, L. R.; Kumar, S.; Watzlawik, J. O.; Warrington, A. E.; Oh, S.-H.; Rodriguez, M. A Patterned Recombinant Human IgM Guides Neurite Outgrowth of CNS Neurons. *Sci. Rep.* **2013**, *3*, 2267.

(6) Lutz, H. U.; Binder, C. J.; Kaveri, S. Naturally Occurring Auto-Antibodies in Homeostasis and Disease. *Trends Immunol.* **2009**, *30* (1), 43–51.

(7) Leslie, M. Cleanup Crew. *Science* **2015**, *347* (6226), 1058–1061.

(8) Copeland, R. A.; Pompliano, D. L.; Meek, T. D. Drug-Target Residence Time and Its Implications for Lead Optimization. *Nat. Rev. Drug Discov.* **2006**, *5* (9), 730–739.

(9) Núñez, S.; Venhorst, J.; Kruse, C. G. Target-Drug Interactions: First Principles and Their Application to Drug Discovery. *Drug Discov. Today* **2012**, *17* (1-2), 10–22.

(10) Wood, R. W. XLII. On a Remarkable Case of Uneven Distribution of Light in a Diffraction Grating Spectrum. *Philos. Mag. Ser. 6* **1902**, *4* (21), 396–402.

(11) Wood, R. W. Anomalous Diffraction Gratings. *Phys. Rev.* **1935**, *48* (12), 928–936.

(12) Langmuir, I. Oscillations in Ionized Gases. *Proc. Natl. Acad. Sci. U. S. A.* **1928**, *14*, 627–637.

(13) Tonks, L.; Langmuir, I. Oscillations in Ionized Gases. *Phys. Rev.* **1929**, *33* (2), 195–210.

(14) Bohm, D.; Gross, E. P. Theory of Plasma Oscillations. A. Origin of Medium-like Behavior. *Phys. Rev.* **1949**, *75* (12), 1851–1864.

(15) Bohm, D.; Gross, E. P. Theory of Plasma Oscillations. B. Excitation and Damping of Oscillations. *Phys. Rev.* **1949**, *75* (12), 1864–1876.

(16) Pines, D.; Bohm, D. A Collective Description of Electron Interactions: II. Collective vs Individual Particle Aspects of the Interactions. *Phys. Rev.* **1952**, *85* (2), 338–353.

(17) Palmer, Jr., C. H. Parallel Diffraction Grating Anomalies. *J. Opt. Soc. Am.* **1952**, *42* (4), 269.

(18) Palmer, Jr., C. H. Diffraction Grating Anomalies II Coarse Gratings. *J. Opt. Soc. Am.* **1956**, *46* (1), 50.

(19) Ritchie, R. H. Plasma Losses by Fast Electrons in Thin Films. *Phys. Rev.* **1957**, *106* (5), 874–881.

(20) Kretschmann, E.; Raether, H. Radiative Decay of Non-Radiative Surface Plasmons Excited by Light. *Z. Naturforsch.* **1968**, *23* (November 1968), 2135–2136.

(21) Otto, A. Excitation of Nonradiative Surface Plasma Waves in Silver by the Method of Frustrated Total Reflection. *Zeitschrift fur Phys.* **1968**, *216* (4), 398–410.

(22) Kretschmann, E. Die Bestimmung Optischer Konstanten von Metallen Durch Anregung von Oberflächenplasmaschwingungen. *Zeitschrift für Phys.* **1971**, *241* (4), 313–324.

(23) Liedberg, B.; Nylander, C.; Lundström, I. Biosensing with Surface Plasmon Resonance--How It All Started. *Biosens. Bioelectron.* **1995**, *10* (8), i – ix.

(24) Homola, J.; Yee, S. S.; Gauglitz, G. Surface Plasmon Resonance Sensors: Review. *Sensors Actuators, B Chem.* **1999**, *54* (1), 3–15.

(25) Liedberg, B. O.; Nylander, C.; Lundstrom, I. Surface Plasmon Resonance for Gas Detection and Biosensing. *Sensors and Actuators* **1983**, *4*, 299–304.

(26) Nylander, C.; Liedberg, B.; Lind, T. Gas Detection by Means of Surface Plasmon Resonance. *Sensors and Actuators* **1982**, *3*, 79–88.

(27) Ebbesen, T. W.; Lezec, H. J.; Ghaemi, H. F.; Thio, T.; Wolff, P. A. Extraordinary Optical Transmission through Sub-Wavelength Hole Arrays. *Nature* **1998**, *391*, 667–669.

(28) Bethe, H. A. Theory of Diffraction by Small Holes. *Phys. Rev.* **1944**, *66* (7-8), 163–182.

(29) Lesuffleur, A.; Im, H.; Lindquist, N. C.; Oh, S. Periodic Nanohole Arrays with Shape-Enhanced Plasmon Resonance as Real-Time Biosensors. *Appl. Phys. Lett.* **2007**, *90*, 1–3.

(30) Lindquist, N. C.; Lesuffleur, A.; Oh, S. H. Periodic Modulation of Extraordinary Optical Transmission through Subwavelength Hole Arrays Using Surrounding Bragg Mirrors. *Phys. Rev. B - Condens. Matter Mater. Phys.* **2007**, *76* (15), 1–5.

(31) Lindquist, N. C.; Lesuffleur, A.; Oh, S. Lateral Confinement of Surface Plasmons and Polarization-Dependent Optical Transmission Using Nanohole Arrays with a Surrounding Rectangular Bragg Resonator. *Appl. Phys. Lett.* **2007**, *91*, 3–5.

(32) Lindquist, N. C.; Lesuffleur, A.; Im, H.; Oh, S. Sub-Micron Resolution Surface Plasmon Resonance Imaging Enabled by Nanohole Arrays with Surrounding Bragg Mirrors for Enhanced Sensitivity and Isolation. *Lab Chip* **2009**, *9* (3), 382–387.

(33) Brolo, A. G.; Gordon, R.; Leathem, B.; Kavanagh, K. L. Surface Plasmon Sensor Based on the Enhanced Light Transmission through Arrays of Nanoholes in Gold Films. *Langmuir* **2004**, *20* (12), 4813–4815.

(34) Escobedo, C.; Brolo, A. G.; Gordon, R.; Sinton, D. Flow-through vs Flow-over: Analysis of Transport and Binding in Nanohole Array Plasmonic Biosensors. *Anal. Chem.* **2010**, *82* (24), 10015–10020.

(35) Eftekhari, F.; Escobedo, C.; Ferreira, J.; Duan, X.; Girotto, E. M.; Brolo, A. G.; Gordon, R.; Sinton, D. Nanoholes as Nanochannels: Flow-through Plasmonic Sensing. *Anal. Chem.* **2009**, *81* (11), 4308–4311.

(36) Im, H.; Lindquist, N. C.; Lesuffleur, A.; Oh, S. H. Atomic Layer Deposition of Dielectric Overlayers for Enhancing the Optical Properties and Chemical Stability of Plasmonic Nanoholes. *ACS Nano* **2010**, *4* (2), 947–954.

(37) Feuz, L.; Jönsson, P.; Jonsson, M. P.; Höök, F. Improving the Limit of Detection of Nanoscale Sensors by Directed Binding to High-Sensitivity Areas. *ACS Nano* **2010**, *4* (4), 2167–2177.

(38) Lee, S. H.; Bantz, K. C.; Lindquist, N. C.; Oh, S. H.; Haynes, C. L. Self-Assembled Plasmonic Nanohole Arrays. *Langmuir* **2009**, *25* (23), 13685–13693.

(39) Lee, S. H.; Lindquist, N. C.; Wittenberg, N. J.; Jordan, L. R.; Oh, S.-H. Real-Time Full-Spectral Imaging and Affinity Measurements from 50 Microfluidic Channels Using Nanohole Surface Plasmon Resonance. *Lab Chip* **2012**, *12* (20), 3882–3890.

(40) Löfås, S.; Johnsson, B.; Edstrom, A.; Hansson, A.; Lindquist, G.; Muller Hillgren, R. M.; Stigh, L. Methods for Site Controlled Coupling to Carboxymethyldextran Surfaces in Surface Plasmon Resonance Sensors. *Biosens. Bioelectron.* **1995**, *10* (9-10 -10 pt 1-2), 813–822.

(41) Johnsson, B.; Löfås, S.; Lindquist, G. Immobilization of Proteins to a Carboxymethyldextran-Modified Gold Surface for Biospecific Interaction Analysis in Surface Plasmon Resonance Sensors. *Anal Biochem* **1991**, *198* (2), 268–277.

(42) Löfås, S.; Johnsson, B. A Novel Hydrogel Matrix on Gold Surfaces in Surface Plasmon Resonance Sensors for Fast and Efficient Covalent Immobilization of Ligands. *J. Chem. Soc. Chem. Commun.* **1990**, No. 21, 1526.

(43) Liedberg, B.; Lundström, I.; Stenberg, E. Principles of Biosensing with an Extended Coupling Matrix and Surface Plasmon Resonance. *Sensors Actuators B Chem.* **1993**, *11* (1-3), 63–72.

(44) Jönsson, U.; Fagerstam, L.; Ivarsson, B.; Johnsson, B.; Karlsson, R.; Lundh, K.; Lofas, S.; Persson, B.; Roos, H.; Ronnberg, I.; et al. Real-Time Biospecific Interaction Analysis Using Surface Plasmon Resonance and a Sensor Chip Technology. *Biotechniques* **1991**, *11* (5).

(45) Jönsson, U.; Malmqvist, M. Real Time Biospecific Interaction Analysis. The Integration of Surface Plasmon Resonance. Detection, General Biospecific Interface Chemistry and Microfluidics into One Analytical System. *Adv. Biosens.* **1992**, *2*, 291–336.

(46) Im, H.; Lee, S. H.; Wittenberg, N. J.; Johnson, T. W.; Lindquist, N. C.; Nagpal, P.; Norris, D. J.; Oh, S. H. Template-Stripped Smooth Ag Nanohole Arrays with Silica Shells for Surface Plasmon Resonance Biosensing. *ACS Nano* **2011**, *5* (8), 6244–6253.

(47) Nagpal, P.; Lindquist, N. C.; Oh, S.-H.; Norris, D. J. Ultrasmooth Patterned Metals for Plasmonics and Metamaterials. *Science* **2009**, *325* (5940), 594–597.

(48) Hausmann, D.; Becker, J.; Wang, S.; Gordon, R. G. Rapid Vapor Deposition of Highly Conformal Silica Nanolaminates. *Science* **2002**, *298* (5592), 402–406.

(49) Singer, S. J.; Nicolson, G. L. The Fluid Mosaic Model of the Structure of Cell Membranes. *Science* **1972**, *175* (4023), 720–731.

(50) Tamm, L. K.; McConnell, H. M. Supported Phospholipid Bilayers. *Biophys. J.* **1985**, *47* (1), 105–113.

(51) Brian, A. A.; McConnell, H. M. Allogeneic Stimulation of Cytotoxic T Cells by Supported Planar Membranes. *Proc. Natl. Acad. Sci. U. S. A.* **1984**, *81* (19), 6159–6163.

(52) Cremer, P. S.; Boxer, S. G. Formation and Spreading of Lipid Bilayers on Planar Glass Supports. *J. Phys. Chem. B* **1999**, *103* (13), 2554–2559.

(53) Cooper, M. A.; Try, A. C.; Carroll, J.; Ellar, D. J.; Williams, D. H. Surface Plasmon Resonance Analysis at a Supported Lipid Monolayer. *Biochim. Biophys. Acta* **1998**, *1373* (1), 101–111.

(54) Cooper, M. A.; Hansson, A.; Löfås, S.; Williams, D. H. A Vesicle Capture Sensor Chip for Kinetic Analysis of Interactions with Membrane-Bound Receptors. *Anal. Biochem.* **2000**, *277* (2), 196–205.

(55) Yang, T.; Jung, S.; Mao, H.; Cremer, P. S. Fabrication of Phospholipid Bilayer-Coated Microchannels for On-Chip Immunoassays. *Anal. Chem.* **2001**, *73* (2), 165–169.

(56) Keller, C. A.; Glasmästar, K.; Zhdanov, V. P.; Kasemo, B. Formation of Supported Membranes from Vesicles. *Phys. Rev. Lett.* **2000**, *84* (23), 5443–5446.

(57) Reimhult, E.; Höök, F.; Kasemo, B. Intact Vesicle Adsorption and Supported Biomembrane Formation from Vesicles in Solution: Influence of Surface Chemistry, Vesicle Size, Temperature, and Osmotic Pressure. *Langmuir* **2003**, *19* (5), 1681–1691.

(58) Jonsson, M. P.; Jönsson, P.; Dahlin, A. B.; Höök, F. Supported Lipid Bilayer Formation and Lipid-Membrane-Mediated Biorecognition Reactions Studied with a New Nanoplasmonic Sensor Template. *Nano Lett.* **2007**, *7* (11), 3462–3468.

(59) Höök, F.; Stengel, G.; Dahlin, A. B.; Gunnarsson, A.; Jonsson, M. P.; Jönsson, P.; Reimhult, E.; Simonsson, L.; Svedhem, S. Supported Lipid Bilayers, Tethered Lipid Vesicles, and Vesicle Fusion Investigated Using Gravimetric, Plasmonic, and Microscopy Techniques. *Biointerphases* **2008**, *3* (2), FA108.

(60) Schürholz, T.; Schindler, H. Lipid-Protein Surface Films Generated from Membrane Vesicles: Selfassembly, Composition, and Film Structure. *Eur. Biophys. J.* **1991**, *20* (2), 71–78.

(61) Reimhult, E.; Zäch, M.; Höök, F.; Kasemo, B. A Multitechnique Study of Liposome Adsorption on Au and Lipid Bilayer Formation on SiO2. *Langmuir* **2006**, No. 22, 3313–3319.

(62) Richter, R. P.; Bérat, R.; Brisson, A. R. Formation of Solid-Supported Lipid Bilayers: An Integrated View. *Langmuir* **2006**, *22* (8), 3497–3505.

(63) Lasic, D. D. *Liposomes in Gene Delivery*; CRC Press, 1997.

(64) Axelrod, D.; Koppel, D. E.; Schlessinger, J.; Elson, E.; Webb, W. W. Mobility Measurement by Analysis of Fluorescence Photobleaching Recovery Kinetics. *Biophys. J.* **1976**, *16* (9), 1055–1069.

(65) Soumpasis, D. M. Theoretical Analysis of Fluorescence Photobleaching Recovery Experiments. *Biophys. J.* **1983**, *41* (1), 95–97.

(66) Jönsson, P.; Jonsson, M. P.; Tegenfeldt, J. O.; Höök, F. A Method Improving the Accuracy of Fluorescence Recovery after Photobleaching Analysis. *Biophys. J.* **2008**, *95* (11), 5334–5348.

(67) Braun, D.; Fromherz, P. Fluorescence Interference-Contrast Microscopy of Cell Adhesion on Oxidized Silicon. *Appl. Phys. A Mater. Sci. Process.* **1997**, *65* (4-5), 341–348.

(68) Min, Y.; Kristiansen, K.; Boggs, J. M.; Husted, C.; Zasadzinski, J. A.; Israelachvili, J. Interaction Forces and Adhesion of Supported Myelin Lipid Bilayers Modulated by Myelin Basic Protein. *Proc. Natl. Acad. Sci. U. S. A.* **2009**, *106* (9), 3154–3159.

(69) Wittenberg, N. J.; Im, H.; Xu, X.; Wootla, B.; Watzlawik, J.; Warrington, A. E.; Rodriguez, M.; Oh, S. H. High-Affinity Binding of Remyelinating Natural Autoantibodies to Myelin-Mimicking Lipid Bilayers Revealed by Nanohole Surface Plasmon Resonance. *Anal. Chem.* **2012**, *84* (14), 6031–6039.

(70) O'Shannessy, D. J.; Brigham-Burke, M.; Soneson, K. K.; Hensley, P.; Brooks, I. Determination of Rate and Equilibrium Binding Constants for Macromolecular Interactions Using Surface Plasmon Resonance: Use of Nonlinear Least Squares Analysis Methods. *Anal. Biochem.* **1993**, *212* (2), 457–468.

(71) Kuziemko, G. M.; Stroh, M.; Stevens, R. C. Cholera Toxin Binding Affinity and Specificity for Gangliosides Determined by Surface Plasmon Resonance. *Biochemistry* **1996**, *35* (20), 6375–6384.

(72) Shi, J.; Yang, T.; Kataoka, S.; Zhang, Y.; Diaz, A. J.; Cremer, P. S. GM1 Clustering Inhibits Cholera Toxin Binding in Supported Phospholipid Membranes. *J. Am. Chem. Soc.* **2007**, *129* (18), 5954–5961.

(73) Middleton, E. R.; Rhoades, E. Effects of Curvature and Composition on α-Synuclein Binding to Lipid Vesicles. *Biophys. J.* **2010**, *99* (7), 2279–2288.

(74) Nakanishi, K.; Sakiyama, T.; Imamura, K. On the Adsorption of Proteins on Solid Surfaces, a Common but Very Complicated Phenomenon. *J. Biosci. Bioeng.* **2001**, *91* (3), 233–244.

(75) Rabe, M.; Verdes, D.; Seeger, S. Understanding Protein Adsorption Phenomena at Solid Surfaces. *Adv. Colloid Interface Sci.* **2011**, *162* (1-2), 87–106.

(76) Henry, M.; Dupont-Gillain, C.; Bertrand, P. Conformation Change of Albumin Adsorbed on Polycarbonate Membranes as Revealed by ToF-SIMS. *Langmuir* **2003**, *19* (15), 6271–6276.

(77) Keller, C. A.; Kasemo, B. Surface Specific Kinetics of Lipid Vesicle Adsorption Measured with a Quartz Crystal Microbalance. *Biophys. J.* **1998**, *75* (3), 1397–1402.

(78) Holowka, D.; Baird, B. Structural Studies on the Membrane-Bound Immunoglobulin E-Receptor Complex. 1. Characterization of Large Plasma Membrane Vesicles from Rat Basophilic Leukemia Cells and Insertion of Amphipathic Fluorescent Probes. *Biochemistry* **1983**, *22* (14), 3466–3474.

(79) Simonsson, L.; Gunnarsson, A.; Wallin, P.; Jönsson, P.; Höök, F. Continuous Lipid Bilayers Derived from Cell Membranes for Spatial Molecular Manipulation. *J. Am. Chem. Soc.* **2011**, *133* (35), 14027–14032.

(80) Hardy, G. J.; Nayak, R.; Alam, S. M.; Shapter, J. G.; Heinrich, F.; Zauscher, S. Biomimetic Supported Lipid Bilayers with High Cholesterol Content Formed by a-Helical Peptide-Induced Vesicle Fusion. *J. Mater. Chem.* **2012**, *22*, 19506–19513.

(81) Jönsson, P.; Beech, J. P.; Tegenfeldt, J. O.; Höök, F. Shear-Driven Motion of Supported Lipid Bilayers in Microfluidic Channels. *J. Am. Chem. Soc.* **2009**, *131* (14), 5294–5297.

(82) Persson, F.; Fritzsche, J.; Mir, K. U.; Modesti, M.; Westerlund, F.; Tegenfeldt, J. O. Lipid-Based Passivation in Nanofluidics. *Nano Lett.* **2012**.

(83) Lingwood, D.; Simons, K. Lipid Rafts as a Membrane-Organizing Principle. *Science* **2010**, *327* (5961), 46–50.

(84) Ryu, Y.-S.; Lee, I.-H.; Suh, J.-H.; Park, S. C.; Oh, S.; Jordan, L. R.; Wittenberg, N. J.; Oh, S.-H.; Jeon, N. L.; Lee, B.; et al. Reconstituting Ring-Rafts in Bud-Mimicking Topography of Model Membranes. *Nat. Commun.* **2014**, *5*, 4507.

(85) Xu, X.; Denic, A.; Jordan, L. R.; Wittenberg, N. J.; Warrington, A. E.; Wootla, B.; Papke, L. M.; Zoecklein, L. J.; Yoo, D.; Shaver, J.; et al. A Natural Human IgM That Binds to Gangliosides Is Therapeutic in Murine Models of Amyotrophic Lateral Sclerosis. *Dis. Model. Mech.* **2015**, *8* (8), 831–842.

(86) Warrington, A. E.; Bieber, A. J.; Van Keulen, V.; Ciric, B.; Pease, L. R.; Rodriguez, M. Neuron-Binding Human Monoclonal Antibodies Support Central Nervous System Neurite Extension. *J. Neuropathol. Exp. Neurol.* **2004**, *63* (5), 461–473.

(87) Xu, X.; Warrington, A. E.; Wright, B. R.; Bieber, A. J.; Van Keulen, V.; Pease, L. R.; Rodriguez, M. A Human IgM Signals Axon Outgrowth: Coupling Lipid Raft to Microtubules. *J. Neurochem.* **2011**, *119* (1), 100–112.

(88) Vyas, A. A.; Schnaar, R. L. Brain Gangliosides: Functional Ligands for Myelin Stability and the Control of Nerve Regeneration. *Biochimie* **2001**, *83* (7), 677–682.

(89) Diaw, L.; Magnac, C.; Pritsch, O.; Buckle, M.; Alzari, P. M.; Dighiero, G. Structural and Affinity Studies of IgM Polyreactive Natural Autoantibodies. *J. Immunol.* **1997**, *158* (2), 968–976.

(90) Zhou, Z. H.; Tzioufas, A. G.; Notkins, A. L. Properties and Function of Polyreactive Antibodies and Polyreactive Antigen-Binding B Cells. *J. Autoimmun.* **2007**, *29* (4), 219–228.

(91) Burastero, S. E.; Casali, P.; Wilder, R. L.; Notkins, A. L. Monoreactive High Affinity and Polyreactive Low Affinity Rheumatoid Factors Are Produced by CD5+ B Cells from Patients with Rheumatoid Arthritis. *J. Exp. Med.* **1988**, *168* (6), 1979–1992.

(92) Ueki, Y.; Goldfarb, I. S.; Harindranath, N.; Gore, M.; Koprowski, H.; Notkins, A. L.; Casali, P. Clonal Analysis of a Human Antibody Response. Quantitation of Precursors of Antibody-Producing Cells and Generation and Characterization of Monoclonal IgM, IgG, and IgA to Rabies Virus. *J. Exp. Med.* **1990**, *171* (1), 19–34.

(93) Maynard, J.; Georgiou, G. Antibody Engineering. *Annu. Rev. Biomed. Eng.* **2000**, *2* (1), 339–376.

(94) Pirko, I.; Ciric, B.; Gamez, J.; Bieber, A. J.; Warrington, A. E.; Johnson, A. J.; Hanson, D. P.; Pease, L. R.; Macura, S. I.; Rodriguez, M. A Human Antibody That Promotes Remyelination Enters the CNS and Decreases Lesion Load as Detected by T2-Weighted Spinal Cord MRI in a Virus-Induced Murine Model of MS. *FASEB J.* **2004**, *18* (13), 1577–1579.

(95) Malmqvist, M. Kinetic Analysis of Engineered Antibody-Antigen Interactions. *J. Mol. Recognit.* **1994**, *7* (1), 1–7.

(96) Crothers, D. M.; Metzger, H. The Influence of Polyvalency on the Binding Properties of Antibodies. *Immunochemistry* **1972**, *9* (3), 341–357.

(97) Swinney, D. C. Applications of Binding Kinetics to Drug Discovery: Translation of Binding Mechanisms to Clinically Differentiated Therapeutic Responses. *Pharmaceut. Med.* **2008**, *22* (1), 23–34.

(98) Swinney, D. C. The Role of Binding Kinetics in Therapeutically Useful Drug Action. *Curr. Opin. Drug Discov. Devel.* **2009**, *12* (1), 31–39.

(99) Swinney, D. Can Binding Kinetics Translate to a Clinically Differentiated Drug? From Theory to Practice. *Lett. Drug Des. Discov.* **2006**, *3* (8), 569–574.

(100) Swinney, D. C. Biochemical Mechanisms of Drug Action: What Does It Take for Success? *Nat. Rev. Drug Discov.* **2004**, *3* (9), 801–808.

(101) Veatch, S. L.; Keller, S. L. Separation of Liquid Phases in Giant Vesicles of Ternary Mixtures of Phospholipids and Cholesterol. *Biophys. J.* **2003**, *85* (5), 3074–3083.

Appendix A Shear Force Driven Lipid Bilayer

This section is included to show a technique we implemented that could be used to incorporate molecules from real membranes onto a chip for kinetic sensing. This novel technique developed by Jönsson and Höök allows lateral repositioning of a supported lipid bilayer (SLB) across a surface.[81]

The method uses a microfluidic chip with a standard cross pattern of channels, with four inlets/outlets. Two solutions are injected simultaneously toward each other, one with vesicles, and one which is only buffer, causing vesicles to rupture on half of the cross pattern. The vesicle solution is switched to buffer only to wash out unruptured vesicles. The inlet/outlet configuration is then switched: the side channel outlets are now closed, and one of the previous inlets is changed to an outlet, directing buffer solution across the chip from the supported lipid bilayer side to the bare side. A high flow rate is applied, and the drag from the liquid drags the top surface of the lipid bilayer so that rolls across the surface. Ingeniously, this method was used to move bilayers to span small wells, depending on the pH of the solution. At lower pH the bilayer will conform to the well, at higher pH the bilayer will span.[81]

This method is illustrated by the fluorescent images in Figure 32. A lipid bilayer has been formed on the left side of the channels, on both the SiO_2 surface as well as the PDMS

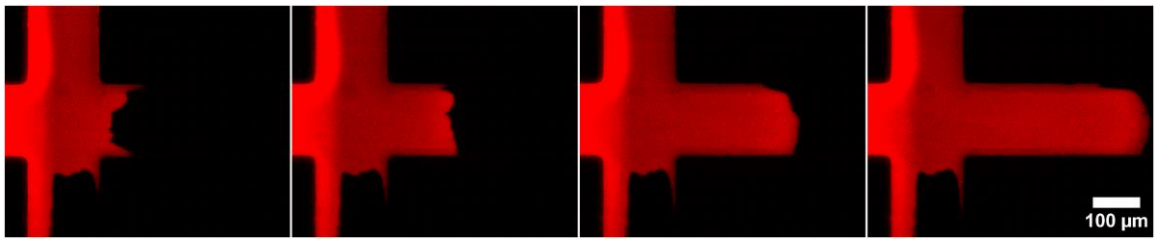

Figure 32: Shear force from a high-speed solution can move a supported lipid bilayer. Time-lapse fluorescence micrographs of a microfluidic chip with channels in a cross pattern, half of which are coated with a supported lipid bilayer. By flowing buffer at a high flow rate over the SLB, the drag from the solution shear force on the SLB pushes it across the surface.

above. As buffer solution is injected over the SLB, the shear force drags the bilayer across the surface.

As discussed in chapter 3, this technique might be able to planarize myelin membranes, bypassing the need of the extrusion process. Myelin particles or GPMVs can be incubated on the SLB-free side, and the SLB can be driven towards them, rupturing or fusing with membranes as they encounter them, thus planarizing larger molecules to bring membrane receptors into the SPR sensing window.[79]